Washington University in St. Louis
Washington University Open Scholarship

McKelvey School of Engineering Theses & Dissertations | McKelvey School of Engineering

Spring 5-15-2023

Nanoparticle Nucleation, Trapping, & Effluent Charging in Low-Temperature Plasmas

Eric Husmann
Washington University in St. Louis

Follow this and additional works at: https://openscholarship.wustl.edu/eng_etds

Recommended Citation
Husmann, Eric, "Nanoparticle Nucleation, Trapping, & Effluent Charging in Low-Temperature Plasmas" (2023). *McKelvey School of Engineering Theses & Dissertations*. 885.
https://openscholarship.wustl.edu/eng_etds/885

This Dissertation is brought to you for free and open access by the McKelvey School of Engineering at Washington University Open Scholarship. It has been accepted for inclusion in McKelvey School of Engineering Theses & Dissertations by an authorized administrator of Washington University Open Scholarship. For more information, please contact digital@wumail.wustl.edu.

WASHINGTON UNIVERSITY IN ST. LOUIS

McKelvey School of Engineering
Department of Energy, Environmental & Chemical Engineering

Dissertation Examination Committee:
Elijah Thimsen, Chair
Richard Axelbaum
Peng Bai
Rajan Chakrabarty
Kathy Flores

Nanoparticle Nucleation, Trapping, & Effluent Charging in Low-Temperature Plasmas

by

Eric Husmann

A dissertation presented to
the McKelvey School of Engineering
of Washington University in
partial fulfillment of the
requirements for the degree
of Doctor of Philosophy

May 2023
St. Louis, Missouri

© 2023, Eric Husmann

Table of Contents

List of Figures iv
List of Tables vi
Acknowledgments vii
Abstract x
Chapter 1: Introduction to Dusty Plasmas 1
1.1 Plasma Fundamentals 1
1.2 Dusty Plasma Fundamentals 3
1.3 Content Overview 5
Chapter 2: Controlling Silicon Nanoparticle Nucleation and Growth 9
2.1 Introduction 9
2.2 Methods 12
2.3 Scaling of NP Nucleation and Growth 20
2.4 Conclusions 39
Chapter 3: Particle Trapping, Size-filtering, and Focusing 41
3.1 Introduction 41
3.2 Experimental Approach and Reactors 45
3.3 Observations of Nanoparticle Trapping 51
3.4 Evidence of Size Filtering 54
3.5 Parametric Monte Carlo Simulation of Particle trapping 56
3.6 Full scale Reactor Simulations of Particle Growth and Trapping 61
3.7 Concluding Remarks 64
Chapter 4: Particle Charge Distributions in the Effluent of a Plasma 66
4.1 Introduction 66
4.2 Methods 69
4.3 Results and Discussion 79
4.4 Conclusions 89
Chapter 5: Concluding Remarks 91
5.1 Summary of Key Findings and Developments 91
5.2 Outlook 92

References 95
Appendix A: Supplementary Material for Chapter 2 .... [111]
A.1 Details on the Reactor Geometry .... [111]
A.2 Transmission Electron Microscopy (TEM) Images .... [112]
A.3 Fitting the QCM Calibration Data .... [113]
A.4 Particle Sampling Line Geometry .... [114]
A.5 Tabulated Parameters and Results .... [115]
A.6 Particle Mass Density as a Function of Silane Concentration .... [118]
A.7 Reaction Mechanism for Global Model .... [120]
Appendix B: Supplementary Material for Chapter 3 .... [127]
B.1 The Monte Carlo Code for Particle Trapping Simulation .... [127]
B.2: Comsol Simulation Results of a Particle Synthesis .... [128]
Appendix C: Supplementary Material for Chapter 4 .... [129]
C.1 Design of the Flow-Through Plasma .... [129]
C.2 DMA Operation and DMA Transfer Function .... [130]
C.3 The Constant Number Monte Carlo Simulation .... [131]
C.4 Collision Kernel Models .... [133]
C.5 Sample Particle Charge Distribution with the Measured Neutral Fraction .... [137]
C.6 Simulation Results at a Conventional Plasma Condition .... [138]

List of Figures

Figure 1.1: Examples and applications of plasmas 2
Figure 1.2: The formation and journey of silicon particles in a nonthermal plasma 6
Figure 2.1: Schematic of the experimental apparatus and diagram of the QCM impactor 13
Figure 2.2: The change in the quartz crystal resonance frequency over time 22
Figure 2.3: Sensitivity of the quartz crystal as a function of radial position 24
Figure 2.4: Particle mass density as a function of the silane fraction fed 26
Figure 2.5: The nucleation onset fraction of silane as a function of reactor pressure 27
Figure 2.6: Mass spectroscopy results 29
Figure 2.7: Mass deposition rate as a function of the reactor inlet silane fraction fed 31
Figure 2.8: Image of the silicon deposit on reactor tubes of various sizes 32
Figure 2.9 The nucleation onset fraction of silane as a function of reactor tube diameter 34
Figure 2.10 Particle mass density and radius predicted by GlobalKin 35
Figure 2.11 Particle properties for varying sticking coefficients 39
Figure 3.1: Overview of two scenarios of particle growth in nonthermal plasmas 40
Figure 3.2: Schematics of two of the two plasma reactors used to investigate particle trapping . 50
Figure 3.3: Experimental results demonstrating particle trapping 52
Figure 3.4: Images of the UMN2 reactor used for silicon quantum dot synthesis 53
Figure 3.5: Particle trapping acting as a size filter 54
Figure 3.6: Parametric Monte Carlo model results of particle trapping 59
Figure 3.7: Reactor simulation and trapped particle locations 63
Figure 4.1: A simplistic diagram of particle charging in a plasma 67
Figure 4.2: Schematic of the experimental setup 70
Figure 4.4: SEM images and bulk work functions 74
Figure 4.5: Sample results from the mobility measurements 81
Figure 4.6: Experimentally determined particle charge fractions 83
Figure 4.7: Experimentally determined mean charges in the plasma effluent 85
Figure 4.8: Simulation results 89
Figure A.1: Illustration of the plasma reactor with the relevant dimensions .... [111]
Figure A.2: Sample TEM images of the synthesized particles .... [112]

Figure A.3: Quartz crystal sensitivity as a function of radial position ....[113]

Figure A.4 Geometry of the sampling line ....[114]

Figure A.5 Mass deposition rate as a function of the silane concentration of the feed gas......[119]

Figure B.1: Schematic of the Monte Carlo code...[127]

Figure B.2: Comsol simulation results of a particle synthesis reactor.....................................[128]

Figure C.1: The flow-through plasma with the Langmuir probe port ....[129]

Figure C.2: The ion-electron collision model ....[136]

Figure C.3: Charge fraction post plasma ....[137]

Figure C.4: Simulation results ....[138]

List of Tables

Table 4.1: Plasma Parameters 72

Table A.1: QCM Impaction Parameters and Results ....[115]

Table A.2: Mass spectroscopy Parameters and Results ....[117]

Table A.3: Gas phase species included in the plasma chemistry model ....[120]

Table A.4: Nanoparticle growth reaction mechanism ....[120]

Acknowledgments

As I reflect over the last five years of my life, there have been so many individuals who have helped me on my journey through graduate school. First, I need to acknowledge and thank my advisor, Dr. Elijah Thimsen. He has consistently challenged me, and I have certainly grown as a person under his tutelage.

I also need to thank all the people who have helped me traverse graduate school. I have learned so much from my current and former lab-mates, Dr. Necip Üner, Dr. Qinyi Chen, Dr. Trey Oldham, Dr. Xiaoshuang Chen, Dr. AJ Cendejas, Dillon Moher, Kirby Simon, and a number of rotating students and undergraduates. I will miss our office chats and outings to get boba tea.

The people who I have collaborated with outside of WashU have also played a major role in my development as a researcher. This would include everyone involved with the New Materials from Dusty Plasmas Multidisciplinary University Research Initiative (MURI), and I would particularly like to thank Dr. Uwe Kortshagen, Dr. Mark Kushner, and Jordyn Polito for what they have taught me.

Next, I would like to thank the Center for Teaching and Learning (CTL) at WashU and Dr. Meg Greggory and Dr. Julia Johnson in particular. The CTL has played a major role in helping me develop my pedagogical skills, and Dr. Greggory and Dr. Johnson played the largest role in that process. I have attended an unknown number of workshops, book clubs, and other programs, and these opportunities have been essential to my goal of becoming a teaching professor.

I wish to thank Dr. Janie Brennan for mentoring me through my first experience as a primary instructor. Her guidance has been the capstone I needed to be prepared for my coming career in teaching following graduation.

I also want to thank my family. They have always been more interested in my happiness rather than how much money I make, and I believe very few people can speak as highly of their families as I can. I am lucky to have them.

Lastly, (but not least importantly), I would like to thank my friends. You all have kept me sane and have pulled me out of isolation more times than I can count.

Eric Husmann

Washington University in St. Louis

May 2023

Dedicated to my mother, who taught me the meaning of unconditional love.

ABSTRACT OF THE DISSERTATION

Nanoparticle Nucleation, Trapping, & Effluent Charging in Low-Temperature Plasmas

by

Eric Husmann

Doctor of Philosophy in Energy, Environmental & Chemical Engineering

Washington University in St. Louis, 2023

Associate Professor Elijah Thimsen, Chair

Nanoparticles in nonthermal plasmas (i.e., dusty plasmas) have been the subject of both great concern and great promise. For microelectronics fabrication, particles from nonthermal plasmas behave as a problematic system impurity; however, due to the interesting properties of the nanoparticles which can be synthesized in nonthermal plasmas, there has been much interest to develop nonthermal plasma-synthesized nanoparticles for a wide range of applications. Given this interest in nonthermal dusty plasma systems, understanding how systematic parameters affect dusty plasma systems is of great importance. As such, this work will focus on three particular phenomena: how systematic parameters affect nanoparticle formation, how forces which act on nanoparticles can cause them to be trapped within nonthermal plasmas, and how particles discharge in the effluent of a nonthermal plasma reactor.

Particles can form in nonthermal plasmas via the condensation of gasses or via chemical transformation. Instead of particles, films also commonly form in nonthermal plasma reactors. Oftentimes, when the goal is to synthesize films, particles are not desired and vice-versa. The first aim of this work is to show how systematic parameters such as reactor size, pressure, and chemical composition control particle vs. film formation.

Once particles form, they are subject to several forces in nonthermal plasmas. The second aim of this work is to show how particles can become trapped by electrostatic forces in nonthermal plasmas, which partially explains the monodisperse nature of nanoparticles synthesized in nonthermal plasmas and informs future approaches for synthesizing nanoparticles.

While nanoparticles are in a plasma, they become highly negatively charged; however, they begin to neutralize as they leave the plasma glow. The third aim of this work is to show how the resulting particle charge may be modulated by varying reactor flow velocity and particle size. This control is necessary for controlling the trajectory of particles by generating electric fields, which is particularly important for particle capture.

Chapter 1: Introduction to Dusty Plasmas

1.1 Plasma Fundamentals

In the context of this dissertation, plasma is the fourth state of matter (the other three being solid, liquid, and gas). Plasmas share many characteristics with gases. Unlike gases, plasmas are ionized, i.e., they contain free electrons and ions. These charged species make plasmas much more conductive than their gaseous counterparts and they are heavily influenced by electric and magnetic fields. Not only are plasmas required for modern life to be possible; they are also a necessity for life on earth in general.

There are many examples of naturally occurring plasmas, and in fact, >99% of matter in the universe exists in the plasma phase [1, 2]. Examples on earth include lightning, natural fires, and auroras. Extraterrestrial examples of plasmas include stars, solar winds, and nebulae. Graphics of natural terrestrial and extraterrestrial plasmas are shown by Fig. 1.1(a-c). While plasmas (most significantly, our sun) are essential for life on earth, artificial plasmas are required for modern technology.

Plasmas are used for wide range of fields including microelectronics manufacturing [3–5], energy production [6–9], vehicle manufacturing [10, 11], lighting and light displays [12, 13], welding [14], experimental instrumentation [15, 16], and more. Some notable examples of plasma use in developing technologies include ion thrusters which are used to aid in satellite navigation [17, 18], tokamak reactors which are used to achieve nuclear fusion for energy production [19, 20], and plasma devices for wound healing [21–23]. Sample graphics are shown

by Fig 1.1(d-f). These applications use different kinds of plasmas, and as such, plasma description and characterization are helpful.

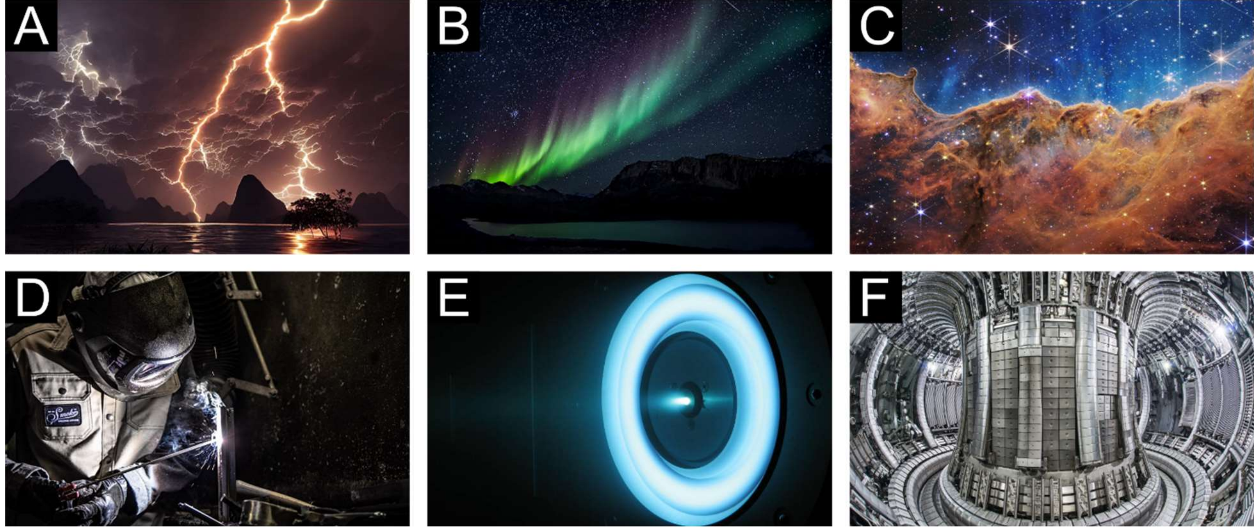

Figure 1.1. Examples and applications of plasmas: (a) the Catatumbo lightning in Venezuela [24], (b) the aurora borealis [25], (c) the "Cosmic Cliffs" in the Carina Nebula [26], (d) an arc welder at work [27], (e) an ion thruster [28], and (f) the inside of the JET tokamak reactor [29].

Plasmas are often separated into two major categories: thermal plasmas and nonthermal plasmas (also called nonequilibrium plasmas). Thermal plasmas form at high temperatures ($T \approx 10^4$ K) and are characterized by being in a state of local thermal equilibrium [30, 31]. More specifically, electrons, ions, and neutral species (including gas molecules and dust particles) have about the same temperature ($T_e \approx T_i \approx T_n$) [30, 31]. Conversely, nonthermal plasmas can form at relatively low temperatures, even down to room temperature, and they are characterized by having a state of thermal nonequilibrium ($T_e > T_i > T_n$) [30, 31]. Note, electron temperatures are commonly described in terms of electron volts (eV), where 1 eV corresponds to about 10^4 K. These plasmas are often produced by generating a strong electric field between two electrodes or

by generating a strong magnetic field via an induction coil. The disparity between species temperatures is the result of how charged species behave in the presence of an electric or magnetic field. While electrons and singly charged ions experience the same magnitude of force given the same electric or magnetic field, electrons are orders of magnitude less massive. As such, they obtain a much higher velocity (and therefore they collectively obtain a higher temperature). In nonthermal plasmas, the electron temperature can be 100 times greater than the bulk gas temperature [30, 31]. As such, the spatial variables required to characterize a plasma are: chemical composition, pressure, bulk gas temperature, electron temperature (more technically, an electron energy distribution as electrons have a distribution of velocities), and ion number density (which is often taken to be equivalent to the electron number density due to plasma quasi neutrality) [30, 31]. This dissertation will focus on the utilization of nonthermal plasmas as they offer specific advantages which will be later highlighted.

1.2 Dusty Plasma Fundamentals

Plasmas which contain particles are called dusty plasmas. Here, particles refer to chemically stable solid or liquid atom clusters which can be as small as ~1 nm. They also may be arbitrarily large, but particles are usually considered to be smaller than 1 mm. Particles play a major role in a variety of plasma processes. In some dusty plasma systems they are the desired product; however, they are major sources of contamination in others. Kortshagen et al. have reviewed a number of promising applications for nonthermal plasma-synthesized nanoparticles [32], some of which include utilizing semiconductor nanocrystal plasmonics for bioimaging [33], implementing doped nanoparticles as a dopant source for semiconductors [34], and including silicon nanoparticles embedded in amorphous silicon to boost photovoltaic performance [35]. On

the other hand, particles are a major concern during semiconductor manufacturing as they can act as “killer defects” in microelectronics [36]. As such, it is important to understand how particles form in plasmas, what forces particles experience once they form, and the lasting effects of plasma-treated particles (such as the resulting particle charge).

Particles, intentionally or unintentionally, can form in plasmas via condensation from a gas phase [37–39] or via gas phase precursor decomposition [32, 40]. Largely due to the nonequilibrium nature of nonthermal plasmas, particle formation via precursor decomposition is much more difficult to model compared to traditional chemical reactor processes. As previously stated, determination of the electron temperature and ion density are required to characterize a nonthermal plasma. Additionally, measuring these parameters is much less trivial compared to measuring pressure and temperature in a traditional chemical reactor [30]. A significant amount of effort has been done to characterize [30] and model [41] plasma reactor systems, and there have also been efforts to apply thermodynamics to explain fundamental behaviors observed in plasma reactors [42, 43].

Once particles are formed in a plasma, they experience a multitude of forces including: Brownian motion, electromagnetic forces, ion drag (caused by momentum transfer between ions and particles), neutral drag (caused by collisions between neutral species and particles), thermophoresis, and gravity [44]. Residence time has often been a varied and/or controlled parameter in plasma reactors used to synthesize particles [45, 46]; however, this parameter fails to capture the residence time that particles often experience in nonthermal plasmas (as it will be later shown). As such, to fully describe and control particle formation, consideration of plasma kinetics must be combined with an understanding of how the forces inside a plasma influence particles once they form.

Several of the forementioned forces are a result of particle charging in plasmas. As particles traverse a plasma, they become highly negatively charged as the electron mobility is much higher than ion mobility in nonthermal plasmas (due to the high electron temperatures) [44, 47–49]. In fact, particles in plasmas frequently have 1-10 negative charges per nm of particle diameter [44, 47–49]. As particles leave a plasma, they will begin to neutralize. If the resulting particle charge could be controlled, then electric fields could be used to control the trajectory of charged particles, which is the operating principle of electrostatic precipitators which are used in industry [50, 51].

1.3 Content Overview

This dissertation will focus on understanding and controlling three specific features illustrated by Fig. 1.2 (a silicon nanoparticle synthesis process is provided as it will be later relevant in Chapters 2 & 3). In a broad sense, these features are particle formation, forces on particles in a nonthermal plasma, and particle charging behavior downstream of a plasma. Chapter 2 will explore how operational conditions can be manipulated to control particle formation in a nonthermal plasma, Chapter 3 will focus on particle trapping behavior once particles have formed, and Chapter 4 will examine the resulting particle charge downstream of a nonthermal plasma.

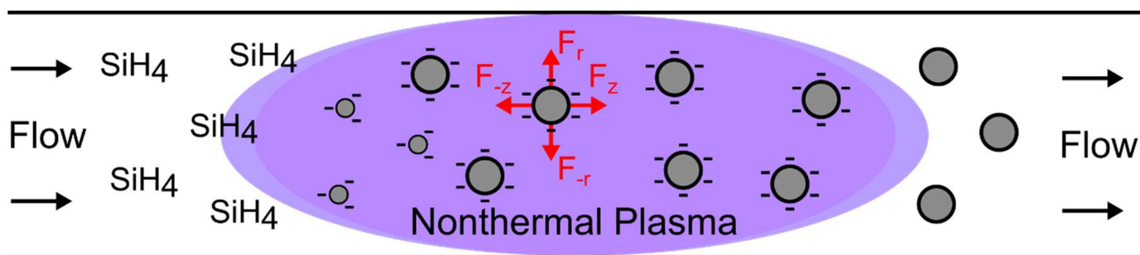

Figure 1.2. The formation and journey of silicon particles in a nonthermal plasma. SiH_4 is shown to decompose into particles. These particles then grow in the plasma and are subject to various forces. The red vectors are used to denote forces in the radial (r) and axial (z) directions. When particles leave the plasma, they lose the majority of their charges.

In Chapter 2, silicon nanoparticle (NP) production from silane is used as a model system to investigate the nucleation process. Although the mechanisms responsible for silicon NP nucleation and growth have been studied [52–54], it is unclear how controllable system parameters (e.g., pressure, system geometry, and gas composition) can be used to inhibit or promote NP formation. For example, the transport of reactive silane species is expected to significantly affect the feed fraction of silane required to nucleate silicon NP (the nucleation onset fraction) due to losses at the reactor walls. In this work, NP mass density was determined as a function of system pressure, gas composition, and reactor diameter for a tubular flow-through radiofrequency (RF) plasma using $Ar/H_2/He/SiH_4$ gas mixtures. A quartz crystal microbalance (QCM) impactor was developed to measure the total aerosol mass density downstream of the plasma and thereby identify the nucleation onset and its dependence on process parameters. A reaction mechanism was developed and incorporated into a global plasma chemistry model to better understand the nucleation onset and NP growth. Jordyn Polito, Dr. Steven Lanham, & Dr. Mark Kushner provided and wrote the material pertaining to the model. This work has been published elsewhere [55].

Chapter 3 presents experimental and computational evidence of, during their growth in the plasma, sub-10 nanometer silicon particles becoming temporarily confined in an electrostatic trap in radio frequency excited plasmas until they grow to a size at which the increasing drag force imparted by the flowing gas entrains the particles, carrying them out of the trap. This trapping is demonstrated to enable the size filtering of the synthesized particles, leading to highly monodisperse particle sizes, as well as the electrostatic focusing of the particles onto the reactor centerline. Understanding of the mechanisms and utilization of such particle trapping will enable the design of plasma processes with improved size control and the ability to grow heterostructured nanoparticles. This work encapsulates a significant collaborative effort which included Zichang Xiong, Dr. Steven Lanham, Dr. Gunnar Nelson, Dr. Mohammad Ali Eslamisaray, Jordyn Polito, Dr. Yaling Liu, Dr. John Goree, Dr. Elijah Thimsen, Dr. Mark Kushner, and Dr. Uwe Kortshagen. Original work by Eric Husmann includes the experimental and writing of the QCM impactor particle trapping results and partial contribution to overall revisions. This work has been published elsewhere [56].

In Chapter 4, monodisperse particles of various sizes and work functions are introduced into an atmospheric pressure radiofrequency capacitively coupled plasma reactor. Dust particle electrical mobility distributions downstream of the plasma reactor are measured utilizing a differential mobility analyzer in conjunction with a condensation particle counter at various reactor flow velocities. Charge distributions are determined from the measured electrical mobility distributions. Experiments confirm that particles become less negatively charged, and even net-positively charged after leaving the plasma volume following a shifted Boltzmann charge distribution. Additionally, particle charge in the effluent of the plasma reactor is shown to be largely independent of work function but highly size and flow velocity dependent. Larger

particles are shown to have a higher magnitude of charge under all studied conditions; however, particle polarity was switchable by varying reactor flow velocity. The charging dynamics beyond the plasma reactor is simulated utilizing a constant number Monte Carlo model which accounts for electron temperature decay and the transition from ambipolar to free diffusion of electrons and ions in the spatial afterglow. Simulation results also suggest that, at same flow velocity, large particles obtain a greater magnitude of charge, negative or positive. The decrease in electron mobility and the difference between ion and electron convective loss rates create an ion-rich region in the plasma effluent that promote ion-particle collisions and drives particle charge removal and even reversal of polarity. Larger particles more favorably collide with energetic species in these environments, which results in higher charge states. Dr. Xiaoshuang Chen provided and wrote the material pertaining to the model. This work has been published elsewhere [57].

Chapter 2: Controlling Silicon Nanoparticle Nucleation and Growth

2.1 Introduction

The promotion or suppression of silicon nanoparticle formation in dilute silane containing plasmas is a topic of interest within the nanomaterials field. Silicon nanoparticles are being investigated for their use in photocatalysis [58, 59], optoelectronics [60], energy storage [61], and medicine [62, 63]. Controlling the nucleation and growth rate of nanoparticles allows for increased particle mass yields, control over particle size, or even suppressed particle formation if particles are undesired. In the case of semiconductor processing, particle deposition onto microelectronics devices during fabrication steps using plasmas continues to be a source of reduced yields [64]. With device dimensions having approached nm scale, particles below 10 nm in diameter are "killer defects" [36]. The suppression of particle formation in these systems typically is accomplished by reducing plasma power, which reduces processing rates and utilization of the feedstock gases. As such, the ability to suppress particle formation while promoting film growth or etching is of great benefit.

Several methods have been reported to reduce particle contamination of thin films during plasma processing. The methods used to prevent existing particles from reaching a film surface include increasing the volumetric flowrate through the plasma reactor to sweep out particles [65] and leveraging thermophoresis to transport particles away from a higher temperature substrate [66]. Plasma pulsing has also been shown to be capable of reducing particle formation and/or removing electrostatically trapped particles [52, 67–69]. Silane containing plasmas for silicon

amorphous film deposition are often diluted with hydrogen to improve film quality [70, 71], a practice that has also been shown to inhibit particle formation [69, 72]. As a side effect, hydrogen dilution can also decrease film deposition rates [73]. In spite of these techniques, particle contamination remains a significant problem and is made more challenging by the need to prevent formation of particles less than 10 nm in diameter to meet current process requirements. Methods of *in-situ* detection of small densities of particles less than 10 nm in diameter are required to ensure that state-of-the-art semiconducting processing reactors operate at acceptably low levels of particle contamination.

A variety of commercially available instruments can be used for the *in-situ* detection and quantification of aerosol nanoparticles including: scanning mobility particle sizers (SMPSs) [74], electrical low pressure impactors (ELPIs) [75], and micro-orifice uniform deposit impactors (MOUDIs) [76]. These devices are well suited for sampling aerosols at atmospheric pressure where the gas density is high. For these conditions, ELPIs can detect particles below 10 nm in diameter. However, most semiconductor processing reactors and low temperature plasma reactors operate at pressures in the range 10^{-3} to 10 mbar. Diagnostic methods suitable for atmospheric or low pressure sampling include optical particle spectrometers (OPCs) [77, 78] and aerosol mass spectrometers (AMSs) [79–81]. OPCs are suitable for detecting particles above 70 nm in size [77], and AMSs can detect particles down to about 10 nm in size [79]. Although each of these devices are powerful, robust and cost-effective techniques to detect low concentrations of aerosol particles below 10 nm in size under low pressure conditions are still needed.

In this paper, we discuss the development and application of a quartz crystal microbalance (QCM) impactor capable of detecting nanoparticles having sizes 10 nm or less under low pressure conditions. Although size information cannot be obtained directly from the

diagnostic reported herein, there are significant benefits of using a single impaction stage including: high mass resolution, high mass sensitivity, low capital cost compared to other instruments, and low operating expenses. For applications such as monitoring dust contamination in microelectronic processing reactors, size information is not always important since the goal is often to suppress nanoparticle formation, or more specifically, have the mass density of the aerosol below a certain value defined by the process quality control constraints. As a demonstration of the capabilities of this QCM impactor, we explored silicon nanoparticle nucleation from silane in a low temperature plasma reactor, and processes that contribute to the nucleation of such particles.

In spite of several studies related to the nucleation and formation of silicon nanoparticles in dilute silane plasmas, little focus has been given to suppressing or promoting particle formation by exploiting the transport of reactive silane radical species. Maemura et al. studied particle densities in a parallel plate plasma reactor at two different electrode spacings; however, the effects of electrode spacing on particle mass density were unclear [82]. Bhandakar et al. demonstrated that particle formation can be suppressed by increasing the Brownian diffusion of reactive species by increasing the bulk gas temperature [83].

In this work, a QCM impactor was developed to study the effects of tube diameter, reactor pressure, and gas composition on particle formation (presented as a mass density of particles leaving the plasma reactor). Decreasing the discharge tube diameter inhibited particle formation as reactive species diffuse shorter distances on average to be lost to the reactor walls. Since diffusion coefficients scale inversely with pressure, to test the hypothesis we showed that increasing pressure can also promote particle formation by suppressing diffusive losses. As hydrogen addition to the gas mixture is known to inhibit particle growth, hydrogen content in the

reactor inlet was also varied to determine if the consequences of hydrogen content and tube diameter/operating pressure are cumulative. A 0-dimensional global plasma chemistry model was adapted to predict NP growth, and to provide further insights into silicon nanoparticle growth as a function of inlet gas composition and reactor diameter.

2.2 Methods

To quantify the effects of pressure, reactor tube diameter, hydrogen content, and the silane fraction fed on NP nucleation, experiments were performed for two sets of conditions: constant pressure, and constant reactor tube diameter. For each of these cases, hydrogen content and the silane fraction were varied, however, the total molar flowrate was constant for all experiments. Particles generated in the plasma reactor were detected by the QCM impactor. Comparison of trends for NP production were made with results from the global plasma chemistry model.

2.2.1 Experimental Methods

The primary components of the experimental setup are the tubular plasma reactor and the QCM impactor, illustrated in Fig. 2.1. The plasma reactor consists of a 25 cm-long fused silica tube with two ring electrodes to produce a capacitively coupled plasma (CCP). Tubes having inner diameters of 1.0 cm, 1.7 cm, 2.2 cm, and 3.2 cm were investigated. Further details on the reactor geometry can be found in section A.1 in Appendix A. The feed gas was 0.9% silane in helium and a balance gas of either pure argon, 10% hydrogen in argon, or pure hydrogen. The total molar flowrate, controlled by flow controllers (MKS Instruments and Bronkhorst), of the feed gas was held constant at 52 standard cubic centimeters per minute (sccm). The reactor

pressure was varied from 4.5 to 8.5 Torr by throttling the pump via a valve. A radio frequency (RF) 13.56 MHz AG0163 power supply with an AIT600 matching network (T&C Power Conversion) was used to supply the plasma reactor with 5 W of power, which was constant for all conditions. Ideally, average plasma parameters (e.g., electron temperature, ion density, bulk gas temperature) would be kept constant for all conditions; however, the measurement and maintenance of these parameters was beyond the scope of this work. Note that the measurement of plasma parameters for a silane plasma using Langmuir probe techniques [84] is made challenging due to silicon deposition fouling on the probe tips [85].

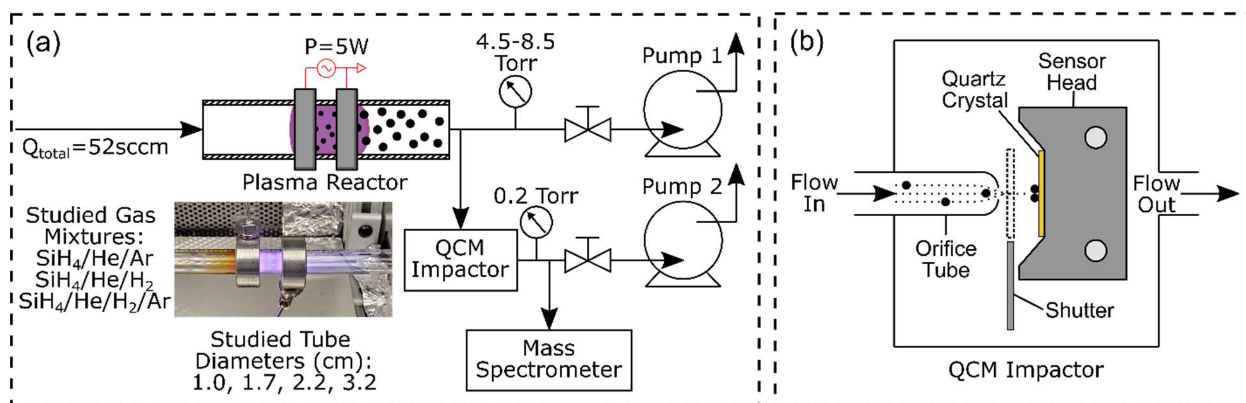

Figure 2.1. (a) Schematic of the experimental apparatus (b) diagram of the QCM impactor.

Downstream of the plasma reactor, gas was diverted to the QCM impactor. The amount of gas diverted was not held constant due to the different reactor pressures and chemical composition. A 150 μm diameter orifice tube (Lenox Laser) was used to impact particles onto the quartz crystal (Telemark, part number 880-0201-3). Molar flowrates to the QCM were determined using software provided by the orifice manufacturer [86]. The pressure downstream

of the orifice was held at 0.2 Torr.

For the conditions of this investigation, all particles, irrespective of size, are expected to impact onto the quartz crystal since the critical cutoff diameter of impaction, $d_{p,c}$, was always less than 1 Å (much smaller than any critical cluster size). As a result, the QCM measures the total aerosol mass current in the sample stream. The cutoff diameter of impaction is given by [78]:

$$d_{p,c} = \left(\frac{9\pi \cdot \mu \cdot D_O^3 \cdot Stk_C}{4 \cdot \rho_p \cdot Q \cdot C_C(P)} \right)^{0.5} \tag{2.1}$$

where μ is the dynamic viscosity of the gas, D_O is the diameter of the orifice, Stk_C is the critical Stokes number (0.24 for a circular orifice), ρ_p is the mass density of the particle material (i.e. silicon), Q is the volumetric flowrate through the orifice, and $C_C(P)$ is the Cunningham slip correction factor, which is dependent on pressure. Particles were assumed to stick to the QCM surface since the particles were small (< 10 nm) and thus the particles had a smaller kinetic energy in comparison to the adhesion energy [87, 88]. Particle size was verified using a transmission electron microscope (TEM), and results can be found in section A.2 in Appendix A. To maintain constant impaction conditions, the orifice was cleaned between experiments using sonification in water for 5 minutes followed by blasting with pressurized air. The orifice was subsequently dried in a desiccator oven.

The quartz crystal was held by a sensor head (Telemark) equipped with a shutter. The resonance frequency of the quartz crystal was monitored using an OSC-100 oscillator (Inficon) and an FTM-2400 quartz crystal monitor (Kurt J. Lesker). The change in resonance frequency of the quartz crystal can be converted into a mass loading by using the Sauerbrey equation [89]:

$$\Delta m = -\Delta f \cdot \left(\frac{A \cdot (\rho_q \cdot \mu_q)^{0.5}}{2 \cdot f_0^2} \right) \tag{2.2}$$

where Δm is the change in the mass loading of the quartz crystal, Δf is the change in the quartz crystal resonance frequency, A is the effective crystal area, ρ_q is the density of the quartz crystal (2.65 $g \cdot cm^{-3}$), μ_q is the shear modulus of the quartz crystal ($2.95 \cdot 10^{11}$ $g \cdot cm^{-1} \cdot s^{-2}$), and f_0 is the resonant frequency of the fundamental mode of the quartz crystal (6 MHz). To avoid overloading, the quartz crystal was replaced whenever $\Delta f > 40$ Hz from its original value. The sampling procedure for the QCM is as follows: plasma ignition, opening the QCM shutter after 10 seconds, particle sampling for up to 120 seconds, closing the QCM shutter, turning the plasma off. Deposition rates were determined by fitting the linear response of the QCM. Deposition rates were then converted into particle mass densities by normalizing the deposition rates by the volumetric flowrate to the QCM.

Particles were impacted onto a small area at the center of the crystal. As a result, the calculated mass loading is expected to be overestimated by a constant factor if the effective crystal area is assumed to be that of the overlapping electrodes on the quartz crystal (0.33 cm^2, as determined from the electrode geometry shown in Fig. A.3 of Appendix A). This overestimate is due to the quartz crystal having a radially dependent mass sensitivity, with a maximum sensitivity at the center [89–91]. To account for this effect, the sensitivity of the QCM was determined as a function of radial distance from the center of the quartz crystal, r. To perform this calibration, a 200 $ng \cdot \mu L^{-1}$ solution of < 25 nm TiO_2 nanoparticles (Sigma-Aldrich, catalog number 637254) in deionized water (18.2 $M\Omega \cdot cm$) was prepared. QCM sensitivity as a function of r was determined by depositing 0.2 µL of the prepared solution at various locations for a series of quartz crystals. The water was left to evaporate at atmospheric conditions for 6 minutes,

leaving behind a deposit of TiO_2 nanoparticles of a known mass. QCM sensitivity was then calculated as the change in the quartz crystal resonance frequency over the mass loading. The positions of the deposits were measured from digital images of the quartz crystals. To avoid depositing over existing deposit and to simplify image processing, up to 4 depositions were performed in a line for each quartz crystal.

Downstream of the QCM, a quadrapole mass spectrometer (ExTorr Inc., Model XT300) was used to determine the amount of remaining silane. Ionization of the silane was performed by electron impact using an electron energy of 70 eV and a current of 2 mA. The m / z = 31 peak (corresponding to the mass-to-charge ratio of SiH_3^+, a dominant product of dissociative ionization of SiH_4) was normalized by the m / z = 4 peak (corresponding to helium) to account for small fluctuations of the reactor pressure upon plasma ignition and termination, which directly affected the flow to the mass spectrometer.

2.2.2 Computational Methods

GlobalKin, a 0-dimensional plasma chemistry model, was adapted for use in this work to predict NP growth. A detailed description of *GlobalKin* can be found in Refs. [92] and [93]. *GlobalKin* provides a volume averaged description of a plasma reactor by accounting for electron impact reactions, heavy particle reactions, surface reactions, and gas flow. Species densities are solved by integrating their continuity equations while accounting for sources and losses due to gas flow, diffusion to surfaces, and reactions with electrons, ions, and neutrals. An average electron temperature is given by the electron energy equation. The master equation for the density of species i is

$$\frac{dn_i}{dt} = \sum_j \left\{ \left(a_{ij}^P - a_{ij}^R\right) k_j \prod_l n_l^{a_{ij}^R} \right\} + \sum_m \left\{ -\frac{D_i n_i}{\Lambda^2} f_m S_{im} + \sum_k \frac{D_k n_k}{\Lambda^2} f_m S_{km} g_{ikm} \right\} \quad (2.3)$$

where the first sum is over reactions j having rate coefficient k_j and l reactants. The stoichiometric coefficient for reactant species i in reaction j is a_{ij}^R and for products is a_{ij}^P. The second summation accounts for reactions on m different surfaces each having a fraction f_m of the total surface area. The first term in brackets is for loss of species i having diffusion coefficient D_i, diffusion length Λ and sticking coefficient S_{im} on surface m. The second term is for gain in species i due to reactions on the surface of species k with branching ratio to produce species i of g_{ikm}.

The conditions for the model are those of the experiment – a 52 sccm Ar/He/SiH_4 mixture flowing into a quartz tube reactor (diameter = 1.0 cm – 3.2 cm). Gas flow through the reactor is approximated using a plug-flow approach such that a slug of gas travels down the length of the reactor (15 cm) with an initial speed dependent upon inlet flowrate, gas density, and cross-sectional area of the reactor. The flow speed is adjusted as electron impact, heavy particle reactions, and gas heating change gas density to maintain a constant pressure. The power density profile is specified to approximate that of the experiment with a volume integral of the power density being held constant at 5 W.

A particle growth algorithm was incorporated into *GlobalKin* to investigate trends in Si NP growth and suppression as functions of plasma operating conditions. A list of species and reactions used in the model for NP growth are in S.8 of the SI. Briefly, silane molecules undergo electron impact dissociation to form Si_xH_y radical species. A radical species is any Si_nH_m species where $m < 2n+2$. Any species having $m = 2n+2$ is a saturated silane species. Dissociation of

silane molecules is produced by electron impact dissociative excitation and ionization, dissociative recombination, charge exchange, and excitation transfer from rare gas atoms. Si_nH_m radicals combine with each other or with saturated molecules to form higher order Si_nH_m species. This process continues until Si_nH_m clusters become large enough to be classified as nanoparticles. Here we classified a nanoparticle to be any Si_nH_m species with $n \geq 13$. For example, the reaction

$$Si_3H_7 + Si_{11}H_{24} \rightarrow NP \tag{2.4}$$

produces a NP as the sum of the silicon atoms in the reactants exceeds 12.

Nucleation reactions, as in Eq. 2.4, initially produce and increase both the mass density and number density of NPs. Surface growth reactions, such as

$$SiH_3 + NP \rightarrow NP \tag{2.5}$$

add to the mass density of NPs while not adding to the number density of NPs. Coagulation reactions such as

$$NP + NP \rightarrow NP \tag{2.6}$$

decrease the number density of NPs while not changing the mass density, thus yielding particles with larger effective radii. Neutral NPs were classified as being saturated or radicals, depending on the growth species.

The choice to represent a NP as any Si_nH_m species having greater than 13 Si atoms was based in part on computational efficiency and part on the concept of “critical cluster size.” As higher order Si_nH_m species are included in the mechanism, the number of reactions needed – and

therefore the computational time required – to account for nucleation and coagulation grows rapidly. Here we take "critical cluster size" to mean the point at which a particle has reached a sufficiently large radius that growth is dominated by surface processes (silane radicals sticking on the growing NP) and later by coagulation reactions (NP reacting with NP). Once the silane radicals have been depleted, growth is dominated by coagulation. The cross sections for both radical growth and coagulation increase as the number of Si atoms in the particle increases [94]. Optimization of the reaction mechanism used here has shown that the choice of 13 Si atoms to a NP enables representation of nucleation, growth and coagulation processes with relative computational efficiency on the timescales relevant in this system. This cluster size is consistent with experimental measurements of the smallest observable Si cluster by differential mobility analysis [95]. Nucleation, growth, and coagulation reactions occur simultaneously, though we expect the rate of coagulation to dominate as particles increase in size and silane radicals are depleted.

When nanoparticle number density in the plasma is high, they can carry both negative and positive charge [96, 97]. Negative and positive nanoparticles are accounted for as separate species with independent mass densities. Negative and positive nanoparticles can interact with neutral nanoparticles through charge exchange or coagulation, or with each other through neutralization reactions. We assume that the elementary charge on the particles does not exceed ± 1. Previous work has shown that this assumption is valid when the nanoparticle diameter is small [98].

Particle growth is tracked by accounting for changes in particle mass density,

$$\frac{d\rho_m}{dt} = \sum_{i,j} n_i n_j k_{ij} \left(\pm \Delta m_{ij} \right) \tag{2.7}$$

where ρ_m is the instantaneous mass density of particle species m, k_{ij} is the reaction rate coefficient between species i and j having densities n_i and n_j. Δm_{ij} is the change in mass of the NP due to these reactions. Losses in particle mass density due to diffusion to the reactor walls are also accounted for (Eq. 2.3).

The instantaneous NP mass is derived from the mass density as

$$m_i = \frac{\rho_i}{n_i} \tag{2.8}$$

where n_i is the number density of NP particle species i. Assuming particles are spherical, the radius of the particle scales as

$$r_i = r_0 \left(\frac{m_i}{m_0} \right)^{1/3} \tag{2.9}$$

where r_0 is the original radius of the particle species and m_0 is the original mass of the particle species.

2.3 Scaling of NP Nucleation and Growth

Experiments were performed to validate the QCM impactor and to determine the effects of system parameters on particle formation. Qualifying the QCM impactor included verifying that the QCM could detect the onset of particle formation and calibrating the QCM to accurately relate the QCM response to mass loading. Following verification of the QCM impactor, the

effects of pressure, hydrogen content, reactor tube diameter, and the silane fraction at the reactor inlet on particle formation were investigated using both experimental and computational methods.

2.3.1 Verification of the QCM Impactor

Preliminary validation of the QCM impactor, and establishing a nucleation threshold silane inlet fraction, were performed by tracking Δf over time while varying the fraction of silane fed into the plasma reactor around the nucleation threshold, as shown in Fig. 2.2. The expectation is that below the particle nucleation threshold, no mass deposition will be observed, as indicated by negligible change in the sensor resonance frequency. Above the threshold, a disproportionately large linear slope will be observed when compared to the silane inlet fraction below threshold. Very little to no particle deposition was observed up to a reactor inlet silane fraction of 140 ppm. However, particle deposition was observed at a silane inlet fraction of 174 ppm, indicated by the linear shift of the quartz crystal resonance frequency that is larger in magnitude than the digital noise floor. This result establishes a baseline that a minimum silane concentration at the reactor inlet is required for particles to nucleate and be detected [53, 99].

Since the resolution of the QCM is 0.1 Hz and instrumental drift is low (< 0.1 Hz·min^{-1}), particles were said to be observed if $\Delta f / \Delta t > 0.3$ Hz·min^{-1}. The reactor inlet silane fraction required to satisfy this criterion is defined as the nucleation onset fraction. Although this definition ignores potential particle losses upstream of the QCM, and variation in particle transmission efficiency due to distributions in particle size, it does account for the abrupt jump of $\Delta f / \Delta t$ observed over a relatively small change in silane feed fraction. A geometric description of the gas line from the plasma reactor to the QCM impactor orifice is provided in section A.4 of

the Appendix.

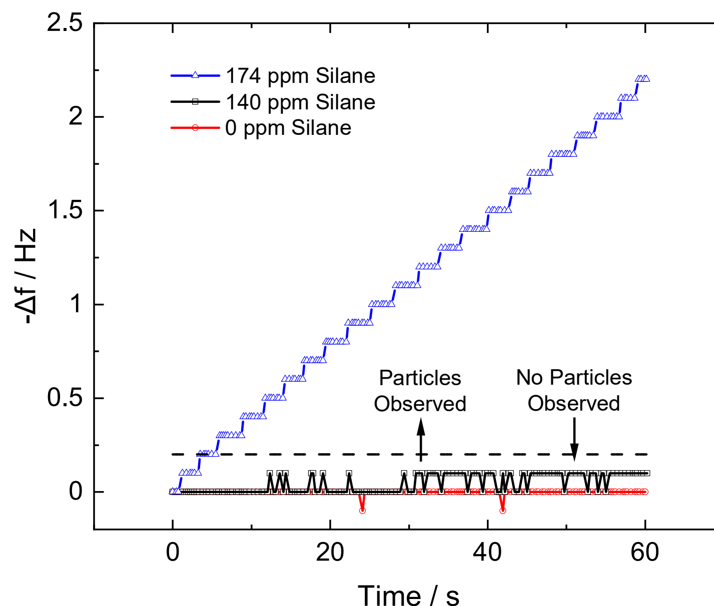

Figure 2.2. The change in the quartz crystal resonance frequency over time for various molar fractions of silane fed into the plasma reactor. The following parameters were used: reactor pressure: 6.5 Torr, tube diameter: 1.7 cm, and balance gas: pure Ar.

To accurately relate the change in frequency of the QCM to a mass loading, quartz crystal sensitivity (defined as $S = -\Delta f / \Delta m$) as a function of r was determined as shown by Fig. 2.3. Bessel functions and modified Bessel functions have been shown to accurately model the radially-dependent vibrational response of planar quartz crystals [90]. However, Eq. 2.10, an empirical relationship reported in the literature [100, 101], provided a more accurate description of the data. Note that similar expressions are used for plano-convex crystals [90]. A comparison of the two models can be found in section A.3 in Appendix A.

$$S = S_{\max} \cdot \exp(-\beta \cdot r^2) \qquad (2.10)$$

S_{max} represents the maximum sensitivity of the quartz crystal (where $r = 0$), and β is an empirical constant which describes the width of the sensitivity distribution. Values for S_{max} and β were determined to be 3.40 Hz·ng^{-1} and 73 cm^{-2} respectively. The area-averaged sensitivity of the quartz crystals was determined to be 0.28 Hz·ng^{-1} using Eq. 2.11,

$$S_{avg} = \frac{2}{r_0^2} \int_0^{r_0} S(r) \cdot r \cdot dr \qquad (2.11)$$

where r_0 is the radius of the exposed quartz crystal (0.405 cm). From taking the ratio of S_{max} to S_{avg}, sensitivity of the quartz crystal is increased by a factor of 12 when depositing on the center of the quartz crystals rather than over the entire area. These sensitivities can also be converted into a minimum mass deposition rate required for detection by the QCM impactor of 88 pg·min^{-1} for the center of the quartz crystal and approximately 1056 pg·min^{-1} when depositing over the entire exposed area.

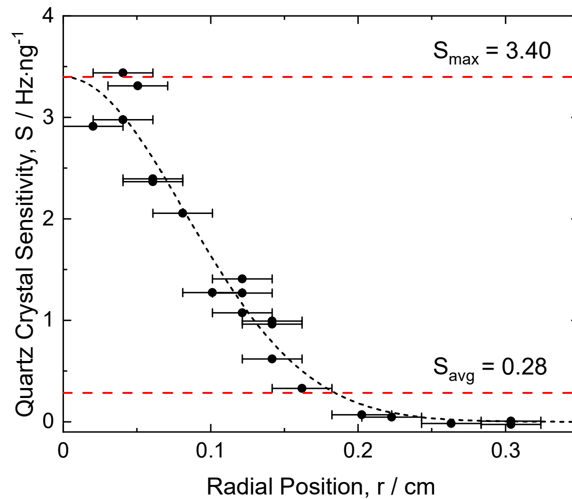

Figure 2.3. Sensitivity of the quartz crystal, *S*, as a function of radial position, *r*. The dotted line represents the fit given by Eq. 2.10, and the error bars represent the area over which the deposit was spread. The maximum and area averaged sensitivities are provided.

2.3.2 The Effects of System Parameters on Particle Formation – Experimental

To relate the nucleation onset fraction to experimental parameters, particle mass density (the mass deposition rate normalized by the volumetric flowrate to the QCM) was determined as a function of the silane fraction in the reactor inlet, reactor pressure, and hydrogen content, as shown in Fig. 2.4. For all cases, the mass density increased with increasing silane fraction at the reactor inlet. Intuitively, as more silane was fed into the reactor, more mass can be incorporated into particles. As pressure was increased at the same fraction of silane at the reactor inlet, particle mass density increased for all cases. The increase in mass density of the NPs agrees with the hypothesis that decreasing the diffusion coefficient of reactive silane radical species (by increasing the pressure) promotes particle formation over film deposition on the walls of the reactor. As the diffusion coefficient of reactive species is decreased and the reactor size is held constant, more radical species can be incorporated into particles before depositing on the walls since transport to the reactor walls is limited. Note that by the ideal gas law, increasing pressure will increase the silane mass density at the reactor inlet even if the fraction is the same. However, the pressure effects are still significant if Fig. 2.4 is replotted as a function of silane mass density at the reactor inlet rather than silane fraction (see section A.6 of Appendix A).

When a 10% H_2 gas mixture was used in the inlet, shown by Fig. 2.4b, particle mass density generally increased compared to the pure argon case, shown by Fig. 2.4a. This result was surprising as hydrogen has been reported to suppress particle formation [69, 72]. A moderate amount of H_2 in the balance gas appears to be disproportionately inhibiting film formation on the walls over particle growth for these conditions. Hydrogen radicals can deprotonate silane and other silyl species via hydrogen abstraction [54, 102], and the resultant faster reaction kinetics

are expected to promote particle formation over film growth due to diffusion to the walls.

This mechanism would require the increased rate of silane deprotonation by hydrogen radicals to be greater than the increase in conversion of reactive silyl species back into silane by hydrogen incorporation. Alternatively, a small to moderate amount of H_2 in the inlet flow may disproportionally inhibit film formation over particle formation by reducing the number of potential reactive sites on the reactor walls. Upon increasing the hydrogen fraction from 10% H_2 to pure H_2, particle mass density in the effluent was decreased by over an order of magnitude (Figs. 2.4b-c). Particle formation is suppressed for high fractions of hydrogen in the balance gas. This effect will be later discussed in more detail.

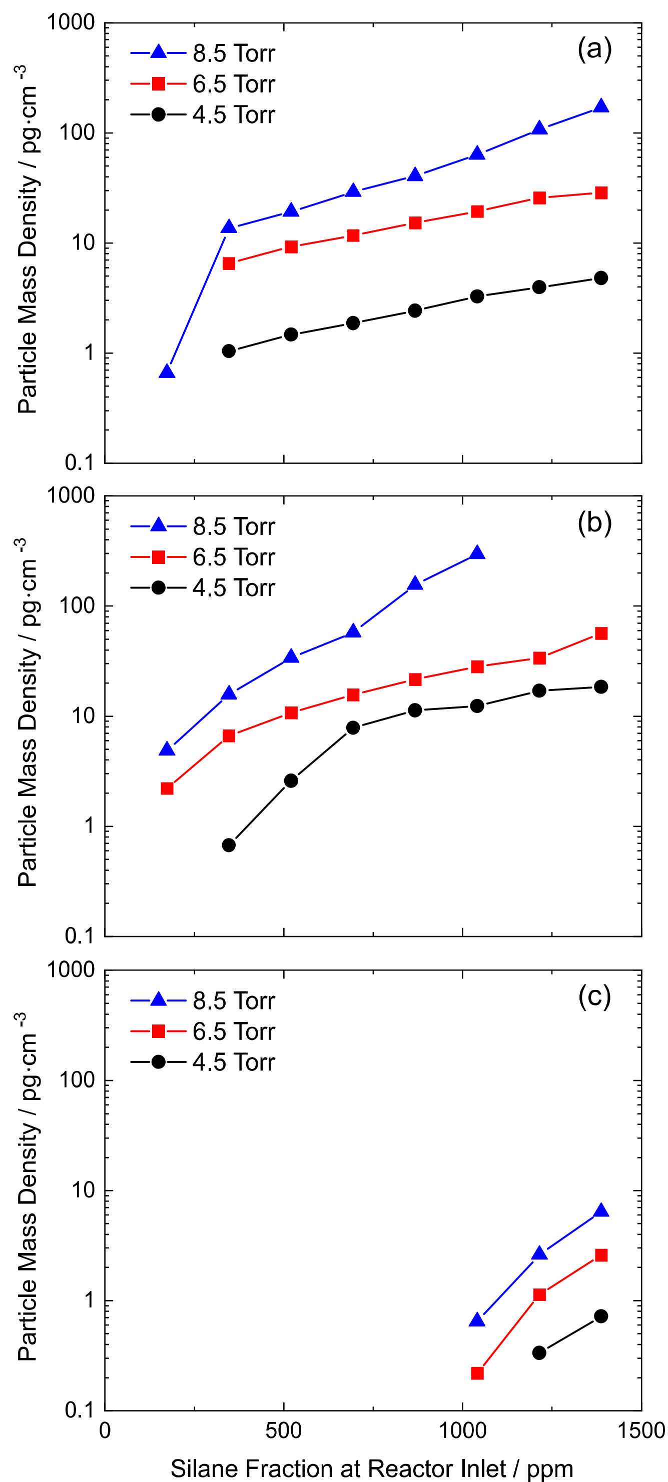

Figure 2.4. Particle mass density as a function of the silane fraction fed into the plasma reactor for various pressures given a balance gas of (a) pure Ar, (b) 10% H_2 in Ar, (c) pure H_2. Tube diameter was held constant at 1.7 cm. Tabulated parameters and results are provided in section A.5 in Appendix A.

Since the suppression of particle formation is important for a variety of industrial processes, the nucleation onset fraction was measured as a function of pressure and hydrogen content in the balance gas. The results are shown by Fig. 2.5. The nucleation onset fraction provides a minimum reactor inlet silane fraction above which particles can be detected with the QCM impactor. As the reactor pressure was increased, the nucleation onset fraction generally decreased. The effect of pressure was most significant when the balance gas was 10% H_2 where the nucleation onset fraction was reduced by a factor of 3 over a pressure range of 4.5 Torr to 8.5 Torr. However, this reduction was small considering that the increase in pressure results in an increase of the density of silane at the rector inlet by approximately a factor of 2. When a balance gas of pure H_2 was used, the nucleation onset fraction was larger and nearly constant over the pressure range that was investigated.

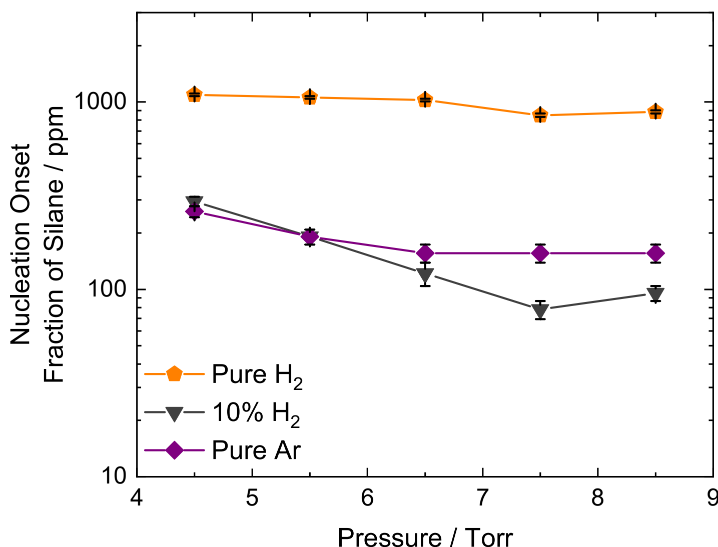

Figure 2.5. The nucleation onset fraction of silane as a function of reactor pressure for various balance gases. The reactor tube diameter was 1.7 cm. The bottom and top of the error bars represent the reactor inlet silane fractions at which the measured deposition rate was below and above the nucleation threshold respectively.

When the balance gas was switched to pure H_2, particle formation was greatly suppressed, as shown by Fig. 2.4c and Fig. 2.5. This result corroborates previous reports in the literature [69, 72], and can be explained by the suppression of silane conversion into reactive species. Mass spectroscopy was performed for verification, as shown in Fig. 2.6. For the pure Ar case, total silane conversion (into either particles or film on the walls) was over 95%. For the pure H_2 case, the total silane conversion was only 34%. As such, large fractions of hydrogen seem to aid in suppressing particle formation. However, there is a cost of also significantly reducing silane utilization.

Silane conversion was independent of tube diameter for 1.0 cm and 3.2 cm tubes at 6.5 Torr and otherwise the same flow conditions, as determined by mass spectroscopy of the plasma effluent (Fig. 2.6). The timescale of silane conversion is expected to be much shorter than the gas residence time in the plasma reactor [103], and the observed film deposition onto the reactor walls was largely focused upstream or at the powered electrode with little film deposition at or past the grounded electrode. As such, gas residence time is not expected to be an important parameter in determining eluted particle mass density, independent of reactor pressure and diameter, for our conditions. It would be ideal to have the capability to channel the silicon mass into either particle formation or film deposition, depending on the goal of the process, while maintaining a high precursor conversion. Varying reactor tube diameter appears promising to that end.

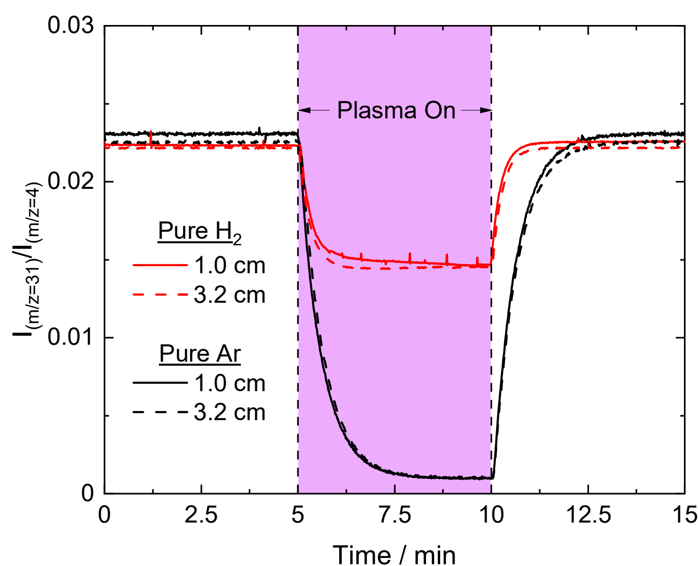

Figure 2.6. Mass spectroscopy results showing the *m* / *z* = 31 intensity (silane) over the *m* / *z* = 4 intensity (helium) as a function of time given a balance gas of pure Ar or H_2. The silane feed fraction was 1388 ppm, the reactor pressure was 6.5 Torr. Two tube diameters were tested: 1.0 cm and 3.2 cm. Tabulated parameters and results are provided in section A.5 in Appendix A.

Particle mass density increased with tube diameter. To assess how the reactor tube diameter affects particle formation, particle mass density was measured as a function of the reactor inlet silane fraction at a constant reactor pressure of 6.5 Torr for various tube diameters, as shown by Fig. 2.7. Similar to the results shown in Fig. 2.4, particle mass density increased with increasing silane fraction at the reactor inlet for any given tube diameter. Upon increasing the tube diameter, particle mass density increased significantly for the pure Ar and 10% H_2 cases (over an order of magnitude when comparing the 1.0 cm tube mass densities to the 3.2 cm tube mass densities). These experiments were carried out at constant pressure and flow rate, and thus were free of artifacts due to changing silane mass density at the reactor inlet. This result is consistent with the original hypothesis that smaller tubes will suppress particle formation due to

higher rates of diffusion loss to the walls. To further support the hypothesis, film deposition on the reactor walls increased for smaller tube sizes (noted by a much darker coloration on the reactor tube) as shown by Fig. 2.8. Each tube was subject to the same experimental conditions and methods (apart from the variable tube diameter). It is noted that deposition was eventually observed for tubes of all sizes upon extended use, although the deposition was more rapid on smaller tubes (data not shown here).

Particle mass densities were similar for the cases when the balance gas was Ar compared to 10% H_2 (all else kept constant). However, when the balance gas was switched to pure H_2, a significant decrease in particle mass densities occurred. For the pure H_2 case, particle mass density no longer increased with increasing tube diameter. High H_2 content may be lowering reaction rates such that deposition on the reactor walls is limited by kinetics rather than diffusion. This would explain why particle formation was suppressed (due to the lower concentrations of reactive species) and why the tube diameter becomes less relevant. As previously discussed, high H_2 content can suppress both particle and film formation on the walls of the tube. As such, the potential benefit of inhibiting particle formation is accompanied by reducing the film deposition rate.

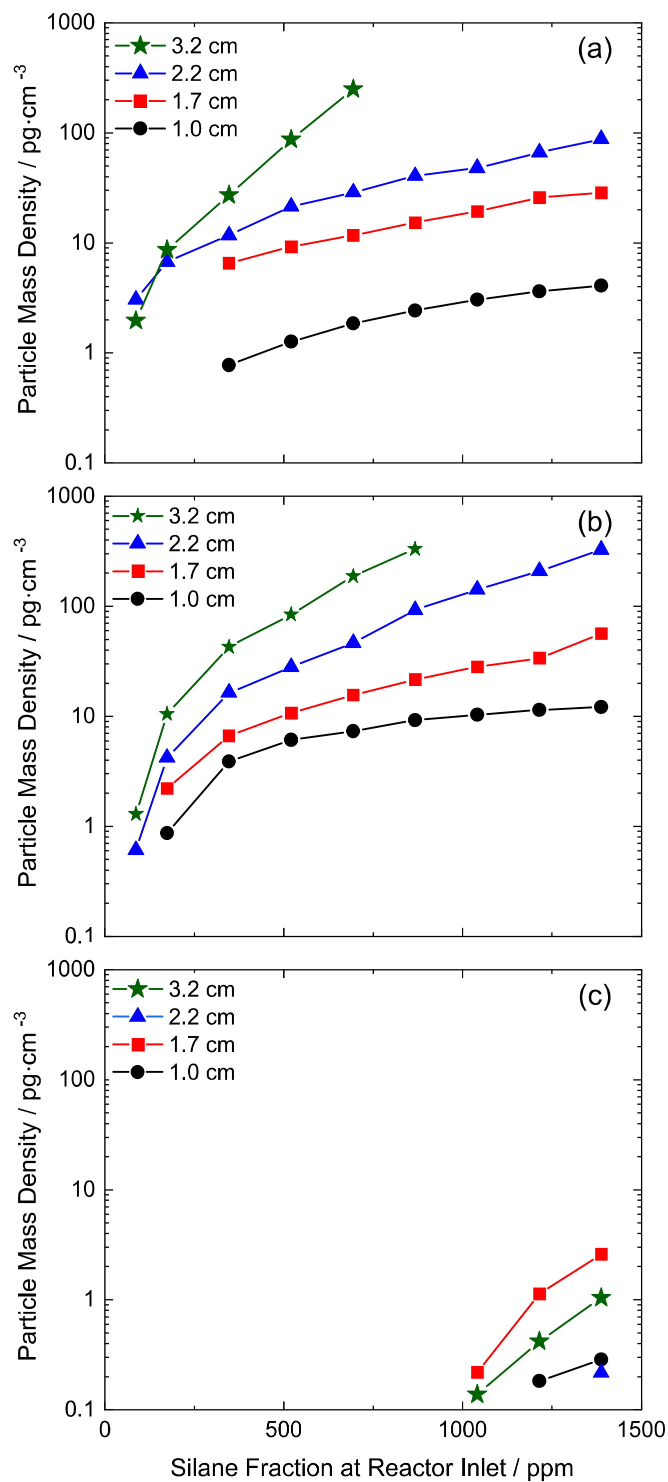

Figure 2.7. Mass deposition rate as a function of the reactor inlet silane fraction fed into the plasma reactor for various tube diameters given a balance gas of (a) pure Ar, (b) 10% H_2 in Ar, (c) pure H_2. Reactor pressure was held constant at 6.5 Torr. Tabulated parameters and results are provided in section A.5 in Appendix A.

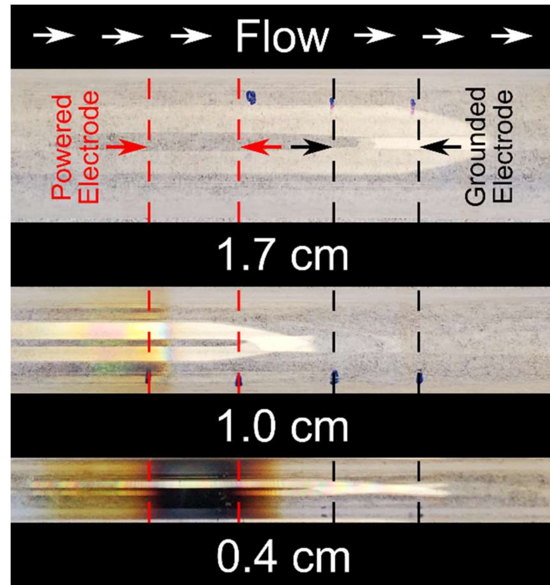

Figure 2.8. Image of the silicon deposit on reactor tubes of various sizes. A 0.4 cm tube is included here to exaggerate tube diameter effects. Each tube was subjected to the same experimental conditions, apart from the changing tube diameter.

The results shown in Fig. 2.7 indicate that increasing reactor tube diameter can increase particle mass density when the background gas is Ar, while with a balance gas of pure H_2, the particle mass density is nominally independent of tube diameter. It is not immediately clear how the nucleation onset fraction of silane will be affected. As such, it is useful to express the nucleation onset fraction of silane as a function of reactor parameters for applications which focus on inhibiting particle formation. The nucleation onset fractions as a function of tube diameter given a balance gas of pure Ar, 10% H_2, and pure H_2 are shown in Fig. 2.9. For the pure argon case, increasing the tube diameter from 1.0 cm to 3.2 cm decreases the nucleation onset fraction by over an order of magnitude, a result explained by diffusion losses to the wall.

Upon switching to a balance gas of 10% H_2, increasing the tube diameter from 1.0 cm to 3.2 cm only decreased the nucleation onset fraction by a factor of 2, as hydrogen can suppress the effects of varying tube diameter by limiting reaction kinetics. This result may suggest that the

deprotonation of silane radical species by hydrogen radicals was not significant compared to the insertion of hydrogen to convert reactive silane species back into silane species. As such, hydrogen may generally inhibit silane conversion, but disproportionally favor particle formation or film formation depending on the specific reactor conditions.

The nucleation onset fraction was significantly increased when the balance gas was switched to pure H_2, meaning particle nucleation was suppressed. The nucleation onset fraction appears to be largely independent of the tube diameter for a pure H_2 balance gas. Although varying H_2 content and varying the tube diameter appear to be useful parameters for suppressing or promoting particle formation, these effects cannot be combined to suppress particle formation. Although hydrogen may be required for some deposition processes to control film crystallinity [70, 71], for processes that do not require hydrogen, the use of small reactor sizes for deposition processes shows promise for inhibiting particle formation.

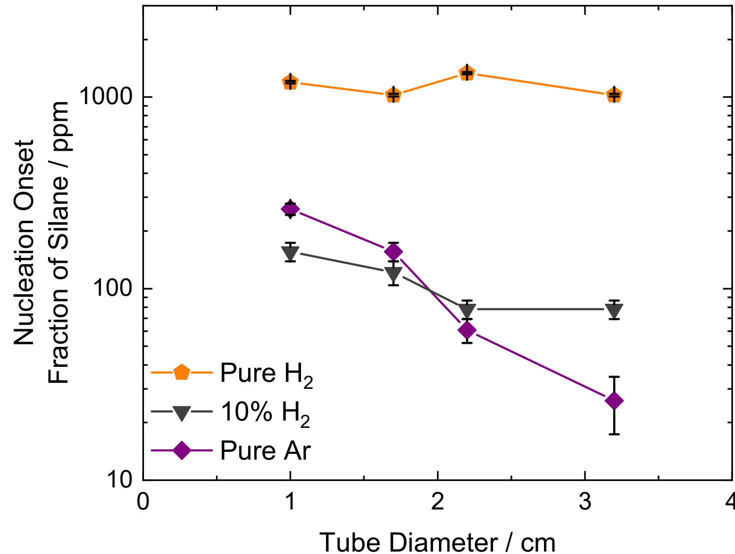

Figure 2.9. The nucleation onset fraction of silane as a function of reactor tube diameter for various balance gases. The reactor pressure was 6.5 Torr. The bottom and top of the error bars represent the reactor inlet silane fractions at which the measured deposition rate was below and above the nucleation threshold respectively.

2.3.3 The Effects of System Parameters on Particle Formation - Modelling

The computer model *GlobalKin* was used to further investigate the effects of changing reactor operating conditions on the nucleation and growth of silicon nanoparticles. The inlet gas mixture was flowed at 52 sccm with a small fraction (70-1000 ppm) of silane in argon through tubular reactors having varying diameters (1.0 cm, 1.7 cm, 2.2 cm, and 3.2 cm). The total RF power deposited and the pressure were held constant for all cases (5 W and 6.5 Torr).

The simulated mass densities and particle radii for the neutral NP (which had the largest density) as a function of inlet silane fraction are shown in Fig. 2.10 for all reactor diameters. The reactor outlet at which point these measurements were made is located 15 cm downstream of the inlet and 10 cm downstream of the power deposition region. The experimental sampling site is

60 – 61 cm further downstream. NP losses occurring in the sampling line that connects the plasma reactor to the QCM and the collection efficiency of the QCM have not been accounted for in the model. The model results are a measure of the maximum NP production rates and expect to closely track the experimental measurements downstream.

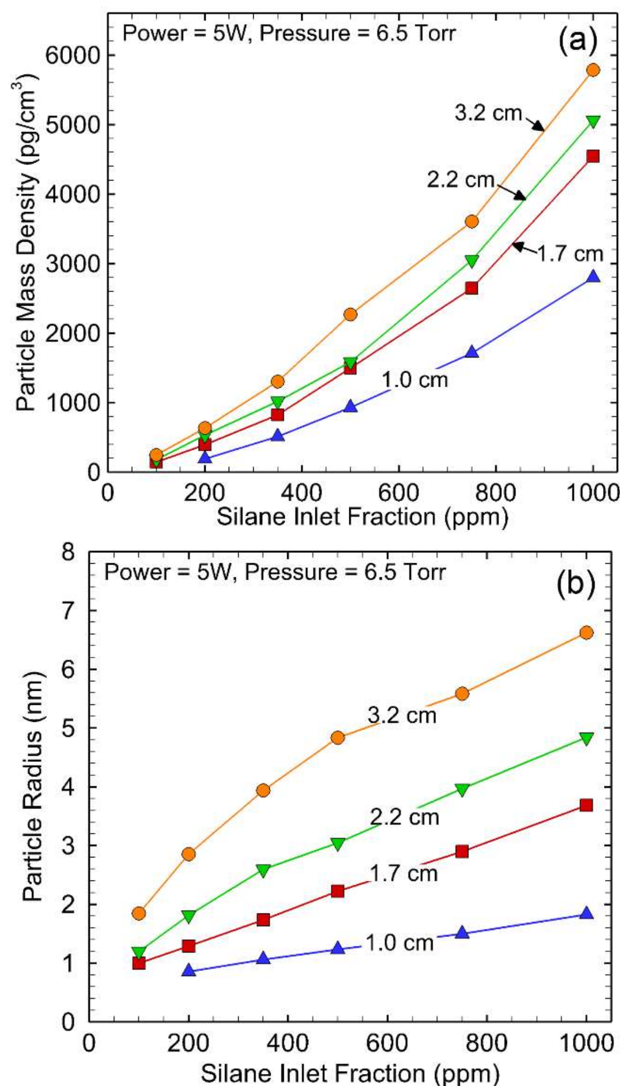

Figure 2.10. Particle mass density (a) and radius (b) predicted by *GlobalKin* as a function of silane inlet fraction in argon for different reactor diameters.

The general trends from the model closely match the experimental results of increasing mass density with increasing silane fraction. For all conditions, silane was converted to reactive precursor species within a few cm of the flow entering the power deposition zone, allowing for particle nucleation to rapidly begin. This observation is consistent with the results shown in Fig. 2.9 which suggests that onset of nucleation occurs at an inlet fraction of 200 ppm of silane or less in pure argon for all reactor sizes. In nearly all cases, silane consumption exceeded 95%.

These results suggest that NP growth is reaction limited and transport dominated. Particle number density at the outlet is higher for low silane inlet fractions than with large silane fractions. Inlet silane is depleted at roughly the same rate regardless of inlet silane fraction across all cases at the same reactor diameter. Nanoparticle number density increases in the plasma with increasing silane inlet fraction. However, at midrange silane inlet fractions (200 ppm for the 3.2 cm case) nanoparticle number density decreases downstream of the plasma as particles reach a critical cluster size and coagulate to form larger particles.

The model tracks a sequence of higher silane species and a single NP species, and the mass and radius of the NP species is calculated. Aside from the Si that may stick on the walls, the total mass (number) of Si atoms is conserved as a function of position. The distribution of that mass can be, for example, a larger number density of smaller NPs or a smaller number density of larger NPs. As long as there is a flux of silane radicals nucleating NPs at the smallest radius, the number density of NPs increases while keeping the average size of the NP small. Once nucleation (the creation of new NPs) ceases due to the depletion of nucleating radicals, growth of NPs is dominated by coagulation (NP + NP $\rightarrow$ NP), which reduces the number of NPs

while increasing the radius of the remaining NP to conserve the total mass of Si. These processes are occurring simultaneously – though one process can dominate over another.

In the low silane inlet fraction cases, the number density of particles downstream remains high, and their size is small. This indicates that the dominant process adding mass to the NPs is nucleation. Nucleation will increase the particle number density by continually supplying small particles to the system while coagulation will decrease the number density as particles combine to create larger particles. The particle size does increase somewhat, and that increase in NP diameter can be attributed primarily to coagulation. These results for the low silane inlet fraction cases suggest particles are unable to grow large enough for coagulation to dominate, meanwhile reactive precursors are lost to the wall or swept from the reactor by fluid flow.

A comparison of particle mass densities and radii across all reactor diameters at constant silane inlet fraction reinforces this observation. As reactor diameter decreases at constant inlet flow rate and pressure, the speed of the plug moving down the reactor increases. For comparison, the estimated plug speed in the 1.0 cm diameter reactor is about 150 cm/s whereas the estimated plug speed in the 3.2 cm reactor is 14 cm/s. The mass density of particles in all 3.2 cm cases is 2-3 times that in the 1.0 cm cases (3600 pg/cm^3 in the 3.2 cm reactor and 1700 pg/cm^3 in the 1.0 cm reactor at 500 ppm, for example). Due to the high rate of fluid flow in the 1.0 cm case, silane spends less time in the plasma region. However, the power deposition increases at the same rate, resulting in about the same dissociation fraction as in the 3.2 cm case. However, as noted above, decreasing the reactor diameter also decreases the effective diffusion length to the walls. Modelling results suggest that particle growth can be suppressed by decreasing reactor diameter or by decreasing silane inlet fraction, consistent with the experimental results. Film formation is most likely suppressed by increasing reactor size and adjusting silane inlet fraction above the

nucleation threshold to achieve a target particle size.

To demonstrate the potential consequences of sticking coefficients on nucleation and growth rates, two extremes were simulated with the model - a small tube (1 cm diameter) with zero and unity sticking coefficient for all radicals, and a large tube (3.2 cm diameter). The reactor conditions are a constant flow rate of 52 sccm, 5 W, 6.5 Torr and 350 ppm SiH_4. The results for particle mass density and particle radius as a function of reactor position are shown in Fig. 2.11. For a diameter of 1 cm, there is a significant increase in particle radius and particle mass density from a sticking coefficient, $s = 1$ to $s = 0$. For a diameter of 3.2 cm, there is little change in particle radius for the same change in sticking coefficient. The particle mass density increases with decreasing sticking coefficient, though less appreciably in the 3.2 cm case compared to the 1.0 cm case. For a diameter of 1.0 cm, the more rapid rate of radical loss to the walls with $s = 1$, even with a smaller residence time, results in lower net growth rates, smaller particles, and lower total particle mass density. For a diameter of 3.2 cm there is little change in the particle diameter between $s = 0$ and $s = 1$ as volumetric processes are dominating the number densities of particle precursors and growth species in the plasma zone. However, downstream, after nucleation has occurred for both cases, the $s = 0$ case produces a larger number density of smaller particles due to growth reactions of radicals onto the particles dominating over coagulation.

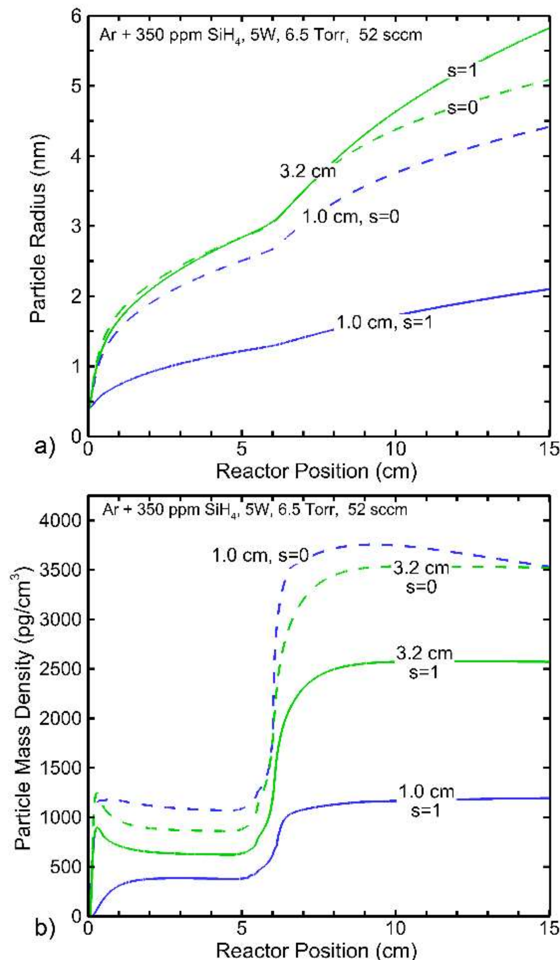

Figure 2.11. Particle properties for varying sticking coefficients. (a) Particle radius and (b) mass density for tube diameters of 1.0 and 3.2 cm for two cases of the sticking coefficient for all silane radical species, $s = 0$ and $s = 1$.

2.4 Conclusions

In this work, a QCM impactor has been shown to be a promising method for sampling aerosolized particles (of sizes below 10 nm) under vacuum conditions at low mass densities. By depositing particles on the center of a QCM crystal, rather than over the entire area, device sensitivity was shown to increase by over an order of magnitude. Using this QCM impactor, particle mass densities from the effluent of a dilute silane plasma were measured. These mass

densities were determined as a function of the inlet silane fraction, gas composition, reactor pressure, and reactor tube diameter. Increasing the reactor tube diameter was shown to significantly increase particle mass density, and increasing the reactor pressure was also shown to increase particle mass density. Particle formation was greatly inhibited when pure H_2 was used as the balance gas. These results suggest that species diffusion to surfaces that act as sinks (e.g. reactor walls) plays a major role in determining whether film formation is favored over particle formation. Reactor conditions having high hydrogen fraction suppresses both film formation, and to a greater extent, particle formation.

Experimental and modeling results indicate that diffusion of radicals and their loss on the walls can be important with respect to NP formation. When varying the sticking coefficient of silicon precursor species on the reactor walls in the model, we see similar dependencies with respect to the experiments. These dependencies could be sensitive functions of reactor radius as sticking coefficients are likely a function of reactor radius. Changes in sticking coefficient at the reactor walls would be expected as the walls are subject to heating, ion bombardment, and photo desorption over the life of the reactor. As a film is deposited on the walls, sticking coefficients may change. Further studies are needed to fully parameterize these dependencies. Results from the model suggest that controlling particle growth and film formation is a delicate balance between controlling the particle growth regime (nucleation vs. coagulation) and fluid properties. Additionally, the model results suggest that reactor diameter (which also determines residence time for a given flow rate) should be tuned in combination with inlet gas composition to either achieve a particle-free film, or particles of a specified size while also suppressing film formation on the reactor walls.

Chapter 3: Particle Trapping, Size-filtering, and Focusing

3.1 Introduction

The work in this section is the result of a large collaborative effort with contributions from Zichang Xiong, Dr. Steven Lanham, Dr. Gunnar Nelson, Dr. Mohammad Ali Eslamisaray, Jordyn Polito, Dr. Yaling Liu, Dr. John Goree, Dr. Elijah Thimsen, Dr. Mark Kushner, and Dr. Uwe Kortshagen. Original work by Eric Husmann includes the experimental and writing of the QCM impactor particle trapping results and partial contribution to overall revisions. This work has been published elsewhere [56].

The term dusty plasma refers to a weakly ionized gas containing solid particulates [104, 105]. Over the past two decades, nonthermal dusty plasmas in low pressure flowing systems have become critically important sources for the synthesis of nanoparticles and quantum dots [32, 106–110]. In these plasmas, energetic plasma electrons decompose molecular gaseous precursors, producing radicals, which lead to the nucleation and growth of nanoparticles. Based on the extreme nonequilibrium in these plasmas, with the temperature of electrons (several eV) exceeding the temperature of the gas atoms and plasma ions (near ambient) by about two orders of magnitude, dusty plasmas offer the ability to synthesize crystalline nanoparticles even of high melting point, including covalently bonded materials. This capability is due to the selective heating of nanoparticles to temperatures far above the gas temperature [32]. This mechanism enables the synthesis of nanocrystals that are commonly inaccessible to liquid phase synthesis [37, 111, 112]. Once the nanoparticles growing in the plasma reach a certain minimum size, they acquire a negative charge based on the higher mobility of free plasma electrons compared to that of plasma ions. This negative charging suppresses agglomeration of larger nanoparticles as a result of the resulting Coulombic repulsion [113, 114]. This mechanism is widely credited with the ability of plasmas to produce nanoparticles with much more monodisperse size distributions than other gas-phase approaches [32].

Dust particles immersed in plasmas are subject to a variety of forces, including electrostatic, gas and ion drag, thermophoresis, Brownian motion, and gravity [115–123]. The relative magnitude of each force depends on the size of the particle and the plasma conditions. The plasmas of interest here are produced by application of radio frequency (RF) voltages, typically sustained in cylindrical reactors of up to a few cm in diameter and 10-15 cm length, operating at pressures of a few Torr with nominal power deposition of up to about 50 W. The electrostatic force originates from the negative charge acquired by dust grains and the electric fields in the plasma. These electric fields are either ambipolar in nature, self-generated to confine the highly mobile electrons in a way that the plasma bulk is charged slightly positively compared to the surrounding reactor walls, or due to applied voltages, which for the plasma of interest produce moderate electric fields of only a few V/cm in the bulk plasma and hundreds of V/cm in the bounding sheaths. In dusty plasmas containing micron-sized particles, particles can carry many thousands of elementary charges and electrostatic forces produced by the RF sheaths at the plasma boundary can be strong enough to balance the gravitational and ion drag forces, leading to particle levitation and trapping close to the plasma boundary sheath [105, 124]. In semiconductor processing, this trapping of particles was recognized as a problem as early as the 1990s [125], as dust particles that form during plasma processing can accumulate in these electrostatic particle traps and then drop onto the wafer being processed after the plasma is turned off.

Plasma reactors used for nanoparticle synthesis are fundamentally different from reactors used in semiconductor processing and those typically used to study the fundamental properties of dusty plasmas which are parallel plate, capacitively coupled systems [106, 107, 126, 127]. As noted above and shown schematically in Fig. 3.1a, the plasmas typically used for nanoparticle synthesis are based on tubular laminar flow reactors, in which a plasma is excited either by capacitive or inductive coupling of RF power. Gas flow rates are commonly large so that the gas residence time in the reactor is on the order of milliseconds in order to limit particle growth to the nanometer size range.

For nanometer-sized particles, gravity does not play a significant role. Trapping, if it were to occur, would be the result of the balance between the electrostatic force and opposing forces such as the drag of the flowing neutral gas, the ion drag, and the thermophoretic force

[115, 128]. In this context, trapping refers to nanoparticles which are temporarily quasi-stationary within the reactor and which continue to grow by reactions with radicals while in the trap. Particles are, indeed, collected as they flow out of the reactor so any trapping would be temporary or dynamic. However, to date, the likelihood and leveraging of particle trapping in the synthesis of nanoparticles with diameters of less than tens of nm has not been either realized or acknowledged. This lack of acknowledgement has resulted mainly for two reasons:

- The high concentration of nanoparticles during particle nucleation: During the initial nanoparticle nucleation event, the concentration of nanoparticles of less than a few nm in diameter commonly can exceed that of positive ions and plasma electrons by more than an order of magnitude [114]. These conditions imply that the average charge of nanoparticles in a plasma is less than one elementary charge. While the nanoparticle charge fluctuates stochastically due to the random collection of electrons and ions [113], nanoparticles are neutral for a significant fraction of time while in the plasma. (Large particles with sizes exceeding many tens of nm will be permanently negatively charged.) With particles of a few nm being neutral for long periods of time, they would presumedly not be subject to electrostatic trapping while still being subject to neutral drag and thermophoretic forces.
- In many studies, it has been found that the average nanoparticle size correlates nearly linearly with the residence time of particles in the plasma (and inversely with the gas flow velocity) [45]. These observations have been interpreted to mean that particles, while growing, travel through the reactor with the gas flow akin to a plug flow reactor and that the particle position in the reactor varies with time in a linear fashion. These processes are schematially shown in Figs. 3.1b and 3.1c.

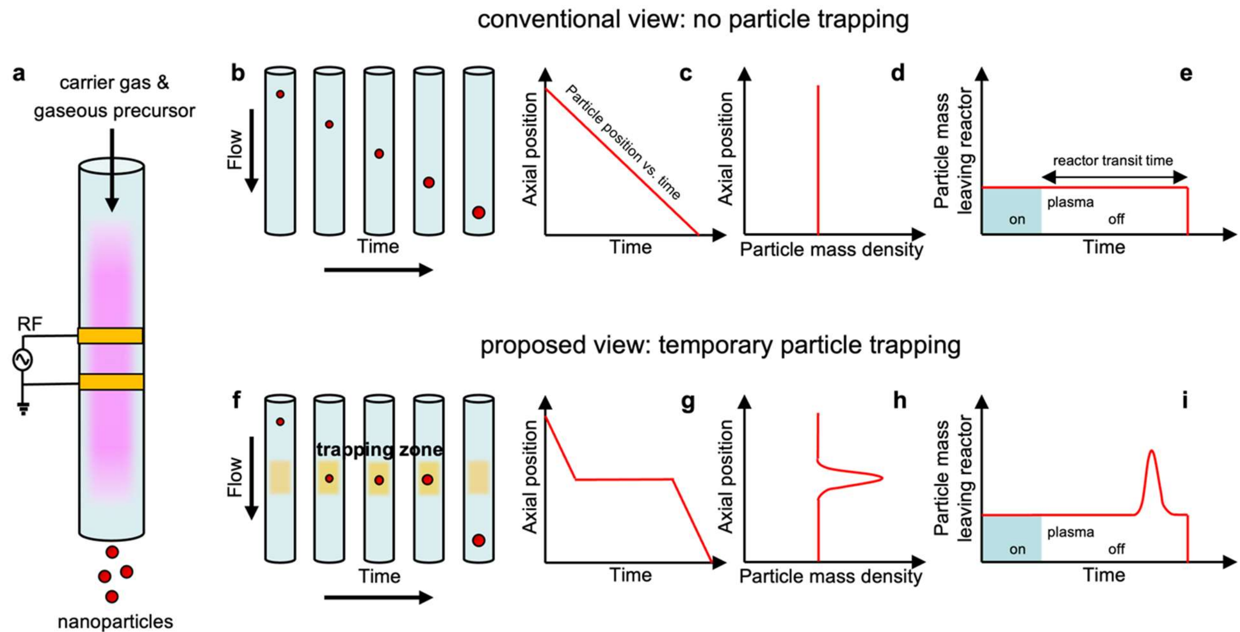

Figure 3.1. Overview of two scenarios of particle growth in nonthermal plasmas without and with particle trapping. (a) Schematic of laminar flow plasma reactor for nanoparticle synthesis. (b-e) Scenario without particle trapping and (f-i) with particle trapping. In the untrapped scenario (b-e) the particles flow through the reactor at a constant velocity as they continue to grow by reactions with radicals. Under the assumption of negligible radial losses to the reactor walls, the particle mass density, defined as the mass density of particles and unreacted precursor, is therefore constant along the reactor. When the plasma is extinguished, particle mass leaves the reactor at a constant rate until one transit time after the plasma turn-off. In the trapped scenario (f-i), the particles become temporarily trapped while continuing to grow, leading to a locally enhanced mass density in the trapping zone. When the plasma is turned off, removing the trap, this larger mass density is released and will appear as a peak in the rate of particle mass leaving the reactor.

There have been limited reports of nanoparticle trapping during plasma synthesis. Nanoparticle trapping was observed in a laminar flow reactor with small gas flow speeds through the tube geared towards synthesizing large nanocrystals of several tens of nanometers in diameter [129]. This observation, *a priori*, was not inconsistent with the above reasoning because such large nanoparticles carry several tens of elementary charges and, despite stochastic charge fluctuations, are likely negative all of the time. Furthermore, the gas drag that acts to remove particles from the electrostatic traps was small due to the low flow speeds. A recent simulation study was the first to point to the possibility of trapping of particles even in the sub-10 nm regime [130]. While these simulations did not model the high particle concentrations that are

present in actual synthesis reactors, they clearly indicated that even small particles that are electrically neutral for a fraction of their time in the plasma can experience trapping.

The present study provides the first experimental evidence, with computational verification, of the trapping of sub-10 nm particles during particle synthesis and introduces a new paradigm of utilizing trapping in nonthermal plasma synthesis for the size filtering of nanoparticles. The demonstration system is the growth of Si nanoparticles using Ar/SiH_4 gas mixtures in RF sustained plasmas at pressures of 1.1 - 6.5 Torr and powers of 5-20 W. Trapping was independently observed in multiple different reactor set-ups by two different research groups using different experimental techniques to analyse the presence of trapped particles. Experimental results were interpreted based on parametric Monte Carlo simulations and verified with full scale plasma reactor simulations.

3.2 Experimental Approach and Reactors

In situ detection of trapped sub-10 nm particles poses great difficulties. For larger particles, visible laser light scattering (LLS) is widely used [105, 124]. However, the scattered intensity for LLS rapidly becomes untenably small as the particle size is reduced. In particular, the Rayleigh scattering cross section scales with the sixth power of the particle diameter [131]. To overcome this unfavorable scaling, the only *in situ* detection method that we know of and that provides good sensitivity for particles smaller than 10 nm, is a destructive method – laser induced particle explosive evaporation (LIPEE) [132]. In this method, the diagnostic is not elastically scattered laser light, but rather the thermal glow from particles that are suddenly heated and evaporated by a pulsed laser. This LIPEE method has not been widely used in the dusty plasma literature since it was reported in 1994. This lack of use is perhaps due to the

equipment that is required, which includes a powerful pulsed ultraviolet laser along with sensitive high-speed optical detection. For these reasons, our approach relies not on *in situ* detection of the particles, but instead on *ex situ* measurements.

Our experimental approach is based on the scheme detailed in Fig. 3.1 utilizing a time-resolved measurement of the particle mass at the exit of the reactor. For simplicity, we neglect in this figure the influence of radial losses of particles and chemical precursors, which occurs in an actual reactor, but will not significantly affect the argument that we present. If particle trapping during synthesis does not occur, the currently predominant view, particles move through the reactor with time in a linear fashion following the gas flow (Fig. 3.1b,c) while growing by reactions with the locally available precursor radicals. When radial losses are neglected, the particle mass density, defined by the mass density of the forming nanoparticles and that of the unreacted precursor, is constant along the reactor (Fig. 3.1d). Towards the exit of the reactor, the majority of the mass that has been transformed into particles can be collected and their mass measured. If the plasma is turned off, particle formation ceases and the collection of particles ceases after one gas transit time through the reactor following the moment of plasma turn-off (Fig 3.1e).

Particle trapping significantly changes this picture. If nanoparticles are temporarily trapped, their motion through the plasma reactor is no longer linear in time (Fig. 3.1f,g). Particles are temporarily confined in a trapping zone but continue to grow due to the presence of the radical precursors. The electrostatic trapping force is roughly proportional to the particle diameter. However, in the Knudsen number range of relevance to low pressure processing, the gas drag force is proportional to the square of the particle diameter [133]. As a result, particles will be forced from the trap once they reach a critical size when drag by the gas flow dominates.

However, since particles are temporarily stopped in their motion through the reactor, the particle mass density within the trapping zone exceeds that of the particles outside the trapping region (Fig. 3.1h). If the plasma is turned off and the particle mass at the reactor exit is measured, the trapped particles will appear as a peak in the particle mass leaving the reactor after the plasma is turned off (Fig. 3.1i).

To evaluate these two scenarios, three different plasma reactors were designed using different experimental methodologies to measure the particle mass leaving the reactor over time. The reactors are shown schematically in Fig. 3.2. The first reactor was resident at the University of Minnesota (UMN1). The plasma was generated by applying capacitively coupled RF power (frequency 13.56 MHz) to the quartz tubular reactor 2.5 cm external diameter (2.2 cm internal diameter) and 20 cm long. The power was applied with a pair of ring electrodes 1 cm wide and separated by 2 cm at their centers. The operating conditions for the base case are an RF power of 20 W, flow rate of Ar/He/SiH_4 = 30 sccm/4.75 sccm/0.25 sccm and gas pressure of 1.1 Torr.

The nanoparticle cloud resulting from plasma synthesis was sent through a slit-shaped nozzle (0.5 mm × 12 mm) at the reactor exit and focused into a curtain-shaped beam of nanoparticles. These particles were deposited on a glass or silicon substrate that was translated through the nanoparticle beam at a constant velocity by a linear DC servomotor.

The deposited particle mass was evaluated by measuring optical absorption of the particles deposited on a transparent glass substrate moving at a constant speed of 5 mm/s. The plasma was turned off during the substrate translation to collect both particles leaving the reactor in steady state operation and trapped particles. The substrate with deposited silicon nanoparticles was then placed on one exit port of a Labsphere 10 cm integrating sphere, illuminated with a 390

nm LED, and imaged using a digtal camera (NIKON D7100). Raw files were converted to 16-bit TIFF format and the transmitted light intensity was measured as line intensity plots in ImageJ, using a bare glass substrate as a baseline. Absorbance was obtained as $A = -\log{(I_t/I_0)}$, where I_t is the transmitted light intensity, I_0 is the incident light intensity.

The delay time of the arrival of the trapped particles at the substrate after turning off the plasma was measured by a 240 fps camera (iPhone 12, Slo-mo mode). Accuracy of the arrival time was estimated as ±1 frame (1/240 s). The axial trapping position was determined by multiplying the arrival time by the gas flow velocity, which was determined by fitting particle arrival times versus the different axial positions of the electrode pair

A second reactor similar in design to UMN1, also resident at the University of Minnesota was used to evaluate the consequences of particle growth on precursor density and deposition on the walls of the reactor. This reactor, UMN2, was a quartz tubular reator having two diameters. The power was applied to the narrower portion of the tube, 0.7 cm internal diameter. The tube expanded downtream to 2.2 cm internal diameter. The plasma conditions were a gas pressure of 0.8-0.9 Torr and gas mixture of Ar/He/SiH_4 that was varied from 30/6.65/0.35 sccm to 30/13.3/0.7 sccm. RF power of 50 W was applied to a pair of 1cm wide electrodes, separated by 2 cm center-to-center, that was located 2 cm upstream of the tube expansion.

The third reactor was resident at Washington University in St. Louis (WUSTL). Similar to the UMN1 reactor, the plasma was generated by applying capacitively coupled RF power (frequency 13.56 MHz) to the quartz tubular reactor 3.2 cm internal diameter. The power was applied with a pair of aluminum ring electrodes 1.4 cm wide and separated by 2.65 cm at their centers. The operating conditions for the base case are an RF power of 5 W, flow rate of

$Ar/He/SiH_4$ = 51 sccm/0.991 sccm/0.009 sccm and gas pressure of 6.5 Torr. Following the reactor, 2.7% of the total flow was diverted to a quartz crystal microbalance (QCM) impactor. A 150 μm orifice was used to impact synthesized particles onto the quartz crystal. The mass loading on the quartz crystal was determined using the Sauerbrey equation [134]:

$$\Delta m = -\Delta f \left(\frac{A\sqrt{\rho_q \mu_q}}{2 f_o^2} \right) \tag{3.1}$$

where Δm is the change in the mass loading of the quartz crystal, Δf is the change in the quartz crystal resonance frequency, A is the effective crystal area (6.5 mm), ρ_q is the density of the quartz crystal (2.65 $g \cdot cm^{-3}$), μ_q is the shear modulus of the quartz crystal ($2.95 \cdot 10^{11}$ $g \cdot cm^{-1} \cdot s^{-2}$), and f_o is the resonant frequency of the fundamental mode of the quartz crystal (6 MHz).

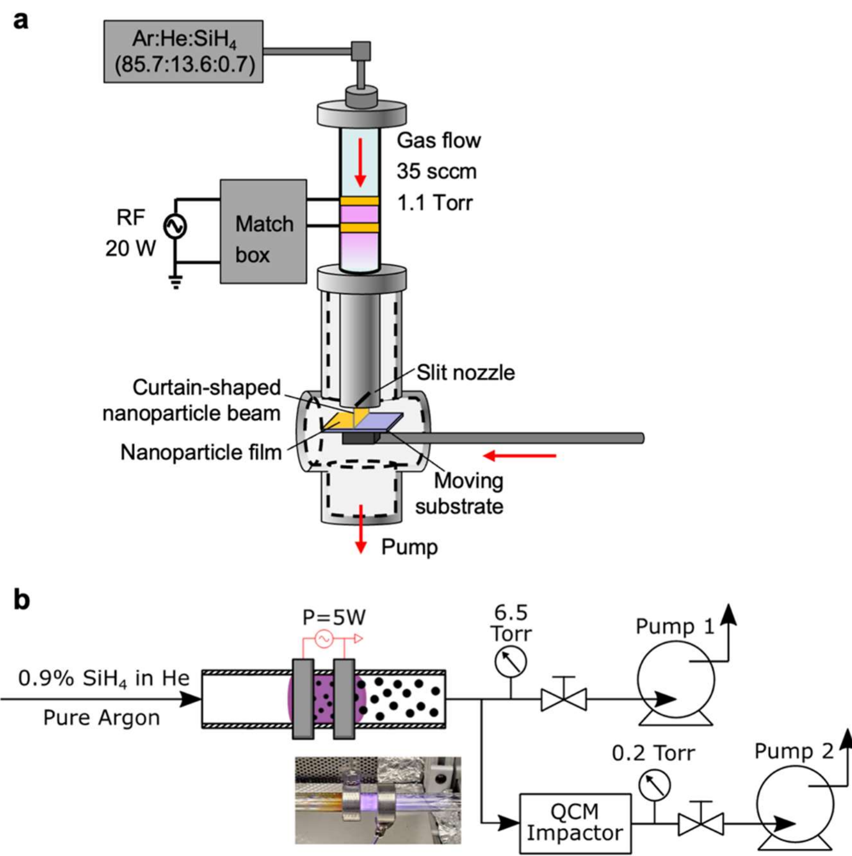

Figure 3.2. Schematics of two of the two plasma reactors used to investigate particle trapping. (a) Schematic of the UMN1 plasma synthesis reactor used to deposit silicon nanocrystals on a moving substrate. The deposited particle mass is analyzed by studying the optical absorbance of the particles on the substrate. (b) Schematic of the WUSTL plasma synthesis reactor. In this reactor, particle mass leaving the reactor is directly measured using a QCM.

Transmission electron microscope (TEM) imaging of the collected particles was performed using an FEI Talos F200x operating at an accelerating voltage of 200 kV as well as an FEI Tecnai T12 operating at 120 kV. To determine particle size distributions, nanoparticles were deposited directly onto thin holey carbon coated Cu TEM grids translated under the curtain-shaped particle beam in reactor UMN1. The diameters of 300 particles were then measured with ImageJ and their size distribution fit to a log-normal size distribution.

3.3 Observations of Nanoparticle Trapping

Silicon nanoparticles deposited on a silicon substrate translated with constant velocity under the exit nozzle of the UMN1 reactor are shown in Fig. 3.3a. Initially, the particle deposition is essentially uniform (except for some nonuniformities caused by the not entirely constant speed of the motor drive). After turning off the plasma and emptying of the electrostatic trap, the deposition of a significantly larger amount of particles was observed corresponding to the arrival of trapped particles, consistent with the scenario described in Fig. 3.1f-i. After the arrival of the trapped particles, the deposition of additional particles was observed corresponding to particles that were upstream of the trapping zone when the plasma was turned off. The curvature of the deposition in vertical direction is assumed to be caused by the laminar flow in the reactor with there being little slip at the surface of the tube. There conditions result in the gas close to the reactor wall to have a lower flow speed than at the center of the tube. The amount of mass corresponding to the trapped particles is about five times that of the particles leaving the reactor in steady state, shown in Fig. 3.3b. The experiment was repeated for three different axial positions of the electrodes that would in turn determine the location of the electrostatic trap. From the delay of the arrival of the trapped particles with respect to the moment of plasma turn-off, the gas flow velocity was determined which then enabled the computation of the axial position of the trapped particles. As shown in Fig. 3.2c, the trapping zone is located about 1.6 cm below the powered top electrode.

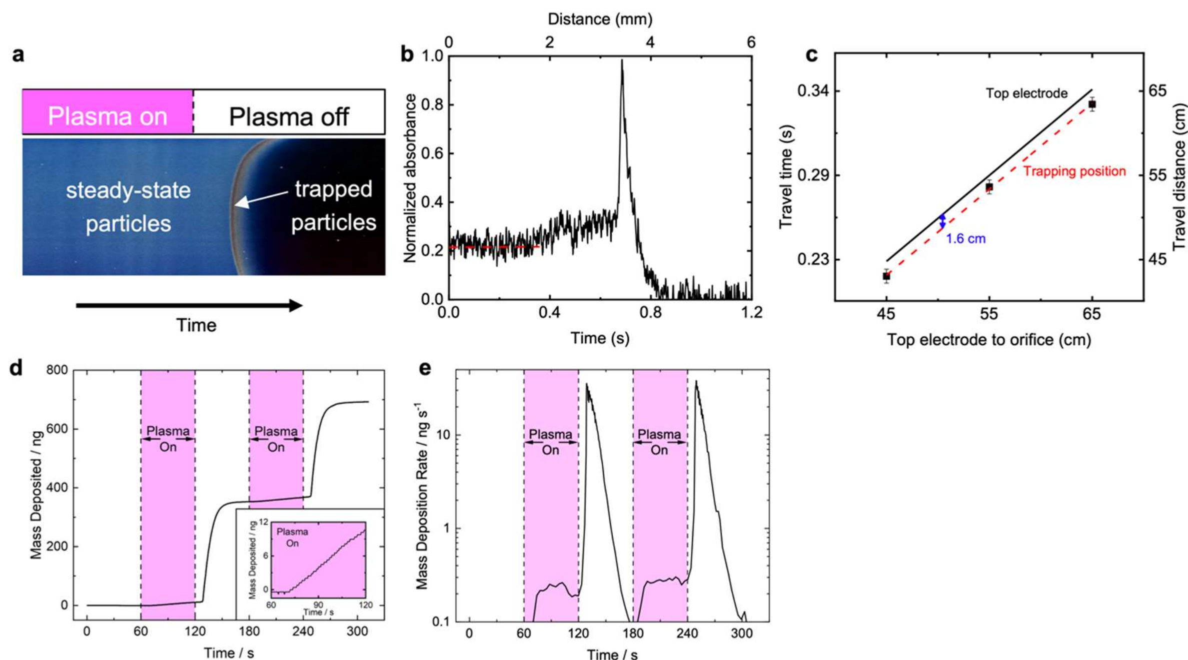

Figure 3.3. Experimental results demonstrating particle trapping in the synthesis of sub-10 nm silicon particles. (a-c) Results from the UMN1 reactor. (a) Photograph of particles deposited on a silicon substrate (to enable better photographic imaging) moving at constant speed below the reactor exit showing the deposition peak associated with trapped particles. (b) Absorbance of 390 nm light by silicon nanoparticles on the translated glass substrate. (c) Position of trapped particles derived from arrival time of particles after plasma turn-off for three different electrode positions. (d-e) Results from WUSTL plasma reactor. (d) Particle mass deposited on a quartz crystal microbalance over time and e) particle mass deposition rate.

Results from the WUSTL plasma reactor, which was operated at significantly higher pressure than the UMN1 reactor, are shown in Fig. 3.2d,e. In this reactor, the arrival of particles after leaving the reactor was significantly delayed due to the low flow rate in the gas lines leading to the QCM. A significant increase in the deposited mass after plasma turn-off, indicative of the arrival of trapped particles, is shown in Fig. 3.2d. The mass deposition rate after plasma turn off was almost 2 orders of magnitude larger than the deposition rate during the steady-state plasma on phase, as shown in Fig. 3.2e. This result suggests that the particle mass density in the particle trap is about a factor of 100 times larger than that outside of the trap. These results demonstrate that plasma parameters such as pressure and flow rates can be used to control the

amount of particle mass that is trapped compared to that leaving in steady state.

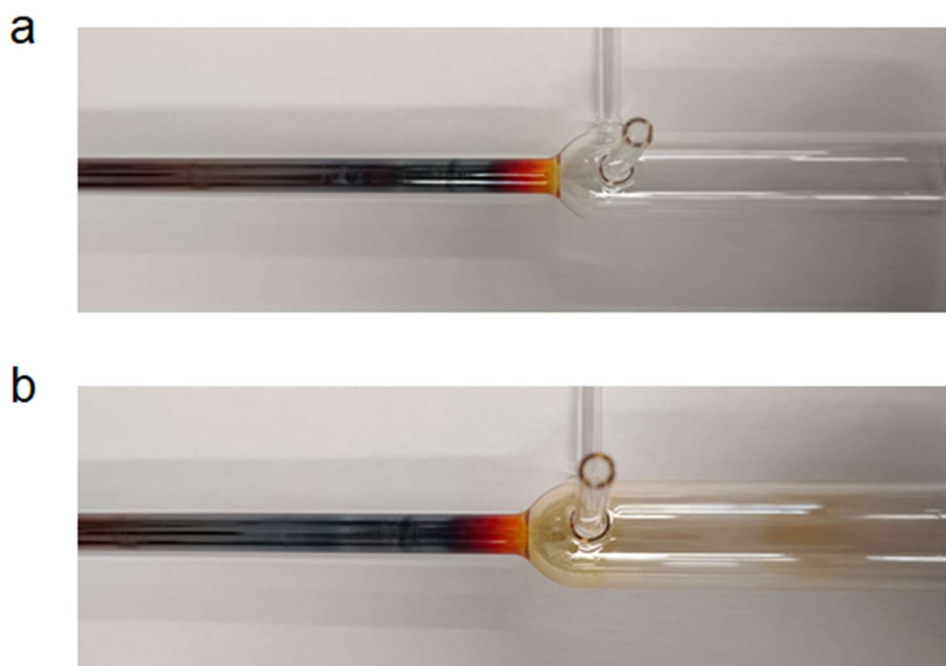

Figure 3.4. Images of the UMN2 reactor used for silicon quantum dot synthesis. The electrode pair was located 2 cm to the left of the tube expansion. a) Photograph of a plasma reactor run with a silane flow rate (Ar/He/SiH4 = 50/13.3/0.7 sccm) that leads to the formation and collection of ~3 nm Si quantum dots. Note that deposition of a parasitic silicon film is only observed upstream (left) of the electrodes but not downstream (right) of the electrodes. This observation is consistent with the assumption that trapped particles around the electrode position act as sink of silicon precursor, preventing silicon film deposition downstream of the electrodes. b) Photograph of the same plasma reactor operated at lower silane flow rate (0.35 sccm) so that particle nucleation and collection is avoided. Note that film deposition now also occurs downstream of the electrodes, suggesting that the precursor sink due to trapped particles is removed, because the precursor density is too low for particle nucleation.

It is also instructive to consider the deposition of a silicon film on the reactor walls, which occurs in actual reactors as an unwanted loss process of radicals, but was neglected in our simplified argument illustrated in Fig. 3.1. The silicon film deposition in a third plasma reactor, similar in design to the UMN reactor, which is typically used for the synthesis of sub-5 nm silicon particles, is shown in Fig. 3.4. For the higher flow rates associated with silicon nanocrystal formation (Ar/He/SiH_4 = 50/13.7/0.7 sccm), the deposition of a silicon film on the reactor walls is limited to the region upstream of the electrodes. If the silane precursor flow rate

is lowered to a level that particle nucleation does not occur ($Ar/He/SiH_4$ = 50/6.65/0.35 sccm), and no particles are collected, the silicon film deposition is observed both upstream and downstream of the RF electrodes. These observations are consistent with the hypothesis that nanoparticles are trapped close to the RF electrodes at the higher silane flow rate. The trapped particles likely act as a sink for the silane precursor that leads to an almost complete precursor consumption in the region upstream and up to the RF electrodes. In the case of the lower silane flow, no particles form and the strong precursor sink around the electrodes is removed, leading to silicon deposition also downstream of the electrodes.

3.4 Evidence of Size Filtering

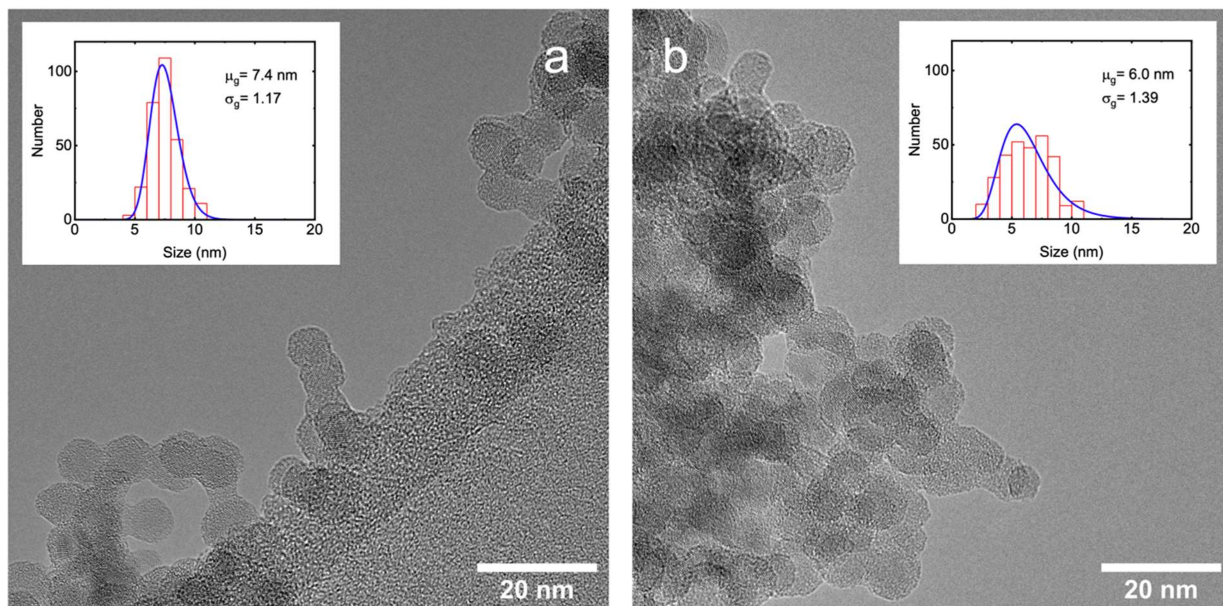

Figure 3.5. Particle trapping acting as a size filter in the nanoparticle synthesis with nonthermal plasmas. Transmission electron micrographs of silicon nanocrystals and associated size distributions (insets). a) Particles that exit the plasma reactor in steady state and b) particles that are representative of those collected from the trapping region after plasma turn-off.

The sole observation of particle trapping during nonthermal plasma synthesis may be viewed as an interesting outcome of the plasma dynamics. However, its importance is significantly deeper because particle trapping acts as an inherent size filter in the plasma synthesis as particles need to reach a certain critical size before they can escape the particle trap. This concept is demonstrated in Fig. 3.5a which shows a transition electron microscope (TEM) image of particles that are leaving the reactor in steady state operation. These are the particles that were trapped and grew to a size so that the gas drag overcame the electrostatic trapping force and liberated the particles from the trap. More than 300 particles were counted and their size distribution fit with a log-normal distribution with a mean size of 7.4 nm and a geometric standard deviation of 1.17. This geometric standard deviation is typical for nonthermal plasma synthesis but significantly smaller than those achieved in other gas-phase syntheses where nanoparticles are neutral and not prevented from agglomerating [135, 136]. Particles are shown in Fig. 3.5b that were collected after the plasma turn-off and that are representative of the trapped particle deposit shown in Fig. 3.3a. These particles exhibit a significant population of smaller particles that is not present in the particles that are collected in steady state. Accordingly, the log-normal size distribution of trapped particles has a mean size of 6 nm and a geometric standard deviation of 1.39. To our knowledge, this is the first demonstration of trapping acting as a size filter during the nonthermal plasma synthesis of sub-10 nm particles. Understanding this aspect may open new routes to designing plasma processes with even better size and composition control.

3.5 Parametric Monte Carlo Simulation of Particle trapping

Particle charge and particle trajectories were simulated with a one-dimensional Monte Carlo code implemented in MATLAB, shown schematially by Fig. B.1 in Appendix B. In this simulation, pseudoparticles of a specified diameter are initiated at the entrance to the plasma reactor. Their size is kept constant during the simulation. Their trajectories are integrated in time until they leave the reactor. An important input for this simulation is the time-averaged axial electric field profile, as the nanoparticles are too massive to follow the instantaneous RF electric field. An approximate electric field profile was derived by performing Comsol simulations for a pure argon plasma, as shown by Fig. B.2 in Appendix B. The time averaged electric field derived from these simulations, Fig. B.2d, was approximated by the simplified profiles in Fig. B.2e.

The simulation ran cyclically with a time step Δt of 100 ns. At every time step, a new position and charge for a particle was calculated. The initial particle had no charge and had a position of 10 cm from the outlet. Orbital motion limited theory [137] was then used to calculate collision frequencies of the particle with ions and electrons [138]:

$$\begin{aligned} \nu_{e,i} &= n_{e,i} S \left(\frac{k_B T_{e,i}}{2\pi m_{e,i}}\right)^{\frac{1}{2}} \exp\left(-\frac{q_{e,i}\Phi_k}{k_B T_{e,i}}\right), \qquad q_{e,i}\Phi_k \geq 0\,, \\ &= n_{e,i} S v_{e,i} \left(1 - \frac{q_{e,i}\Phi_k}{k_B T_{e,i}}\right), \qquad q_{e,i}\Phi_k < 0, \end{aligned} \tag{3.2}$$

where $S = 4\pi R_p^2$ is the particle surface area, $n_{e,i}$, $m_{e,i}$ and $T_{e,i}$ are density, mass and temperature of electrons and ions, respectively. $q_{e,i}$ represents ∓e (with e the elementary charge) for electrons and ions, respectively. k_B is the Boltzmann constant. $\Phi_k = Z_k/4\pi\epsilon_0 R_p$ is the surface

potential of a particle with radius R_p which carries a charge $Z_k = ke$ (with k an integer), with ϵ_0 the vacuum dielectric constant. The probabilities of a particle colliding with an electron or and ion are $P_{e,i} = \Delta t \nu_{e,i}$. A specific event (collision with an ion or an electron) was chosen according to random Monte Carlo sampling. The contribution of negative ions to particle charging is neglected in the Monte Carlo simulations. In nanoparticle-forming argon-silane plasmas it has been observed that negative ions are consumed in particle nucleation and their density is often on the same order as the free electron density [139]. Hence, their contribution to the negative charging current is small.

The electrostatic force acting on a particle is $\overrightarrow{F_E} = \vec{E} Z_k$, where $\vec{E}$ is the electric field. The gas drag force in the free molecular regime is $\overrightarrow{F_D} = \left(\overrightarrow{v_g} - \overrightarrow{v_p}\right) \frac{4}{3} \rho_g \bar{c}_{gas} 1.36 \pi {R_p}^2$ [140], where $\overrightarrow{v_g}$, $\overrightarrow{v_p}$ are velocities of gas and the particle respectively, ρ_g is the gas density and $\bar{c}_{gas} = \sqrt{\frac{8 k_B T_g}{\pi m_g}}$ is the average speed of gas molecules, with T_g the gas temperature and m_g the mass of gas molecules.

The Störmer-Verlet method [141] was applied to determine the particle trajectory. Given an initial position $\vec{z}_1$ and velocity $\vec{v}_1$, the particle position is advanced by a timestep Δt to a new position $\vec{z}_2$ using:

$$\vec{z}_2 = \vec{z}_1 + \vec{v}_1(\Delta t) + \frac{(\overrightarrow{F_E} + \overrightarrow{F_D})_1}{2 m_p} (\Delta t)^2, \tag{3.3}$$

where m_p is the particle mass. Subsequent particle positions are found from

$$\vec{z}_{n+1} = 2\vec{z}_n - \vec{z}_{n-1} + \frac{(\overrightarrow{F_E} + \overrightarrow{F_D})_n}{m_p} (\Delta t)^2. \tag{3.4}$$

The particle velocity at each time step is evaluated as

$$\vec{v}_{n+1} = \frac{\vec{z}_{n+1} - \vec{z}_n}{\Delta t}. \tag{3.5}$$

A single Monte Carlo simulation was run for 5×10^6 timesteps.

Results of the model are shown in Fig. 3.6. With the exception of the results shown in Fig. 3.6f, simulations were performed for a typical positive ion density n_i of 5×10^{11} cm^{-3} and a free electron density n_e of 5×10^9 cm^{-3} resulting in an electronegativity $n_i/n_e = 100$. This degree of electronegativity is consistent with previous work on dusty plasmas forming silicon particles [142, 143]. Plasma electrons can dissociatively attach to silane or directly attach to radicals to form negative SiH_x^- ions and attach to the nanoparticles, whose density can exceed the positive ion density. The fraction of time that nanoparticles of three different sizes are in a certain charge state is shown in Fig. 3.6a. Particles with a diameter of 1 nm are neutral or positively charged 78% of the time, while larger 5 nm particles are neutral 31% of the time. As a result of the long times that particles are neutral, one might conclude that small nanoparticles may not be trapped in the plasma.

The typical charging times are compared with the gas transit time through trapping region in Fig. 3.6b, defined by the pink shaded region in Fig. 3.6c with a length of about 1 cm. In this region, the electrostatic force opposes the gas drag force and increases up to a maximum at z=4 cm. Particle charging is so fast that neutral particles are likely to become negatively charged again before they are convected out of the trapping zone. As a result, particles remain trapped, even if they are charged negatively only for a fraction of the time.

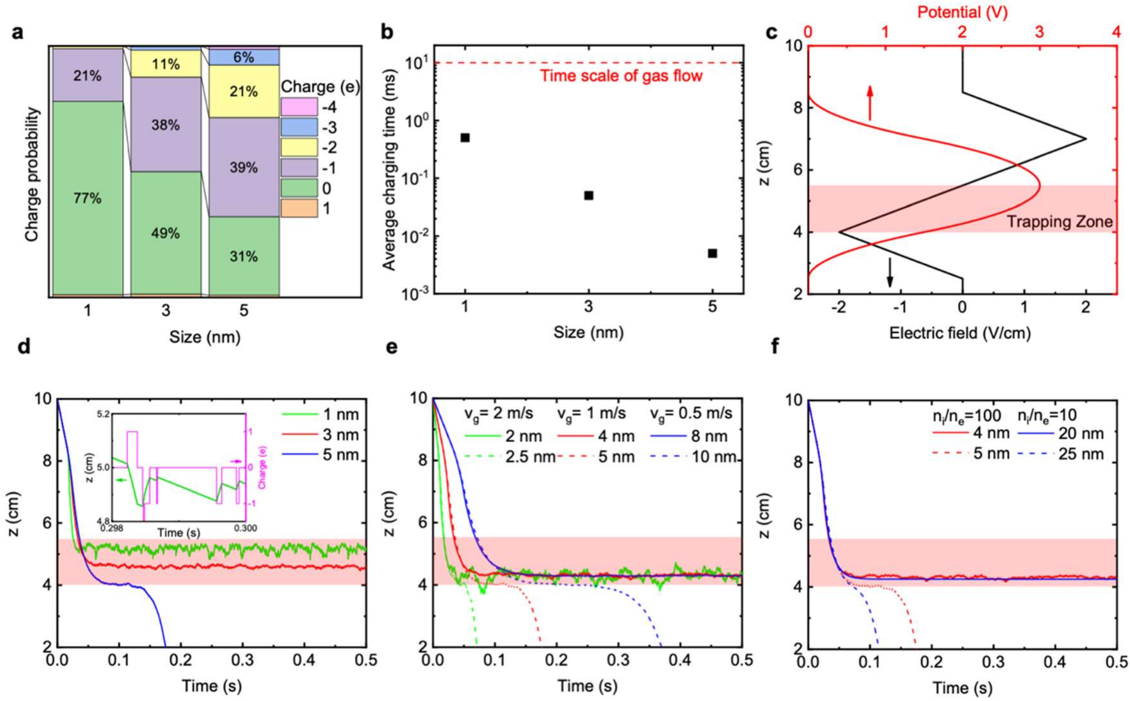

Figure 3.6. Parametric Monte Carlo model results of particle trapping. All results except (f) are for a positive ion density, n_i, of $5\cdot10^{11}$ cm^{-3} and a free electron density, n_e, of $5\cdot10^{9}$ cm^{-3}. (a) Fraction of time that particles are found in a certain charge state for three different particle sizes. (b) Comparison of the typical charging times with the time scale of the gas flow through the trapping zone. (c) Electrostatic potential profile and electric fields. (d) Axial position of particles at three different diameters as function of time. The insert shows the particle trajectory and its correlation with the fluctuating particle charge for a 1 nm particle. (e) Influence of the gas flow velocity on the critical size for particle trapping. (f) Influence of plasma electronegativity on the critical size for particle trapping.

The trapping of particles in spite of their transient neutral states is demonstrated by the results in Fig. 3.6d, which shows the axial locations of 1 nm, 3 nm and 5 nm particles with time for a gas flow velocity of 100 cm/s. The smallest 1 nm particles enter the trapping zone and their position fluctuates in the axial direction as the particle charge changes. This is shown in the inset in Fig. 3.6d, where particles follow the gas flow when they are neutral, but are drawn upstream again when they acquire a negative charge. For these conditions, 1 nm particles remain trapped indefinitely. Somewhat larger 3 nm sized particles behave similarly, but they assume a position deeper in the particle trap, because they require a larger electrostatic force to balance the gas

drag force. Particles with a 5 nm diameter are not confined in the trap. The particles are slowed down by the electrostatic force, but the force is insufficient to trap the particles. In an actual plasma reactor, the particle size does not remain constant, but particles grow due to the deposition of precursor. This means that the smallest particles are initially trapped at the top of the trap at the smallest electric fields. As particles grow, they sink deeper into the trap where the electric field increases. Finally, the electric field will be insufficient to balance the increasing gas drag and particles will be released from the trap.

The influence of gas flow velocity on the critical size for particle detrapping is shown by the results in Fig. 3.6e. Since the gas drag force acting on trapped particles scales linearly with the gas flow speed, the critical size above which trapping does not occur varies inversely with the gas flow speed. The simulations reproduce the often observed linear dependence of particle size with the gas residence time in the reactor. However, the simulations suggest that the important time is not the residence time of the gas in the reactor but the extended time spent in the particle trap that allows particles to grow to larger sizes before leaving the trap.

The effect of plasma electronegativity on the critical size for detrapping is illustrated by the results in Fig. 3.6f. As electronegativity in the plasma is reduced, the critical size for detrapping increases. This is due to the increased electron density at reduced plasma electronegativty, which produces more negatively charged particles and thus enhances electrostatic confinement. Both the impact of gas flow velocity and plasma electronegativity may be important parameters for designing trapping conditions in the plasma.

3.6 Full scale Reactor Simulations of Particle Growth and Trapping

The nanoparticle and plasma dynamics leading to trapping and de-trapping of particles are functions of the spatially dependent electrostatic fields, gas flow, and particle growth rates. To investigate the influence of these processes, a 2-dimensional plasma reactor model with an embedded 3-dimensional nanoparticle trajectory and growth model were employed. The combination of the plasma reactor model, the Hybrid Plasma Equipment Model (HPEM), and the nanoparticle trajectory model, the Dust Transport Simulator (DTS) are described in detail in Ref. [130]. The HPEM provides self-consistent electric fields, gas flow profiles, gas temperatures, charged particles fluxes, and radical fluxes. The DTS uses these values to predict the trajectories, statistical charging and trapping of growing nanoparticles while including all of the pertinent forces (electrostatic forces, fluid drag, ion drag, thermophoretic forces, gravity, Brownian diffusion forces, and particle-particle Coulomb forces).

The HPEM/DTS was used to simulate the process conditions of a low pressure reactor similar to UMN1 described above, with the model cylindrical geometry shown in Fig. 3.7a. The reactor length is 90 mm and diameter 20 mm with powered and grounded ring electrodes, and gas flowing left-to-right. The pressure was 1 Torr, gas flow rate was 75 sccm, and the gas mixture was Ar/He/SiH_4=99/0.9/0.1. A frequency of 10 MHz and a power of 10 W was used for the simulated capacitively coupled plasma reactor. The electron density, electron temperature, electric potential, electric field vectors (with electric field and potential on axis) averaged over an RF cycle, are shown in Fig. 3.7. The electron density has a maximum value of 1.3×10^{11} cm^{-3} on axis at the position of the powered electrode. Due to the high conductivity of the plasma, the electron temperature is fairly constant in the bulk plasma, 3.2-3.7 eV, while extending above 10

eV in the sheath at the powered electrode. The amplitude of the applied RF voltage is 680 V with a self generated DC bias on the tube wall of -217 V, which results in a maximum time averaged electric potential of 182 V. However, again due to the high conductivity of the plasma, the time averaged voltage drop across the bulk of the plasma is < 10 V. This results in electric fields of hundreds of V/cm that are dominantly pointing outwards (confining for negative particles) at the boundaries of the plasma. The electric field along the axis at which particles are trapped is only a few V/cm.

Predictions of trapping locations for 1 nm and 3 nm particles are shown in Fig. 3.7f, i. The 1 nm particles have trapping locations on axis that are nearly at the maximum of the plasma potential (see Fig. 3.7e). This focusing of the particles onto the axis results from the electric field which predominantly points radially outwards, thus accelerating particles radially inwards. The trapping locations are strewn along the axis for about 1 cm, a result of the charging and discharging of the particles. When the particles discharge to be neutral, they drift downwards with the gas flow. When the particles recharge negatively, they drift back towards where the plasma potential is maximized. The 3 nm particles are also trapped on axis, though at a location further downstream beyond the maximum in the potential. The larger particles are more susceptible to the fluid drag forces, and become trapped where the axial electric field provides a sufficient force to counter the fluid drag, approximately 1 V/cm, which occurs downstream of the trapping location of the 1 nm particles. The trapping sites are strewn along the axis for more than 1 cm.

The average locations for particle sizes of 1 to 10 nm as a function of time are shown in Fig. 3.7h. A horizonal line (constant location) indicates that the particles are trapped. Particles falling below 1 cm are not trapped and exit the reactor. For the simulated conditions, de-trapping

occurs for particle sizes of greater than about 4 nm when the neutral gas flow drag exceeds the ability of the plasma to electrostatically confine the particles. The trapping locations are at lower axial locations for larger particles where the confining axial electric fields are larger, as indicated in Fig. 3.7e. The trends from the Monte Carlo simulations (Fig. 3.6) and those from the full 2-dimensional simulations (Fig. 3.7) are in good agreement with each other, and with the experiments.

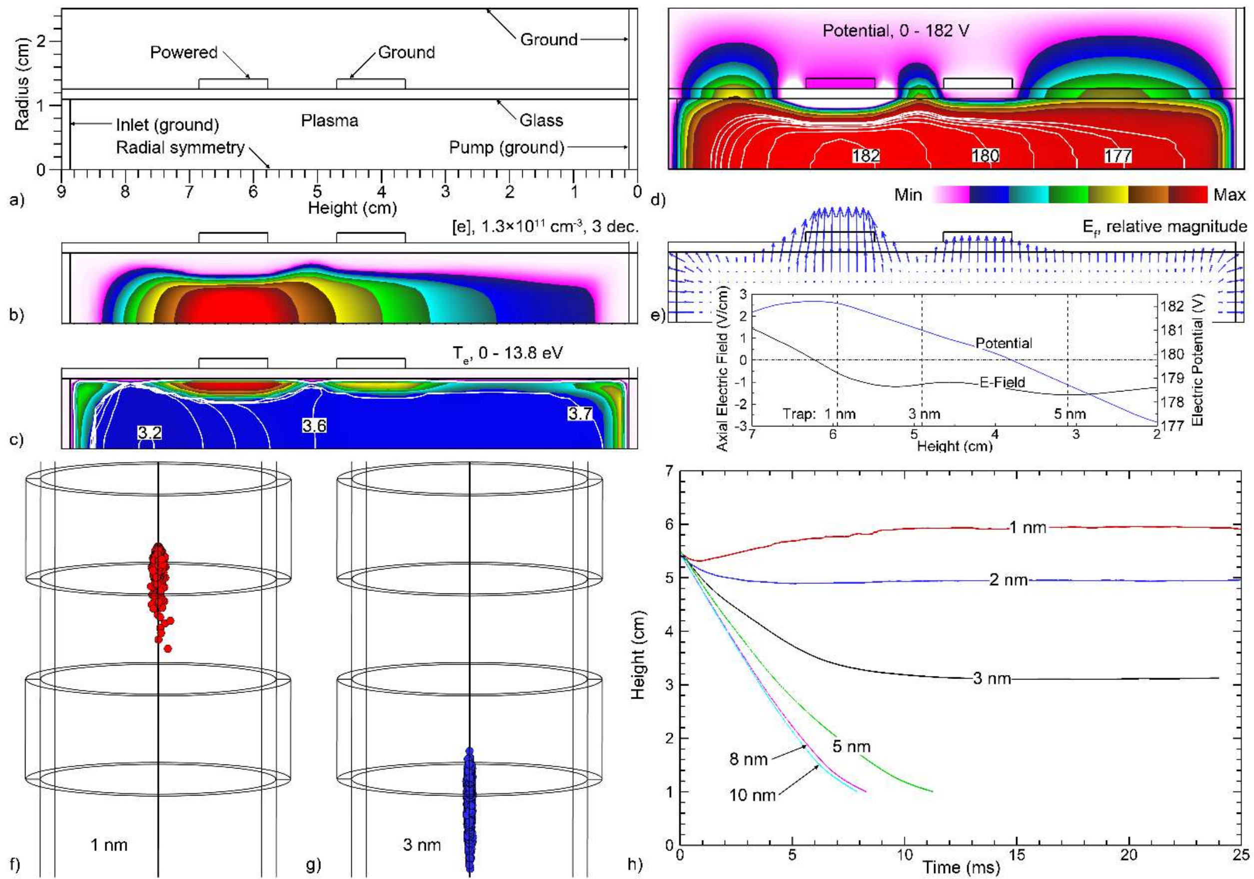

Figure 3.7. Reactor simulation and trapped particle locations. Self-consistent 2-dimensional plasma hydrodynamics simulations for operating conditions of 1 Torr, gas flow rate of 75 sccm, and gas mixture of Ar/He/SiH4=99/0.9/0.1 with capacitively coupled power deposition of 10 W at a frequency of 10 MHz. Results are time averages over an RF period. (a) Model geometry, (b) electron density, (c) electron temperature, (d) plasma (electric) potential, and (e) electric field vectors with inset showing electric field and potential along the axis. Trapping locations are shown for (f) 1 nm particles and (g) 3 nm particles. (h) Average locations of particles as a function of time. The final locations are also indicated in the insert to (e).

3.7 Concluding Remarks

In this contribution, we showed through experiments performed on multiple plasma reactors as well as simulations with different levels of completeness that particle trapping through electrostatic forces does occur during the synthesis of sub-10 nm particles, a phenomenon that has generally not been recognized to date. We demonstrated that particles are trapped even if they are neutral for the majority of time that they spend in the trapping region due to a cycle of particles discharging and recharging. In actual plasma reactors, particles enter the trapping region and are spatially confined while growing through the continued supply of precursor. Once particles reach a critical size such that the gas drag is sufficiently strong to overcome the electrostatic trapping force, particles are released from the trap. This critical size required for de-trapping narrows the collected particle size distribution since particles smaller than the critical size are confined and those that grow to larger than this critical size can escape and exit the reactor in steady state operation. Our numerical simulations suggest that the radial electric fields present in the particle trap lead to a focusing of the released particles onto the reactor centerline.

The observations reported here may establish a new paradigm for control of the nonthermal plasma synthesis of sub-10 nm particles. A better understanding of the trapping mechanism will enable a better control over particle sizes and more monodisperse size distributions than has been possible to date. The existence of trapping is of particular importance for the design of reactors for core-shell heterostructured nanoparticles [112, 144–146]. A better understanding of trapping will enable researchers to design plasma processes in which nanoparticles are either trapped or not trapped in the shell growth region. This will enable

enhanced control over the range of core/shell diameter ranges than has been achieved at present. Moreover, the understanding of the particle focusing onto the centerline of the reactor is another important insight for the growth of heterostructured particles as it implies that all particles essentially experience the same growth conditions in the reactor, despite the parabolic flow velocity profile expected for laminar flow reactors.

However, the current study also leaves several open questions, such as whether particle trapping is a universal phenomenon or whether it is dependent on the nanoparticle material. For high gas flow rates most particles may not be trapped because the critical size for particles to be released from the trap by the gas drag decreases. Equally, one may envision electric field configurations in the plasma that do not support trapping. It is also not clear whether nanoparticles of insulators, semiconductors, or metals will be equally trapped as their charge states depend on their capacitance and secondary emission processes, and so depend on the materials work function or dielectric properties. These issues will need to be clarified to fully take advantage of particle trapping in nanoparticle synthesis as a design parameter. However, the current study already demonstrates that gas flows and electric fields can be designed to utilize particle trapping to control particle sizes and size distributions.

Chapter 4: Particle Charge Distributions in the Effluent of a Plasma

4.1 Introduction

It has long been known that dust particles suspended in nonequilibrium plasma become highly negatively charged [44, 47–49]. If an appreciable fraction of that negative charge could be retained after the plasma, then plasma treatments of aerosols could be used as a means of charging for electrostatic manipulation towards technological ends; for example particle removal [50, 51] or supersonic impaction for material deposition applications [147, 148]. Furthermore, if a dependence could be established of the electrostatic charge on the material comprising the dust particles, then material separation processes could be designed. Such electrostatic material separation devices could have wide ranging applications if they could be realized. There is currently a gap in knowledge of the fundamental processes that control the resultant electrostatic charge on dust particles after they have flowed out of a low temperature plasma under continuous operation, and furthermore, the extent to which those processes can be controlled using external parameters such as gas flow velocity. There is also a gap in knowledge of direct experimental measurements of the resultant electrostatic charge on similarly size particles comprised of different materials that have passed through nominally the same plasma.

It is well established how particles become highly negatively charged (on the order of 1 to 10 charges per nm of particle diameter) as a result of electrons having a much higher mobility in the plasma compared to ions [44, 47–49]. More recent attention has been given to particle charging behavior in plasma afterglows. In low pressure plasmas, Minderhout et al [149] showed

that the magnitude of particle charge in a remote plasma (spatial afterglow) is significantly lower than what is expected in the plasma. Chen et al [150–152] found that particles can even become bipolarly charged out of plasma and can aggregate after either low or atmospheric pressure plasmas. At atmospheric pressure, Sharma et al [153] recently demonstrated particles can be bipolarly charged after an AC or RF plasma. Taking these previous results in mind, a clear mechanistic timeline for how particles become charged in the plasma, and decharge after the plasma under technologically relevant conditions for aerosol treatments, has not been forthcoming. One of the aims of this work is to fill that gap.

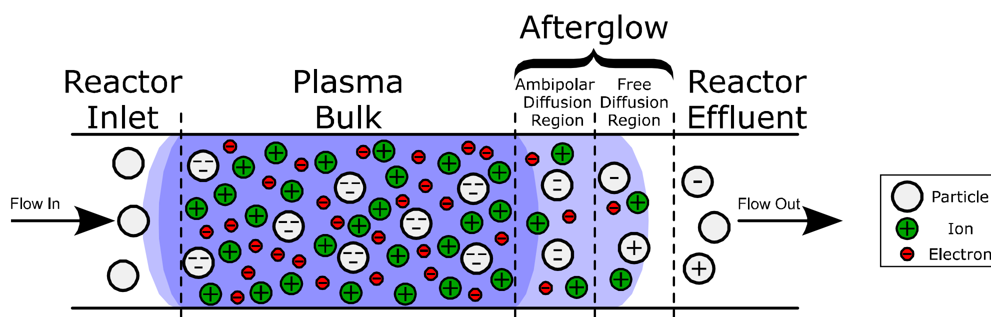

Figure 4.1. A simplistic diagram of particle charging in a plasma. Particles in the plasma bulk are highly negatively charged. In the spatial afterglow, particles will begin to lose negative charges and can become negatively, neutrally, or even positively charged as particles transfer from the ambipolar diffusion to the free diffusion region.

In the afterglow, the weakening of the electric field reduces electron acceleration (causing a reduction in secondary electron emission from gas molecules) and field emission. Thus, the electron temperature and ion/electron densities decrease. As illustrated in Fig. 4.1, due to reduced ion and electron interactions, the ion/electron diffusion mechanism transitions from ambipolar diffusion (ions and electrons diffuse at the same rate) to free diffusion (ions and electrons diffuse at disparate rates). Following this transition, electrons are lost to the tube walls at a higher rate compared to ions due to their greater mobility. Collectively, the reduction in

electron temperature and density suppresses electron-particle collisions and leads to the loss of negative charges, and particles can obtain a bipolar or even net-positive charge distribution downstream from the plasma. Given better control of the afterglow, the charge states of particles leaving a plasma can potentially be varied at will.

Though of great interest, the relationship between particle material and particle charge in a low temperature plasma (LTP) effluent is unclear. Particle work function (a material dependent property) is known to affect thermionic emission (TE), secondary electron emission (SEE), and field emission (FE) [154, 155]. Although separate models are used to describe these three mechanisms [154, 155], decreasing the work function of a particle increases the outgoing electron flux for each case. However, due to ion and electron bombardment, it is unclear what impact TE, SEE, and FE could have on particles in an afterglow.

To better understand the charging mechanisms of particles in an LTP afterglow, charge distributions of monodisperse silica (SiO_2), gold (Au), and hematite (Fe_2O_3) nanoparticles charged via a capacitively coupled plasma (CCP) were measured as a function of particle size and gas flow velocity. Nanoparticle charges were characterized using a differential mobility analyzer (DMA) in conjunction with a condensation particle counter (CPC). Tandem differential mobility analyzers (TDMA) have been used in the past to measure particle charge distributions of polydisperse aerosols [156]. In this work, monodispersed particles were studied, and a mobility inversion procedure was developed to extract particle charge distributions from the measured mobility distributions without the need for a second DMA. Furthermore, a constant number Monte Carlo model [157, 158] was constructed to demonstrate the evolution of particle charge in a spatial afterglow under the transition from ambipolar to free diffusion of energetic species. The simulation incorporates ion-particle collision, electron-particle collision, ion-

electron recombination, electron temperature decay and ion/electron convective loss to the tube walls with a model describing the transition of ambipolar to free diffusion in the spatial afterglow.

4.2 Methods

4.2.1 Experimental Setup & Procedure

Error! Reference source not found. 4.2 shows a schematic of the experimental setup which consists of five main components: a Collison nebulizer, a diffusion dryer, a plasma tube, a DMA, and a CPC. First, nanoparticles were aerosolized using a single-jet Collison nebulizer (CH Technologies Inc.). This nebulizer generates particle containing droplets from a colloidal solution via a high velocity jet stream. The jet stream consisted of argon flowing at 1.5-2.5 SLM depending on the desired plasma gas flow velocity. Based on manufacturer specifications, the nebulizer is estimated to generate 1×10^{11} droplets per mL of solution under the specified flow conditions. 10 mL colloidal solutions were prepared for each type of studied nanoparticle by diluting stock solution/powder with Milli-Q® ultrapure water followed by 5 minutes of sonication to break up agglomerates. The resulting solutions had a particle concentration of 5×10^{10} mL^{-1}. The particle concentration was set lower than the solution droplet concentration such that most droplets are expected to contain 0 or 1 particles. This method prevents particle agglomeration during the drying step.

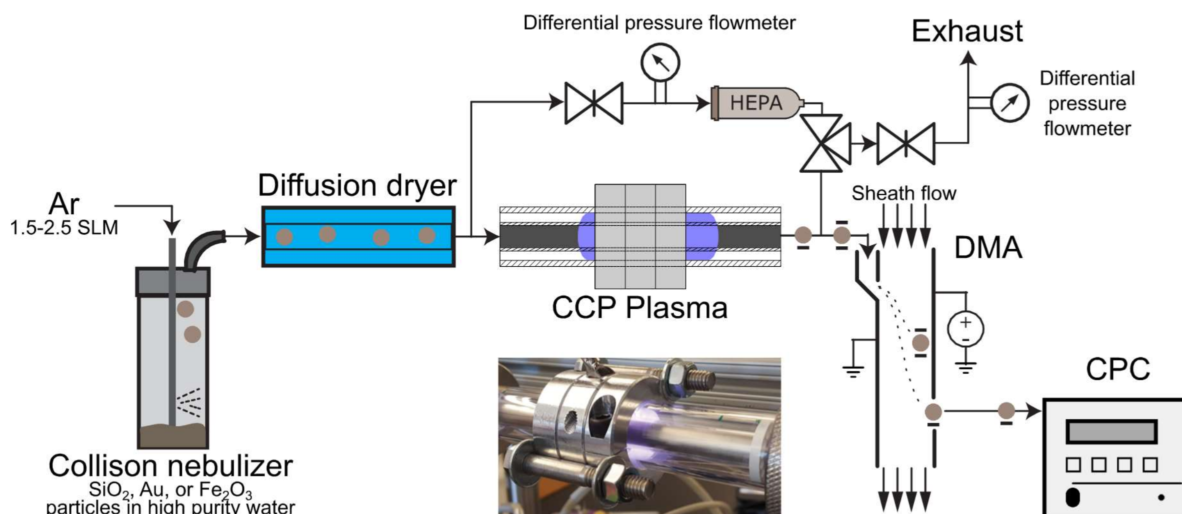

Figure 4.2. Schematic of the experimental setup.

A diffusion dryer containing 13X molecular sieve desiccant (Delta Enterprises Inc.) was used to remove the aerosolized water generated from the nebulizer. An HYT 939 humidity sensor from Innovative Sensor Technology was used to monitor aerosol humidity post-dryer. The desiccant used in this study was shown to reduce water content to less than 1 ppm while traditional silica gel desiccant (Fisher Scientific International, Inc.) only reduces the water content to 630 ppm.

Following the diffusion dryer, the dried aerosol reaches the CCP tube. It is an atmospheric pressure radio frequency (RF) flow-through plasma with a coaxial electrode configuration. The plasma is generated in the annular space between the inner and outer electrode. Fused quartz tubes were utilized as dielectric barriers to electronically isolate the powered outer ring electrode (which has an inner diameter of 25 mm) and grounded inner rod electrode (which has as outer diameter of 9.3 mm) from the plasma. A detailed schematic of the plasma tube is shown in Fig. C.1. A thermocouple located inside of the inner electrode measured

the temperature of the axial center of the plasma tube to be 600 K during operation. The powered outer electrode was supplied 80 W of power by an RF (13.56 MHz) AG0163 power supply with an AIT600 matching network (T&C Power Conversion). An Impedans RF-compensated double Langmuir probe was utilized for plasma characterization. Details on the double Langmuir probe method are described by Malter et al. [159]. For these measurements, the outer plasma tube was replaced with a similar tube with a perpendicular probe port located directly downstream of the outer electrode. The platinum probe tips were 5 mm long and had a radius of 0.18 mm. Although the probe tips were not between the powered and unpowered electrodes, they were well within the plasma glow region. Plasma parameters were extracted from the I-V curve by using the analysis described by Raizer et al. for the highly collisional regime [30]. Langmuir probe results, along with other measured plasma parameters, can be found in Table 1.

Table 4.1. Plasma parameters, T_e, the electron temperature, n_{ion}, the ion density, P, pressure, and T_B, the bulk temperature in the plasma.

T_e (eV)	n_{ion} (#m^{-3})	P (Torr)	T_B (K)
4	10^{18}	745	600

A TSI 3081 DMA was utilized to select plasma charged nanoparticles based on electrical mobility, and the selected particles were counted using a TSI 3010 CPC. Total particle concentration without DMA filtering was measured to be ~10^4 cm^{-3} by the CPC. The DMA characterization zone consists of two coaxial cylindrical electrodes. The outer electrode was grounded and the inner electrode was at an elevated potential, thus creating an electrical field in the radial direction. Sample flow entering the DMA was collectively driven by a sheath flow (sheath flowrate >> sample flowrate) in the axial direction, result in mobility-specific particle trajectories from the balance of Coulombic and drag forces. Only particles within a narrow range

of mobilities will be sampled from the DMA at a given DMA inner electrode voltage. The inner electrode was controlled by a Bertan 225 Series high voltage power supply. By sweeping the DMA voltage, a full mobility spectrum was measured by the CPC. Mobility distributions of both positively and negatively charged particles were characterized by switching the polarity of the DMA power supply. Consequently, the DMA set mobility, Z_p^*, is a function of DMA geometry, applied voltage and flow conditions [160]:

$$Z_p^* = \frac{Q_s + Q_a}{2\pi VL} \ln\left(\frac{r_2}{r_1}\right) \tag{4.1}$$

where Q_s is the sheath flow rate, Q_a is the sample flow rate, V is the set voltage, L is the DMA effective characterization length, and r_1 and r_2 are the inner and outer electrode radii. Furthermore, particle mobility, Z_p, is related to particle size by Stokes' law:

$$Z_p = \frac{qeC_c(d_p)}{3\pi\mu d_p} \tag{4.2}$$

where q is the number of charges on a particle, e is the elementary charge, $C_c(d_p)$ is the Cunningham slip correction factor, μ is the gas viscosity in the DMA (approximated as the sheath gas viscosity), and d_p is particle mobility diameter (the diameter of a singly charged spherical particle with equivalent electrical mobility). The Cunningham slip correction factor is given by [161, 162]:

$$C_c(d_p) = 1 + \frac{2\gamma}{d_p}\left(1.257 + 0.4\exp\left(-\frac{0.55d_p}{\gamma}\right)\right) \tag{4.3}$$

where γ is the mean free path of the gas. Therefore, discrete mobility spectrum is expected to resolve for monodisperse particles of various charge states. Air was used instead of argon for the sheath flow to prevent electrostatic discharging (arcing) in the DMA.

To keep operation conditions constant for the DMA and CPC across all the examined cases, the sample flowrate entering the DMA was set to 1.5 Lpm and the sheath flow was set to 8 Lpm. The flowrate through the plasma tube was independently adjusted using bypass valves as illustrated in Fig 4.2. If the set plasma tube flowrate was less than 1.5 Lpm, the nebulizer flowrate was set at 1.5 Lpm. The excess flow was then diverted prior to the plasma tube, filtered, and then recombined with the plasma tube flow prior to the DMA inlet. If the set plasma tube flowrate was more than 1.5 Lpm, the nebulizer flowrate was set to the desired plasma tube flow rate. Excess flow was vented to an exhaust prior to the DMA inlet. Flowrates through the bypass lines were determined using differential pressure flowmeters. Particle residence time between the plasma and the DMA is estimated to be 3 to 15 s.

Nanoparticles of various sizes and work functions were selected for study based on DMA detection range, monodispersity, and commercial availability: 166 nm silica, 261 nm silica, 507 nm silica (Cospheric LLC), 100 nm gold (nanoComposix Inc.), and ellipsoidal 200×50×50 nm hematite (Corpuscular Inc.). Note that the surface area equivalent diameter of hematite is 90 nm, and the mobility diameter of the hematite nanoparticles was measured to be 110 nm. As shown in Fig. 4.3, all nanoparticles were monodisperse. SEM samples were prepared via drop-casting, and all SEM images were captured using a Thermo Scientific™ Quattro S ESEM. Reported work functions for bulk materials can be found in Fig. 4.3(f).

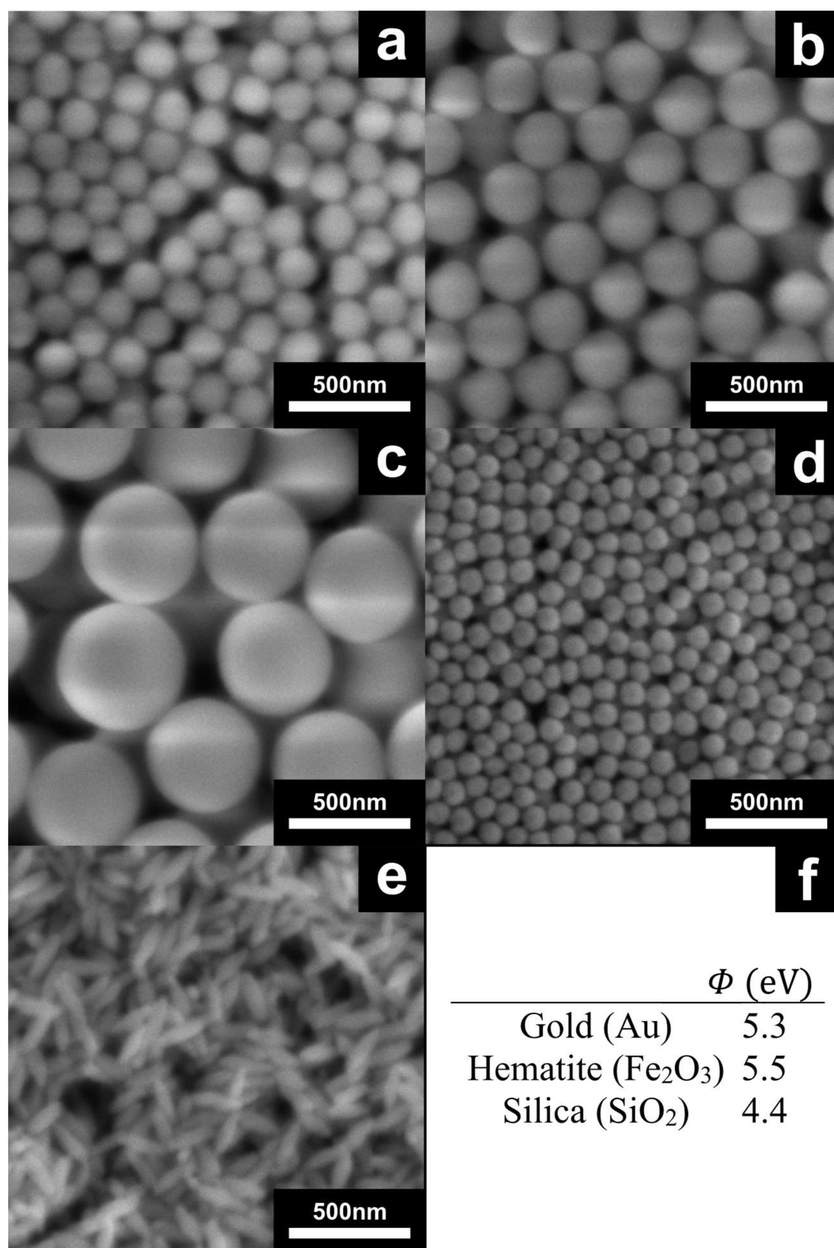

Figure 4.3. SEM images and bulk work functions. (a) 166 nm silica. (b) 261 nm silica. (c) 507 nm silica. (d) 100 nm gold. (e) 90 nm surface area equivalent hematite. (f) bulk material work functions [163–165].

4.2.2 Mobility Inversion Procedure

When the DMA is set to select particles of a certain mobility, it is inevitable that not only particles of the selected mobility can be transferred through the DMA characterization zone, but

also particles of adjacent mobilities, though with lower probability [166]. Thus, particle size distributions from the DMA-CPC measurement usually deviate from actual particle size distributions:

$$N_{Z_p^*} = \sum_{q=-\infty}^{\infty} \phi_q \int_0^{\infty} n(d_p) \Omega_{Z_p^*,q}(d_p) dd_p \quad (4.4)$$

where $N_{Z_p^*}$ is the particle number concentration measured by the CPC when DMA is set to select particles of mobility Z_p^*, ϕ_q is the fraction of particles with charge q. The size dependency of ϕ_q is ignored since particles are monodisperse as suggested by Fig 4.3. $n(d_p)$ is the actual particle size distribution and $\Omega_{Z_p^*,q}(d_p)$ is the DMA transfer function, indicating the fraction of particles with charge q and mobility diameter d_p transmitted through the DMA at the selected mobility Z_p^*.

A full mobility spectrum can be measured from the CPC by sweeping the DMA voltage. The DMA voltage sweep for each polarity is described by Eq. 4.5:

$$V(t) = V_o \left(\frac{V_f}{V_o}\right)^{\frac{t}{\tau}} \quad (4.5)$$

where $V(t)$ is the voltage at time t in kV, V_o is the initial voltage (±0.1 kV), V_f is the final voltage (±10 kV), and τ is the scan time (300s). The voltage is swept in this way in order to simplify the DMA transfer function as described by Wang and Flagan [74].

Traditionally, DMA transfer function accounts for small variances in the streamlines particles must follow to be selected. For instance, the physical width of the inlet and outlet slot of the DMA characterization zone can cause particles of a narrow range of mobilities to be filtered

through the DMA. Moreover, the diffusional effect of nanoparticles can also change the DMA transfer function. However, for particles in the size range (~100 nm) of this study, the diffusional effect can be ignored. To confirm this, both a non-diffusing transfer function and a diffusion transfer function were used to invert the CPC data and the same results were obtained (data not shown). Therefore, for computational ease, the non-diffusive transfer function Ω presented by Stolzenburg and McMurry [166] was utilized in the data inversion procedure:

$$\Omega = \frac{\left(\left|\tilde{Z}_p - (1+\beta)\right| + \left|\tilde{Z}_p - (1-\beta)\right| - \left|\tilde{Z}_p - (1+\beta\delta)\right| - \left|\tilde{Z}_p - (1-\beta\delta)\right|\right)}{2\beta(1-\delta)} \quad (4.6)$$

where $\tilde{Z}_p = \frac{Z_p}{Z_p^*}$, with $\beta = \frac{Q_b + Q_a}{Q_m + Q_s}$, with Q_b being the selected aerosol (outlet) flowrate, Q_m being the excess outlet flowrate, and $\delta = \frac{Q_s - Q_a}{Q_s + Q_a}$.

To accurately extract charge distributions from the mobility distribution, mobility inversion must be performed. Traditional mobility inversion procedure solves for a particle size distribution given a known charge distribution (by the use of a neutralizer) [160]; however, in this paper, a normal particle size distribution is assumed (as the studied particles are monodisperse), and the particle charge distribution is solved. The assumed particle size distribution is:

$$n(d_p) = \frac{N}{\sigma\sqrt{2\pi}} \exp\left(-0.5\left(\frac{d_p - \bar{d}_p}{\sigma}\right)^2\right) \quad (4.7)$$

where N is particle total concentration, σ is the standard deviation of the particle size, and $\bar{d}_p$ is the mean particle diameter. In addition, the charge fraction of neutral particles cannot be measured by the DMA-CPC system, so the condition $\sum_{q=-\infty}^{\infty} \phi_q = 1$ cannot be utilized.

Therefore, relative charge fractions are solved with $\sum_{q=-\infty}^{\infty} \phi'_q = \beta$ and $\phi'_{-1} = 1$. Combining the above discussion, Eq. 4.4 becomes:

$$N_{Z_p^*} = \sum_{q=-\infty}^{\infty} \phi'_q \int_0^{\infty} \frac{\alpha}{\sigma\sqrt{2\pi}} \exp\left(-0.5\left(\frac{d_p - \bar{d}_p}{\sigma}\right)^2\right) \Omega_{Z_p^*,q}(d_p) dd_p \tag{4.8}$$

where $\alpha = N/\beta$. Parameters α, σ, $\bar{d}_p$ and ϕ'_qs are solved with the MATLAB nonlinear least-squares solver. As discussed in the results section, the particle neutral charge fraction and real charge fractions ϕ_q can be inferred by fitting the charge distribution to a shifted Boltzmann charge distribution.

4.2.3 Numerical Modelling Method

To model the particle charge dynamics in and out of the plasma, a simplified model of the constant number Monte Carlo (CNMC) simulation for the plasma and spatial afterglow developed by Chen et al [158] was implemented. The simulation is composed of two parts: (a) simulation of particle charging in-plasma (the region where discharge glow is observed)) and (b) simulation of particle charging post-plasma (from the end of discharge glow to the inlet of the DMA). In both simulations, particle charge is dynamically modeled due to the competition of ion-particle and electron-particle collisions [96, 167–171]. Collisional growth and convective loss of particles are ignored due to the low particle total concentration in this study. Measured plasma conditions shown in Table 1 are utilized for in-plasma simulation. The plasma conditions and the particle charge distribution at the end of in-plasma simulation served as the input of the post-plasma simulation, and the post-plasma gas temperature is changed to 300 K. In the plasma, electron density is calculated using the quasi-neutral condition assuming constant ion density

[172]. In the post plasma, both ion and electron densities reduce due to ion-electron recombination, collisional losses to particles, and diffusive losses to the wall [173, 174]. The electron temperature also starts to decay post plasma [175, 176]. In the CNMC simulation, the change of ion, electron, and particle status is modeled as a function of the residence time in the system. In a flow-through set up as in the experiment, plasma species and particles are assumed to follow the fluid flow. As such, the residence time in the simulation can be interpreted as a spatial distribution along the fluid path at a given fluid velocity. The details of the simulation model are described in Appendix C.

In the plasma, ions and electrons follow ambipolar diffusion because of the high potential between species of opposite charges. Ions and electrons will eventually exhibit free diffusion as they leave the bulk plasma environment, and their densities will fall. However, there lacks a specific mathematical expression to describe how and when the transition from ambipolar to free diffusion happens for plasmas with dusty particles. Chen et al [158] separately studied the effects of free diffusion and ambipolar diffusion on particle charging in a spatial afterglow using the CNMC model and demonstrated that a transition diffusion model would be more accurate. Studies have shown that the transition diffusion is a function of the ratio of the system diffusive length Λ to the electron Debye length λ_D [177]. As illustrated in the results section, in this study a transition from ambipolar diffusion to free diffusion is arbitrarily chose to occur when Λ/λ_D=7.

4.3 Results and Discussion

4.3.1 Particle Charge Distributions from the Mobility Inversion Procedure

To confirm that particles are charged through the CCP plasma, mobility distributions of 261 nm silica nanoparticles with and without a plasma exposure were compared as shown in Fig. 4.4(a). When the plasma was off, there appeared to be a small concentration of highly charged particles (on the order of 100 #cm^{-3}). However, the majority of particles were neutral without plasma exposure. When the plasma was turned on, discrete peaks for particles of different charge states were observed in the mobility spectra. Note that the concentration of charged particles is roughly proportional to the area under the curve. Interestingly, positively charged particles were observed even though these particles are expected to be highly negatively charged in plasma.

To calculate the particle charge distribution more accurately, particle size distributions and relative charge fractions were solved as described in the methods section. A comparison of the measured mobility distributions and fitted mobility distributions from the inversion procedure for 261 nm silica nanoparticles at various gas flow velocities are shown in Fig. 4.4(b). The assumption of a normal particle size distribution appears to yield calculated mobility spectra with close fit to the CPC data. $\bar{d}_p$ and σ were varied independently for each fit, and the determined values were shown to be consistent under the different flow conditions ($\bar{d}_p$ = 272 ± 3 nm and σ = 35.6 ± 3.0 nm). Calculated $\bar{d}_p$ was close to the expected value of 261 nm, however, σ was higher than expected. The standard deviation of particle size from SEM results was determined to be 16.7 nm and mean particle size as determined by SEM was 251 nm (note that

manual measurement error and instrumental error can account for the slight size discrepancy). Fig 4.4(c) shows the comparison of the particle size distribution for 261 nm silicon nanoparticles as determined by the inversion procedure and SEM imaging. There appears to be artificial broadening in the inverted size distribution that the DMA transfer function does not sufficiently account for. It should be noted that the 3010 CPC has been reported to artificially broaden size distributions due to having a long flushing time [178]; however, this effect is expected to cause the observed mobility spectra to have asymmetrical peaks (peaks that tail off on one end), which is not observed in the measured result. A study could be performed to better describe the transfer function of this system. Nevertheless, the procedure described above is sufficient in calculating relative particle charge distributions ϕ_q' as the inverted particle size distribution of same particle sample was consistent across different experimental conditions. If the instrumental defects from the DMA-CPC system are properly removed in the inversion procedure, the inverted particle size distribution is expected to agree with SEM images and ϕ_q' would remain unaltered.

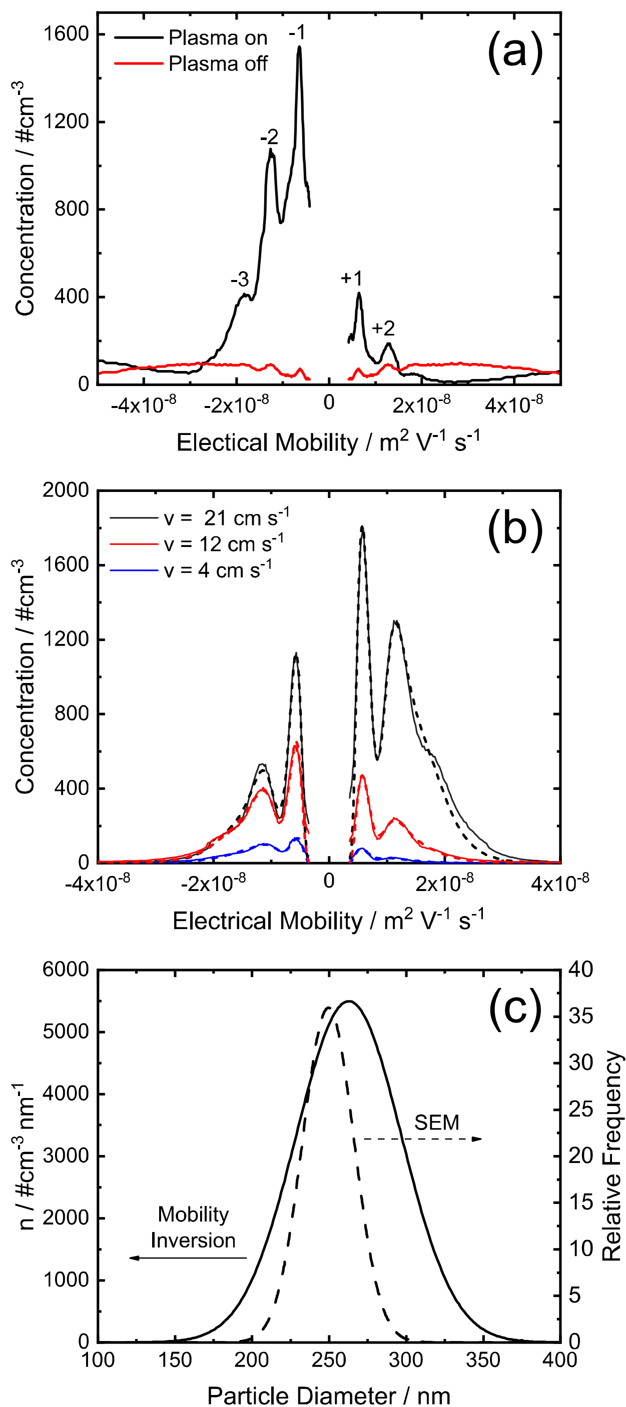

Figure 4.4. Sample results from the mobility measurements. (a) Particle mobility spectra measured with the plasma on and off. (b) A comparison of the mobility data from the CPC (solid) to the fitted mobility spectrum generated from the mobility inversion procedure (dotted) for 261 nm silica as a function of gas flow velocity. (c) The particle size distributions resulting from the inversion procedure and SEM imaging.

Aerosol particles in thermal equilibrium with bipolar ions are known to follow a Boltzmann law governed bipolar charge distribution (net-neutral) as a result of the thermal motions between ions and particles [179]. Here, we found that the inverted particle charge distribution after a flow-through plasma can be fitted to a shifted version of this bipolar charge distribution (referred to as shifted Boltzmann charge distribution) in a wide range of particle sizes and flow velocities:

$$\phi_q = \frac{1}{(2\pi\kappa^2)^{\frac{1}{2}}} \exp\left(-\frac{(q-\bar{q})^2}{2\kappa^2}\right) \tag{4.9}$$

where $\kappa = \left(\frac{1}{2} d_p kT\right)^{\frac{1}{2}}/e$, k is the Boltzmann constant and T is the bulk gas temperature. $\bar{q}$ was solved using a sum of least-squares error minimization between the relative charge fraction results and Eq. 4.9. As mentioned in the methods section, the mobility inversion procedure can only predict relative charge fraction ϕ_q' as the neutral fraction is unknown; however, since the relative charge fractions follow a Gaussian distribution and the sum of real charge fractions ϕ_q is unity, all charge fractions (including the neutral fraction) can be estimated. The fitted particle charge distributions agree very well with the shifted Boltzmann charge distribution model illustrated in Fig. 4.5. To verify that the neutral fraction is being accurately described, we measured the neutral fraction using an electrostatic precipitator, which removes all charged particles, and a CPC. The shifted Boltzmann distribution was shown to accurately capture the neutral fraction, and the results can be found in Appendix C. As described by Eq. 4.9, the fitted particle charge distribution is wider with larger particles (see Fig. 4.5(a)) as κ is proportional to the square root of particle diameter. For 507 nm silica particles, the charge fractions were determined based on ≥ 3 charge states of both polarities as the lower charge states are outside of

the DMA mobility detection range. At the same particle size, the fitted charge distribution is observed to shift with flow velocity without change of the distribution shape (same κ). Thus, in the following section we utilized the net charge $\bar{q}$ from Eq. 4.9 to compare the particle charge distribution at different experimental conditions.

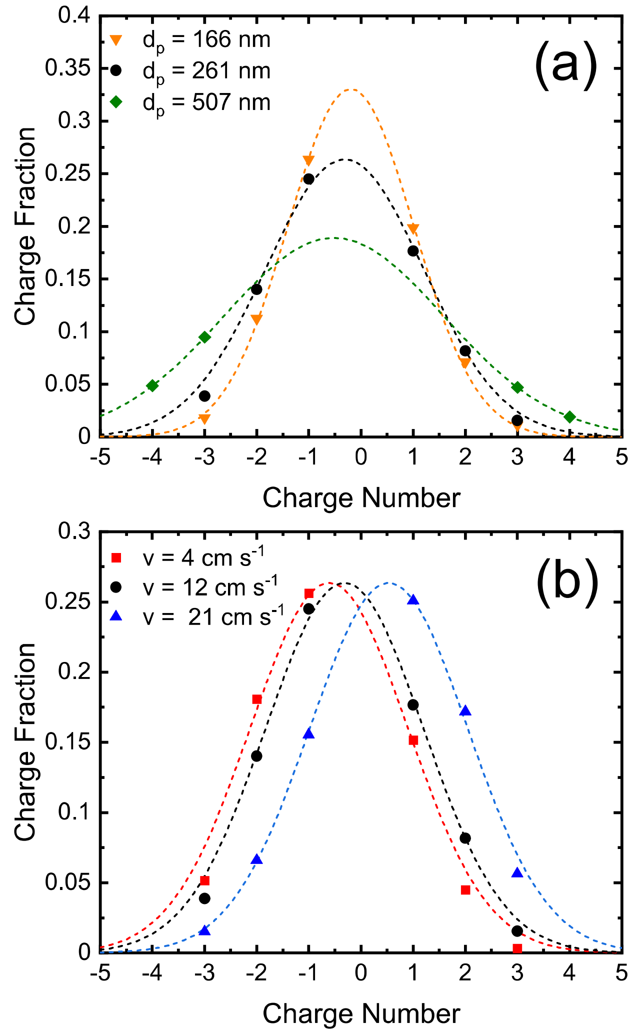

Figure 4.5. Experimentally determined particle charge fractions fitted to shifted Boltzmann charge distributions. Particle charge fractions (markers) were fitted to Eq. 4.9 (dashed) (a) for silica of various diameters at a gas flow velocity of 12 cm s^{-1}; (b) for 261 nm silica at various gas flow velocities.

4.3.2 Influential Parameters on Particle Charge

The average charge was determined for various particle materials, sizes, and the gas flow velocities as shown in Fig. 4.6. As seen in Fig. 4.6(a), particle charge states appear to be independent of particle material. Since the decrease of work function is associated with higher electron emission due to TE, SEE, and FE, particles with a lower work function are expected to be more positively charged; however, the results suggest that these mechanisms are insignificant at these temperatures compared to electron/ion bombardment. A difference in charge states between SiO_2, Au, and Fe_2O_3 particles is observed at low flow velocities; however, particles become more positively charged as work function is increased. As such, a change in work function does not explain the results shown in Fig. 4.6(a). Since increasing particle temperature and lowering particle work function is known to increase the electron emission rate, material dependent charging is more likely to occur under those conditions [154, 155].

The effect of particle size on mean particle charge is observed in Fig. 4.6(b). At low flow velocities, particles in all studied cases were net-negatively charged, and the largest particles had the most negative charges. Similarly, at high flow velocities, particles were net-positively charged, and the largest particles had the most positive charges. This result also coincides with the small variations of mean charge in Fig. 4.6(a) - the silica nanoparticle is the largest and thus has the most negative charges at low flow velocities. It is intuitive to predict that larger particles are less positively charged leaving the plasma volume as they are more negatively charged in the plasma. In fact, a contradictory phenomenon is observed from the experiment. Therefore, it is

necessary to study how the plasma parameters change in the spatial afterglow and how these parameters affect the charging dynamics of dust particles.

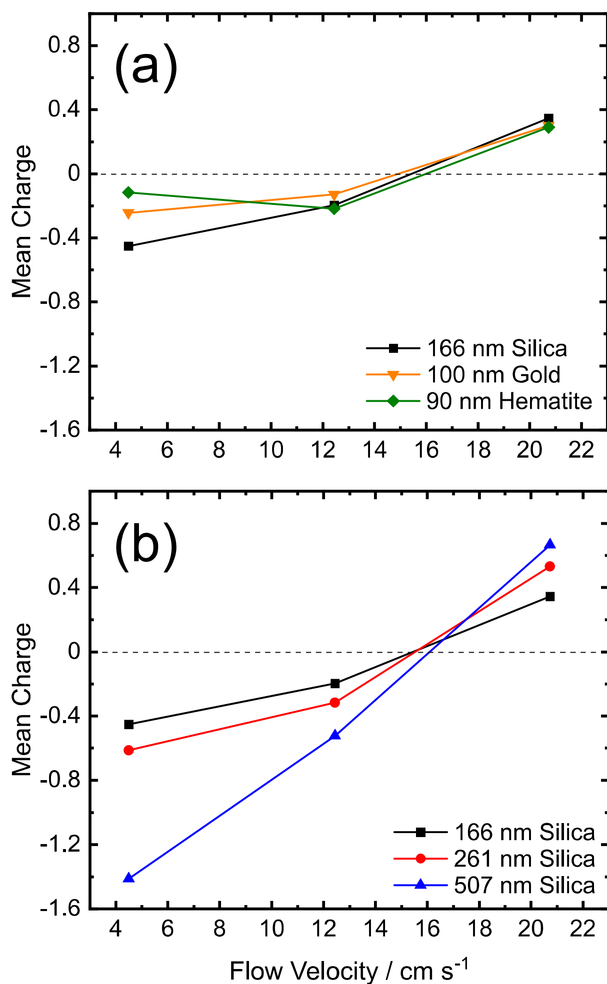

Figure 4.6. Experimentally determined mean charges in the plasma effluent as a function of flow velocity, (a) particle material, and (b) particle size.

A most interesting result shown in Fig. 4.6 is the effect of flow velocity on particle charge. As the flow velocity increases, the particles go from being net-negatively charged to net-positively charged. If the change in flow velocity only affects particle velocity, and not plasma parameters, one would expect that an increase in flow velocity would cause particles to be more negatively charged (as they would have a lower residence time in the afterglow). Since the

opposite result is observed, changing the gas flow velocity appears to directly affect plasma parameters in the plasma and afterglow. Nevertheless, the existence of net-positively charged particles in the plasma effluent is particularly interesting as particles are known to be highly negatively charged in the plasma bulk. To better understand how particles reach this charge state, a constant number Monte Carlo model [157] was constructed and computer experiments were performed.

4.3.3 Numerical Modelling Results

To compare with experimental results, the charging behavior of 166 nm, 261 nm and 507 nm SiO_2 nanoparticles in and after the plasma was simulated as shown in Fig. 4.7. Fig. 4.7(a) illustrates that nanoparticles, initially neutral, become negatively charged in the plasma, and larger particles are more negatively charged. When the particle charge state develops such that the ion-particle collision equilibrates with electron-particle collision, the average particle charge reaches a steady state in the plasma. From Fig. 4.7(a) the average charge does not change with time after a microsecond for all simulated particle diameters. This is orders of magnitudes below the time scale particles spend in the plasma region for the experiment (approximately 5 seconds) which suggests that particles reach their equilibrium negative charge state in the plasma for all experimental conditions.

Particles can become neutral and even positively charged in the post plasma, as exhibited in Fig. 4.7(b-c), due to the decrease of electron temperature and the differences in ion and electron loss rates illustrated in Fig. 4.7(d). In Fig. 4.7(b), particles become more negatively charged around 10^{-3} ms post plasma compared to their charge state in plasma. This is because the ion temperature drops from 600 K to 300 K in the post-plasma simulation. Thus, for a short

period of time ion-particle collision reduces, and particles become more negatively charged. However, particles soon lose negative charges because the electron temperature decreases, and electron-particle collisions are suppressed. The decrease in electron temperature will reduce the number of negative charges on particles. Together with changes in ion and electron densities, particles can eventually reach a neutral and even positive charge state.

When ions and electrons transition from ambipolar to free diffusion, the electron density decreases faster than the ion density, and an ion-rich environment is created post plasma. This ion-rich environment is what drives the reversal of particle charge state after the plasma. How fast the effective diffusion coefficient changes from ambipolar to free diffusion model will affect how quickly particles lose electrons and the eventual particle charge states post plasma. In the simulation, we chose for free diffusion to occur when Λ/λ_D<7 for all cases. The number 7 was chosen so that the net charge on the particles is around neutral when the particle residence time post plasma is close to that of the experiment (3 to 15 s). Further studies are needed for a more accurate transition diffusion model of the plasma species in the spatial afterglow.

Furthermore, Fig. 4.7(c) shows that the large particles, although more negatively charged in plasma, are more positively charged post plasma. This is in agreement with the experimental findings in Fig. 4.6. The reason that larger particles are more positively charged post plasma follows the reason that particles are more negatively charged in the plasma – larger particles have increased chances to collide with ions or electrons and thus they will have more charges, negative or positive. The simulated particle charge distribution largely follows the shifted Boltzmann charge distribution (Eq. 4.9) around the net-neutral state with a few discrepancies as shown in Fig. 4.7(e). While the simulation results in Fig. 4.7 are based on the experimentally measured plasma conditions in Table 1, we noted that the electron temperature and ion density

measured from the experiment deviate from conventional values for atmospheric pressure plasmas. For this reason, sample simulations were performed using more conventional plasma conditions as shown in Appendix C. The results are consistent with Fig. 4.7.

The simulation suggests that particles are more positively charged at longer residence times. This opposes the experimental results that particles are more negatively charged at low flow velocities, which correspond to longer residence times. We note that although the residence time in the simulation can be converted to space distribution along the plasma tube at a given plasma condition (and thus flow velocity), the simulation is not able to predict the effect of flow velocity on the particle charge in the plasma effluent. It is unclear how the flow velocity affects the post plasma volume and the plasma conditions. The plasma volume was observed to increase with flow velocities in the experiments. Although the plasma parameters listed in Table 1 were not sensitive to flow velocities in the Langmuir probe measurement, several studies on atmospheric plasma jet have observed that flow velocity can affect plasma geometry and plasma parameters in the plasma bulk [180–182]. As illustrated by Fig. 4.7 and Fig. C.4, when plasma parameters are changed, simulated particle charge distributions differ given a constant residence time. Moreover, it can be inferred that flow velocity may also affect the rate of electron temperature decay, ion and electron convective loss rate as well as other parameters in the plasma afterglow. Further studies are needed to reveal the effect of flow velocity on plasma parameters in and out of plasma to understand why particles become positively charged at high flow velocities. Nevertheless, the simulation can be improved to reflect the effect of flow velocity if plasma parameters in plasma and afterglow can be calculated accordingly.

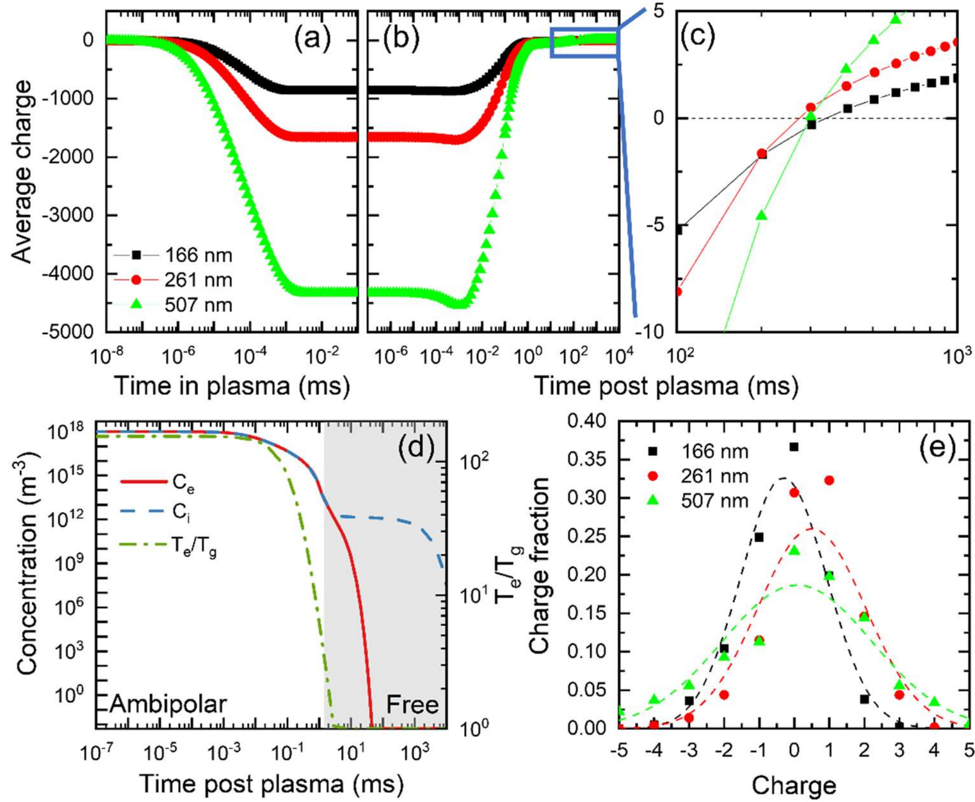

Figure 4.7. Simulation results. (a-c) Average particle charge for various particle diameters as a function of (a) particle residence time in plasma (b-c) particle residence time post plasma. (d) Electron density (C_e), ion density (C_i) and ratio of electron temperature (T_e) to gas temperature (T_g) as a function of residence time post plasma for 166 nm SiO_2 nanoparticles. The shaded area is when free diffusion starts. (e) Charge distributions of 166 nm, 261 nm, and 507 nm SiO_2 nanoparticles at a selected residence time post plasma of 303 ms (markers) with comparison to charge distributions from Eq. 4.9 (lines).

4.4 Conclusions

Utilizing combined DMA-CPC measurement and CNMC simulation, we demonstrated that particles could become negatively, neutrally, or even positively charged in an AP-LTP afterglow. A novel mobility inversion method was performed to extract the particle charge distributions from DMA-CPC mobility spectra. Particles were shown to have a shifted Boltzmann charge distribution under all studied conditions and particle net charges are strongly

influenced by the flow velocity and particle size. At low flow velocities, particles became net-negatively charged; however, at higher flow velocities, particles became net-positively charged. Larger particles were shown to have a greater magnitude of charge under all gas flow conditions. Additionally, material-dependent charging effects appeared to be negligible in the studied cases. The CNMC simulation suggested that the difference in the diffusive loss rate of ions and electrons in the spatial afterglow created an ion-rich environment that caused the particle charge to become less negative and even positive post plasma.

Chapter 5: Concluding Remarks

This section summarizes the key findings, developments, and outlook for work shown previously. For a more detailed summaries of each chapter, refer to the individual chapters.

5.1 Summary of Key Findings and Developments

To characterize particle formation, a specialized QCM impactor was developed to measure particle mass density. It was shown to be capable of sampling aerosolized particles with sizes below 10 nm, and by depositing particles on the center of a QCM crystal, rather than over the entire area, device sensitivity could be increased by over an order of magnitude. This methodology allows for the detection of dilute particles (low mass density) at a relatively low cost.

This developed QCM impactor was used to demonstrate how particle formation could be greatly promoted by increasing the reactor tube diameter, or greatly suppressed by reducing the reactor tube diameter. Additionally, increasing pressure was also shown to promote particle formation. The experimental findings supported by modeling results. These results suggest the diffusion of reactive species to surfaces such as the reactor walls plays a major role in determining the respective amounts of film and particle formation (which is an important consideration to prevent reactor fouling, to prevent particle defects for microelectronics production, and to increase yields for nanoparticle synthesis processes).

Once particles have formed, the developed QCM impactor was used to verify particle trapping of sub-10 nm particles in a nonthermal plasma. This finding is significant as it helps

explain the size-focusing behavior of plasma reactors, and it suggests the gas flow velocity should be a critical processing parameter to consider rather than gas residence time. These design considerations can be used to provide better control over the size of synthesized particles and are particularly useful for the synthesis of core-shell nanoparticles.

Once particles leave a plasma, they reach a charge state which is different compared to the particle charge state within a plasma. By utilizing DMA-CPC measurements, particles were shown to become negatively, neutrally, or even positively charged in an AP-LTP afterglow. A novel mobility inversion method was performed to extract the particle charge distributions from DMA-CPC mobility spectra. Particles were shown to have a shifted Boltzmann charge distribution under all studied conditions and particle net charges are strongly influenced by the flow velocity and particle size. At low flow velocities, particles became net-negatively charged; however, at higher flow velocities, particles became net-positively charged.

5.2 Outlook

This work shows a multitude of significant findings made related to the formation, trapping, and charging of particles produced in nonthermal plasmas, and there is much more to be learned. As demonstrated in Chapter 2, the formation of particles vs. film can be greatly controlled by varying system parameters such as reactor diameter, pressure, and chemical composition. Going forward, this new understanding of particle formation behavior in nonthermal plasmas will continue to improve, and this improved understanding will inform synthesis procedures to increase particle yields and prevent reactor fouling. Additionally, it will inform novel system designs for the production of microelectronics.

The work in Chapter 2 and Chapter 3 relied on the development of a high sensitivity QCM impactor. Further development of the QCM impactor may allow for the sampling of nanoparticles at even lower pressures and lower particle mass concentrations (which would be particularly useful for the microelectronics industry). For instance, the QCM crystal are not currently designed for point deposition, and if they were, QCM sensitivity could be greatly improved. Additionally, modifications of the QCM impactor could be made to help prevent diffusional losses from the sampling stream.

As discussed in Chapter 3, acknowledging the trapping phenomenon that particles experience in nonthermal plasmas unlocks a new way of considering particle synthesis methodology. Already this knowledge has been used to better control particle size and particle size distributions [183–185]. As optoelectronic characteristics of nanoparticles are strongly tied to particle size, this capability is of great importance for applications in renewable energy for instance.

As shown in Chapter 4, nonthermal plasmas are clearly capable of modulating particle charge. As such, there is promise to use nonthermal plasmas as high efficiency charge neutralization devices for instrumentation, or to develop an electrostatic precipitator capable of capturing sub-10 nm particles (which is useful to improve air quality and reduce industrial emissions). There has been some effort to achieve these aims [186, 187], and the greatest the difficulty is the charging of ultrafine particles at atmospheric pressure. It should also be noted that the charge reversal (particles going from negatively charged to positively charged) shown in Chapter 5 has also been observed at low pressure conditions [188], which shows great promise for the development of a particle removal device specialized for microelectronic fabrication equipment. To conclude, considerations of particle formation, trapping, and effluent charging

behavior of particles in nonthermal plasmas show great promise for the development of numerous applications such as microelectronics, novel nanomaterials, and aerosol capture devices.

References

1. Alexandrov AF, Bogdankevich LS, Rukhadze AA (1984) Principles of plasma electrodynamics. Springer

2. Boulos MI, Fauchais P, Pfender E (1994) The plasma state. In: Thermal plasmas. Springer, pp 1–47

3. Coburn JW, Winters HF (1979) Plasma etching—A discussion of mechanisms. Journal of Vacuum Science and Technology 16:391–403. https://doi.org/10.1116/1.569958

4. Coburn JW (1982) Plasma-assisted etching. Plasma Chem Plasma Process 2:1–41. https://doi.org/10.1007/BF00566856

5. Coburn JW (1994) Surface-science aspects of plasma-assisted etching. Appl Phys A 59:451–458. https://doi.org/10.1007/BF00348262

6. Einhaus R, Kraiem J, Cocco F, et al (2006) PHOTOSIL – Simplified Production of Solar Silicon from Metallurgical Silicon

7. Chigondo F (2018) From Metallurgical-Grade to Solar-Grade Silicon: An Overview. Silicon 10:789–798. https://doi.org/10.1007/s12633-016-9532-7

8. Tawada Y, Yamagishi H, Yamamoto K (2003) Mass productions of thin film silicon PV modules. Solar Energy Materials and Solar Cells 78:647–662. https://doi.org/10.1016/S0927-0248(02)00456-7

9. Aberle AG (2009) Thin-film solar cells. Thin Solid Films 517:4706–4710. https://doi.org/10.1016/j.tsf.2009.03.056

10. Vetter J (2015) Surface Treatments for Automotive Applications. In: Cha SC, Erdemir A (eds) Coating Technology for Vehicle Applications. Springer International Publishing, Cham, pp 91–132

11. Lampe Th, Eisenberg S, Rodríguez Cabeo E (2003) Plasma surface engineering in the automotive industry—trends and future prospectives. Surface and Coatings Technology 174–175:1–7. https://doi.org/10.1016/S0257-8972(03)00473-0

12. Dakin JT (1991) Nonequilibrium lighting plasmas. IEEE Transactions on Plasma Science 19:991–1002. https://doi.org/10.1109/27.125026

13. Weber LF (2006) History of the plasma display panel. IEEE Transactions on Plasma Science 34:268–278. https://doi.org/10.1109/TPS.2006.872440

14. Sahoo A, Tripathy S (2021) Development in plasma arc welding process: A review. Materials Today: Proceedings 41:363–368. https://doi.org/10.1016/j.matpr.2020.09.562

15. Ammann AA (2007) Inductively coupled plasma mass spectrometry (ICP MS): a versatile tool. Journal of Mass Spectrometry 42:419–427. https://doi.org/10.1002/jms.1206

16. Thomas R (2013) Practical Guide to ICP-MS: A Tutorial for Beginners, Third Edition. CRC Press

17. Holste K, Dietz P, Scharmann S, et al (2020) Ion thrusters for electric propulsion: Scientific issues developing a niche technology into a game changer. Review of Scientific Instruments 91:061101. https://doi.org/10.1063/5.0010134

18. A review of studies on ion thruster beam and charge-exchange plasmas | International Electric Propulsion Conference. https://arc.aiaa.org/doi/abs/10.2514/6.1982-1944. Accessed 14 Mar 2023

19. Mukhovatov VS, Shafranov VD (1971) Plasma equilibrium in a Tokamak. Nucl Fusion 11:605. https://doi.org/10.1088/0029-5515/11/6/005

20. Pitts RA, Carpentier S, Escourbiac F, et al (2011) Physics basis and design of the ITER plasma-facing components. Journal of Nuclear Materials 415:S957–S964. https://doi.org/10.1016/j.jnucmat.2011.01.114

21. Bekeschus S, von Woedtke T, Emmert S, Schmidt A (2021) Medical gas plasma-stimulated wound healing: Evidence and mechanisms. Redox Biology 46:102116. https://doi.org/10.1016/j.redox.2021.102116

22. Nastuta AV, Topala I, Grigoras C, et al (2011) Stimulation of wound healing by helium atmospheric pressure plasma treatment. J Phys D: Appl Phys 44:105204. https://doi.org/10.1088/0022-3727/44/10/105204

23. Bekeschus S, Schmidt A, Weltmann K-D, von Woedtke T (2016) The plasma jet kINPen – A powerful tool for wound healing. Clinical Plasma Medicine 4:19–28. https://doi.org/10.1016/j.cpme.2016.01.001

24. (2022) Where on Earth can you find perpetual lightning? In: Yourweather.co.uk | Meteored. https://www.yourweather.co.uk/news/science/where-earth-perpetual-lightning-catatumbo-venezuela.html. Accessed 13 Mar 2023

25. Aurora Borealis Photos. https://www.pexels.com/search/aurora%20borealis/. Accessed 13 Mar 2023

26. “Cosmic Cliffs” in the Carina Nebula (NIRCam Image). In: WebbTelescope.org. https://webbtelescope.org/contents/media/images/2022/031/01G77PKB8NKR7S8Z6HBXMYATGJ. Accessed 13 Mar 2023

27. Weldscientist (2020) Shielded Metal Arc Welding. https://commons.wikimedia.org/wiki/File:Shielded_Metal_Arc_Welding.jpg. Accessed 13 Mar 2023

28. NASA (2016) Ion Propulsion…What Is It? In: Tumblr. https://nasa.tumblr.com/post/138684974869/ion-propulsionwhat-is-it. Accessed 13 Mar 2023

29. JET Achieves Fusion Record. In: ITER. http://www.iter.org/album/media/1 - back in time. Accessed 13 Mar 2023

30. Raizer Y, Allen J Gas discharge physics

31. Fridman A (2008) Plasma Chemistry. Cambridge University Press

32. Kortshagen UR, Sankaran RMM, Pereira RN, et al (2016) Nonthermal Plasma Synthesis of Nanocrystals: Fundamental Principles, Materials, and Applications. Chemical Reviews 116:11061–11127. https://doi.org/10.1021/acs.chemrev.6b00039

33. Ku G, Zhou M, Song S, et al (2012) Copper Sulfide Nanoparticles As a New Class of Photoacoustic Contrast Agent for Deep Tissue Imaging at 1064 nm. ACS Nano 6:7489–7496. https://doi.org/10.1021/nn302782y

34. Meseth M, Kunert BC, Bitzer L, et al (2013) Excimer laser doping using highly doped silicon nanoparticles. physica status solidi (a) 210:2456–2462. https://doi.org/10.1002/pssa.201329012

35. Adjallah Y, Anderson C, Kortshagen U, Kakalios J (2010) Structural and electronic properties of dual plasma codeposited mixed-phase amorphous/nanocrystalline thin films. Journal of Applied Physics 107:043704. https://doi.org/10.1063/1.3285416

36. Herrling MP, Rychen P (2017) Review of nanoparticles in ultrapure water: definitions and current metrologies for detection and control. Ultrapure Micro 1:34–43

37. Uner NB, Thimsen E (2020) Nonequilibrium plasma aerotaxy of size controlled GaN nanocrystals. Journal of Physics D: Applied Physics 53:. https://doi.org/10.1088/1361-6463/ab59e6

38. Uner NB, Thimsen E (2020) Phase mixing in GaSb nanocrystals synthesized by nonequilibrium plasma aerotaxy. Plasma Processes and Polymers 17:1900233. https://doi.org/10.1002/ppap.201900233

39. Moriya T, Nakayama H, Nagaike H, et al (2005) Particle reduction and control in plasma etching equipment. IEEE Transactions on Semiconductor Manufacturing 18:477–486. https://doi.org/10.1109/TSM.2005.858464

40. Vollath D (2007) Plasma Synthesis of Nanoparticles. KONA Powder and Particle Journal 25:39–55. https://doi.org/10.14356/kona.2007007

41. Dijk J van, Kroesen GMW, Bogaerts A (2009) Plasma modelling and numerical simulation. J Phys D: Appl Phys 42:190301. https://doi.org/10.1088/0022-3727/42/19/190301

42. Thimsen E (2018) Beyond equilibrium thermodynamics in the low temperature plasma processor. Journal of Vacuum Science & Technology B 36:048501. https://doi.org/10.1116/1.5022470

43. Thimsen E (2021) Entropy production and chemical reactions in nonequilibrium plasma. AIChE Journal 67:e17291. https://doi.org/10.1002/aic.17291

44. Bouchoule A (1999) Dusty plasmas: physics, chemistry, and technological impacts in plasma processing. Wiley, Chichester ; New York

45. Gresback R, Holman Z, Kortshagen U (2007) Nonthermal plasma synthesis of size-controlled, monodisperse, freestanding germanium nanocrystals. Applied Physics Letters 91:093119. https://doi.org/10.1063/1.2778356

46. You KH, Kim JH, You SJ, et al (2018) Gallium nitride nanoparticle synthesis using nonthermal plasma with gallium vapor. Current Applied Physics 18:1553–1557. https://doi.org/10.1016/j.cap.2018.10.001

47. Goree J (1994) Charging of particles in a plasma. Plasma Sources Sci Technol 3:400–406. https://doi.org/10.1088/0963-0252/3/3/025

48. Khrapak SA, Ratynskaia SV, Zobnin AV, et al (2005) Particle charge in the bulk of gas discharges. Phys Rev E 72:016406. https://doi.org/10.1103/PhysRevE.72.016406

49. Matsoukas T, Russell M (1995) Particle charging in low-pressure plasmas. Journal of Applied Physics 77:4285–4292. https://doi.org/10.1063/1.359451

50. Mizuno A (2000) Electrostatic precipitation. IEEE Transactions on Dielectrics and Electrical Insulation 7:615–624. https://doi.org/10.1109/94.879357

51. Jaworek A, Krupa A, Czech T (2007) Modern electrostatic devices and methods for exhaust gas cleaning: A brief review. Journal of Electrostatics 65:133–155. https://doi.org/10.1016/j.elstat.2006.07.012

52. Bouchoule A, Plain A, Boufendi L, et al (1991) Particle generation and behavior in a silane-argon low-pressure discharge under continuous or pulsed radio-frequency excitation. Journal of Applied Physics 70:1991–2000. https://doi.org/10.1063/1.349484

53. Nijhawan S, McMurry PH, Swihart MT, et al (2003) An experimental and numerical study of particle nucleation and growth during low-pressure thermal decomposition of silane. Journal of Aerosol Science 34:691–711. https://doi.org/10.1016/S0021-8502(03)00029-6

54. Agarwal P, Girshick SL (2014) Numerical Modeling of an RF Argon–Silane Plasma with Dust Particle Nucleation and Growth. Plasma Chem Plasma Process 34:489–503. https://doi.org/10.1007/s11090-013-9511-3

55. Husmann E, Polito J, Lanham S, et al (2023) Design Considerations for Controlling Silicon Nanoparticle Nucleation and Growth in a Nonthermal Plasma. Plasma Chem Plasma Process 43:225–245. https://doi.org/10.1007/s11090-022-10299-3

56. Xiong Z, Lanham S, Husmann E, et al (2022) Particle trapping, size-filtering, and focusing in the nonthermal plasma synthesis of sub-10 nanometer particles. J Phys D: Appl Phys 55:235202. https://doi.org/10.1088/1361-6463/ac57de

57. Husmann E, Thimsen E, Chen X (2021) Particle charge distributions in the effluent of a flow-through atmospheric pressure low temperature plasma. Plasma Sources Science and Technology 30:075030

58. Kang Z, Tsang CHA, Wong N-B, et al (2007) Silicon Quantum Dots: A General Photocatalyst for Reduction, Decomposition, and Selective Oxidation Reactions. J Am Chem Soc 129:12090–12091. https://doi.org/10.1021/ja075184x

59. Lv P, Xu C, Peng B (2020) Design of a Silicon Photocatalyst for High-Efficiency Photocatalytic Water Splitting. ACS Omega 5:6358–6365. https://doi.org/10.1021/acsomega.9b03755

60. Ni Z, Zhou S, Zhao S, et al (2019) Silicon nanocrystals: unfading silicon materials for optoelectronics. Materials Science and Engineering: R: Reports 138:85–117. https://doi.org/10.1016/j.mser.2019.06.001

61. Yang Y, Yuan W, Kang W, et al (2020) Silicon-nanoparticle-based composites for advanced lithium-ion battery anodes. Nanoscale 12:7461–7484. https://doi.org/10.1039/C9NR10652A

62. O'Farrell N, Houlton A, Horrocks BR (2006) Silicon nanoparticles: applications in cell biology and medicine. Int J Nanomedicine 1:451–472. https://doi.org/10.2147/nano.2006.1.4.451

63. Ksenofontova OI, Vasin AV, Egorov VV, et al (2014) Porous silicon and its applications in biology and medicine. Tech Phys 59:66–77. https://doi.org/10.1134/S1063784214010083

64. Cooper DW (1986) Particulate Contamination and Microelectronics Manufacturing: An Introduction. Aerosol Science and Technology 5:287–299. https://doi.org/10.1080/02786828608959094

65. Selwyn GS (1991) Plasma particulate contamination control. I. Transport and process effects. Journal of Vacuum Science & Technology B: Microelectronics and Nanometer Structures Processing, Measurement, and Phenomena 9:3487–3492. https://doi.org/10.1116/1.585829

66. Jellum GM, Daugherty JE, Graves DB (1991) Particle thermophoresis in low pressure glow discharges. Journal of Applied Physics 69:6923–6934. https://doi.org/10.1063/1.347630

67. Kashihara N, Setyawan H, Shimada M, et al (2006) Suppression of particle generation in a plasma process using a sine-wave modulated rf plasma. J Nanopart Res 8:395. https://doi.org/10.1007/s11051-005-9005-1

68. Watanabe Y, Shiratani M, Makino H (1990) Powder-free plasma chemical vapor deposition of hydrogenated amorphous silicon with high rf power density using modulated rf discharge. Appl Phys Lett 57:1616–1618. https://doi.org/10.1063/1.104087

69. Shiratani MSM, Maeda SMS, Koga KKK, Watanabe YWY (2000) Effects of Gas Temperature Gradient, Pulse Discharge Modulation, and Hydrogen Dilution on Particle Growth in Silane RF Discharges. Jpn J Appl Phys 39:287. https://doi.org/10.1143/JJAP.39.287

70. Kroll U, Meier J, Shah A, et al (1996) Hydrogen in amorphous and microcrystalline silicon films prepared by hydrogen dilution. Journal of Applied Physics 80:4971–4975. https://doi.org/10.1063/1.363541

71. Matsuda A (1983) Formation kinetics and control of microcrystallite in μc-Si:H from glow discharge plasma. Journal of Non-Crystalline Solids 59–60:767–774. https://doi.org/10.1016/0022-3093(83)90284-3

72. Kim Y, Koga K, Shiratani M (2020) Effect of hydrogen dilution on the silicon cluster volume fraction of a hydrogenated amorphous silicon film prepared using plasma-enhanced chemical vapor deposition. Current Applied Physics 20:191–195. https://doi.org/10.1016/j.cap.2019.11.001

73. Amor SB, Dimassi W, Tebai MA, Ezzaouia H (2012) Effect of the hydrogen flow rate on the structural and optical properties of hydrogenated amorphous silicon thin films prepared by plasma enhanced chemical vapor deposition. physica status solidi c 9:2180–2183. https://doi.org/10.1002/pssc.201200238

74. Wang SC, Flagan RC (1990) Scanning Electrical Mobility Spectrometer. Aerosol Science and Technology 13:230–240. https://doi.org/10.1080/02786829008959441

75. Keskinen J, Pietarinen K, Lehtimäki M (1992) Electrical low pressure impactor. Journal of Aerosol Science 23:353–360. https://doi.org/10.1016/0021-8502(92)90004-F

76. Marple VA, Rubow KL, Behm SM (1991) A Microorifice Uniform Deposit Impactor (MOUDI): Description, Calibration, and Use. Aerosol Science and Technology 14:434–446. https://doi.org/10.1080/02786829108959504

77. Friedlander S (2000) Smoke, Dust, and Haze. Oxford University Press

78. Hinds WC (1999) Aerosol Technology: Properties, Behavior, and Measurement of Airborne Particles. John Wiley & Sons

79. Nash DG, Baer T, Johnston MV (2006) Aerosol mass spectrometry: An introductory review. International Journal of Mass Spectrometry 258:2–12. https://doi.org/10.1016/j.ijms.2006.09.017

80. Hevroni A, Golan H, Fialkov A, et al (2011) In situ measurement of the mass concentration of flame-synthesized nanoparticles using quartz-crystal microbalance. Meas Sci Technol 22:115102. https://doi.org/10.1088/0957-0233/22/11/115102

81. Fomin A, Poliak M, Rahinov I, et al (2013) Combined particle mass spectrometer – Quartz crystal microbalance apparatus for in situ nanoparticle monitoring during flame assisted synthesis. Combustion and Flame 160:2131–2140. https://doi.org/10.1016/j.combustflame.2013.04.011

82. Maemura Y, Fujiyama H, Takagi T, et al (1999) Particle formation and a-Si:H film deposition in narrow-gap RF plasma CVD. Thin Solid Films 345:80–84. https://doi.org/10.1016/S0040-6090(99)00100-5

83. Bhandarkar U, Kortshagen U, Girshick SL (2003) Numerical study of the effect of gas temperature on the time for onset of particle nucleation in argon–silane low-pressure plasmas. J Phys D: Appl Phys 36:1399–1408. https://doi.org/10.1088/0022-3727/36/12/307

84. Uner NB, Thimsen E (2018) Low temperature plasma as a means to transform nanoparticle atomic structure. Plasma Sources Sci Technol 27:074005. https://doi.org/10.1088/1361-6595/aad36e

85. Lin Q, Lin X, Yu Y, et al (1993) Measurements in silane radio frequency glow discharges using a tuned and heated Langmuir probe. Journal of Applied Physics 74:4899–4902. https://doi.org/10.1063/1.354322

86. Lenox Laser Orifice Calculator

87. Ihalainen M, Lind T, Arffman A, et al (2014) Break-Up and Bounce of TiO2 Agglomerates by Impaction. Aerosol Science and Technology 48:31–41. https://doi.org/10.1080/02786826.2013.852155

88. Ellenbecker MJ, Leith D, Price JM (1980) Impaction and particle bounce at high Stokes numbers. Journal of the Air Pollution Control Association 30:1224–1227. https://doi.org/10.1080/00022470.1980.10465173

89. Sauerbrey G (1959) Verwendung von Schwingquarzen zur Wägung dünner Schichten und zur Mikrowägung. Z Physik 155:206–222. https://doi.org/10.1007/BF01337937

90. Cumpson PJ, Seah MP (1990) The quartz crystal microbalance; radial/polar dependence of mass sensitivity both on and off the electrodes. Meas Sci Technol 1:544–555. https://doi.org/10.1088/0957-0233/1/7/002

91. Josse F, Lee Y, Martin SJ, Cernosek RW (1998) Analysis of the Radial Dependence of Mass Sensitivity for Modified-Electrode Quartz Crystal Resonators. Anal Chem 70:237–247. https://doi.org/10.1021/ac9706032

92. Lietz AM, Kushner MJ (2016) Air plasma treatment of liquid covered tissue: long timescale chemistry. J Phys D: Appl Phys 49:425204. https://doi.org/10.1088/0022-3727/49/42/425204

93. Goto N, Kudo S, Motoyama H, Ohyama S (2002) Direct Decomposition Technique for NO in O2-N2 Mixture Using Barrier Discharge and Cu Zeolite. Jpn J Appl Phys 41:L64. https://doi.org/10.1143/JJAP.41.L64

94. Olevanov MA, Mankelevich YuA, Rakhimova TV (2004) Coagulation and growth mechanisms for dust particles in a low-temperature plasma. J Exp Theor Phys 98:287–304. https://doi.org/10.1134/1.1675896

95. Vazquez-Pufleau M, Wang Y, Biswas P, Thimsen E (2020) Measurement of sub-2 nm stable clusters during silane pyrolysis in a furnace aerosol reactor. J Chem Phys 152:024304. https://doi.org/10.1063/1.5124996

96. Gatti M, Kortshagen U (2008) Analytical model of particle charging in plasmas over a wide range of collisionality. Phys Rev E 78:046402. https://doi.org/10.1103/PhysRevE.78.046402

97. Agarwal P, Girshick SL (2012) Sectional modeling of nanoparticle size and charge distributions in dusty plasmas. Plasma Sources Sci Technol 21:055023. https://doi.org/10.1088/0963-0252/21/5/055023

98. Lanham SJ, Polito J, Shi X, et al (2021) Scaling of silicon nanoparticle growth in low temperature flowing plasmas. Journal of Applied Physics 130:163302. https://doi.org/10.1063/5.0062255

99. Slootman F, Parent J-C (1994) Homogeneous gas-phase nucleation in silane pyrolysis. Journal of Aerosol Science 25:15–21. https://doi.org/10.1016/0021-8502(94)90178-3

100. Lin Z, Hill RM, Davis HT, Ward MD (1994) Determination of wetting velocities of surfactant superspreaders with the quartz crystal microbalance. Langmuir 10:4060–4068. https://doi.org/10.1021/la00023a026

101. Zhuang H, Lu P, Lim SP, Lee HP (2007) Frequency Response of a Quartz Crystal Microbalance Loaded by Liquid Drops. Langmuir 23:7392–7397. https://doi.org/10.1021/la063767z

102. Le Picard R, Markosyan AH, Porter DH, et al (2016) Synthesis of Silicon Nanoparticles in Nonthermal Capacitively-Coupled Flowing Plasmas: Processes and Transport. Plasma Chem Plasma Process 36:941–972. https://doi.org/10.1007/s11090-016-9721-6

103. Lopez T, Mangolini L (2014) On the nucleation and crystallization of nanoparticles in continuous-flow nonthermal plasma reactors. Journal of Vacuum Science & Technology B 32:061802. https://doi.org/10.1116/1.4899206

104. Piel A (2017) Plasma physics: an introduction to laboratory, space, and fusion plasmas. Springer

105. Melzer A (2019) Physics of Dusty Plasmas. Springer

106. Knipping J, Wiggers H, Rellinghaus B, et al (2004) Synthesis of high purity silicon nanoparticles in a low pressure microwave reactor. Journal of Nanoscience and Nanotechnology 4:1039–1044. https://doi.org/10.1166/jnn.2004.149

107. Mangolini L, Thimsen E, Kortshagen U (2005) High-Yield Plasma Synthesis of Luminescent Silicon Nanocrystals. Nano Letters 5:655–659. https://doi.org/10.1021/nl050066y

108. Chen T, Reich KV V., Kramer NJNJ, et al (2016) Metal–insulator transition in films of doped semiconductor nanocrystals. Nature Materials 15:299–303. https://doi.org/10.1038/nmat4486

109. Meinardi F, Ehrenberg S, Dhamo L, et al (2017) Highly efficient luminescent solar concentrators based on earth-abundant indirect-bandgap silicon quantum dots. Nature Photonics 11:177–185. https://doi.org/10.1038/nphoton.2017.5

110. Xia P, Raulerson EK, Coleman D, et al (2020) Achieving spin-triplet exciton transfer between silicon and molecular acceptors for photon upconversion. Nature Chemistry 12:137–144. https://doi.org/10.1038/s41557-019-0385-8

111. Alvarez Barragan A, Ilawe N V., Zhong L, et al (2017) A Non-Thermal Plasma Route to Plasmonic TiN Nanoparticles. Journal of Physical Chemistry C 121:2316–2322. https://doi.org/10.1021/acs.jpcc.6b08910

112. Exarhos S, Alvarez-Barragan A, Aytan E, et al (2018) Plasmonic Core-Shell Zirconium Nitride-Silicon Oxynitride Nanoparticles. ACS Energy Letters 3:2349–2356. https://doi.org/10.1021/acsenergylett.8b01478

113. Matsoukas T, Russell M, Smith M (1996) Stochastic charge fluctuations in dusty plasmas. Journal of Vacuum Science & Technology A: Vacuum, Surfaces, and Films 14:624–630. https://doi.org/10.1116/1.580156

114. Schweigert VA, Schweigert I V (1996) Coagulation in a low-temperature plasma. Journal of Physics D: Applied Physics 29:655–659. https://doi.org/10.1088/0022-3727/29/3/026

115. Barnes MS, Keller JH, Forster JC, et al (1992) Transport of dust particles in glow-discharge plasmas. Physical Review Letters 68:313–316. https://doi.org/10.1103/PhysRevLett.68.313

116. Staps TJA, van de Ketterij MI, Platier B, Beckers J (2021) The underexposed effect of elastic electron collisions in dusty plasmas. Communications Physics 4:231. https://doi.org/10.1038/s42005-021-00734-w

117. Staps TJA, Maria Donders TJ, Platier B, Beckers J (2022) In-situ measurement of dust charge density in nanodusty plasma. Journal of Physics D: Applied Physics 55:08LT01. https://doi.org/10.1088/1361-6463/ac3581

118. Gopalakrishnan R, Hogan CJ (2012) Coulomb-influenced collisions in aerosols and dusty plasmas. Physical Review E 85:026410. https://doi.org/10.1103/PhysRevE.85.026410

119. Suresh V, Li L, Redmond Go Felipe J, Gopalakrishnan R (2021) Modeling nanoparticle charge distribution in the afterglow of non-thermal plasmas and comparison with measurements. Journal of Physics D: Applied Physics 54:275205. https://doi.org/10.1088/1361-6463/abf70c

120. Ono T, Kortshagen UR, Hogan CJ (2020) Ion attachment rates and collection forces on dust particles in a plasma sheath with finite ion inertia and mobility. Physical Review E 102:063212. https://doi.org/10.1103/PhysRevE.102.063212

121. Ashrafi KS, Yousefi R, Chen M, et al (2020) Dust as probes: Determining confinement and interaction forces. Physical Review E 102:1–10. https://doi.org/10.1103/PhysRevE.102.043210

122. Fortov VE, Khrapak AG, Khrapak SA, et al (2004) Dusty plasmas. Phys-Usp 47:447. https://doi.org/10.1070/PU2004v047n05ABEH001689

123. Fortov VE, Ivlev AV, Khrapak SA, et al (2005) Complex (dusty) plasmas: Current status, open issues, perspectives. Physics Reports 421:1–103. https://doi.org/10.1016/j.physrep.2005.08.007

124. Praburam G, Goree J (1994) Observations of particle layers levitated in a radio-frequency sputtering plasma. Journal of Vacuum Science & Technology A: Vacuum, Surfaces, and Films 12:3137–3145. https://doi.org/10.1116/1.579227

125. Selwyn GS, Heidenreich JE, Haller HL (1990) Particle trapping phenomena in radio frequency plasmas. Appl Phys Lett 57:1876

126. Gorla CR, Liang S, Tompa GS, et al (1997) Silicon and germanium nanoparticle formation in an inductively coupled plasma reactor. J Vac Sci Technol A 15:860

127. Sankaran RM, Holunga D, Flagan RC, Giapis KP (2005) Synthesis of Blue Luminescent Si Nanoparticles Using Atmospheric-Pressure Microdischarges. Nano Letters 5:537–541. https://doi.org/10.1021/nl0480060

128. Le Picard R, Markosyan AH, Porter DH, et al (2016) Synthesis of Silicon Nanoparticles in Nonthermal Capacitively-Coupled Flowing Plasmas: Processes and Transport. Plasma Chemistry and Plasma Processing 36:941–972. https://doi.org/10.1007/s11090-016-9721-6

129. Bapat A, Anderson C, Perrey CR, et al (2004) Plasma synthesis of single-crystal silicon nanoparticles for novel electronic device applications. Plasma Physics and Controlled Fusion 46:B97–B109. https://doi.org/10.1088/0741-3335/46/12B/009|10.1088/0741-3335/46/12B/009

130. Lanham SJ, Polito J, Shi X, et al (2021) Scaling of silicon nanoparticle growth in low temperature flowing plasmas. Journal of Applied Physics 130:163302. https://doi.org/10.1063/5.0062255

131. Bohren CF, Huffman DR (2008) Absorption and scattering of light by small particles. John Wiley & Sons

132. Boufendi L, Hermann J, Bouchoule A, et al (1994) Study of initial dust formation in an Ar-SiH 4 discharge by laser induced particle explosive evaporation. Journal of Applied Physics 76:148–153. https://doi.org/10.1063/1.357120

133. Friedlander SK (2000) Smoke, Dust, and Haze - Fundamentals of Aerosol Dynamcis, 2nd ed. Oxford University Press, New York

134. Sauerbrey G (1959) Verwendung von Schwingquarzen zur Wägung dünner Schichten und zur Mikrowägung. Zeitschrift für Physik 155:206–222. https://doi.org/10.1007/BF01337937

135. Lai FS, Friedlander SK, Pich J, Hidy GM (1972) The self-preserving particle size distribution for Brownian coagulation in the free-molecule regime. Journal of Colloid and Interface Science 39:395–405. https://doi.org/10.1016/0021-9797(72)90034-3

136. Landgrebe JD, Pratsinis SE (1990) A discrete-sectional model for particulate production by gas-phase chemical reaction and aerosol coagulation in the free-molecular regime. Journal of Colloid and Interface Science 139:63–86. https://doi.org/10.1016/0021-9797(90)90445-T

137. Allen JE, Annaratone BM, de Angelis U (2000) On the orbital motion limited theory for a small body at floating potential in a Maxwellian plasma. Journal of Plasma Physics 63:299–309. https://doi.org/10.1017/S0022377800008345

138. Kortshagen U, Bhandarkar U (1999) Modeling of particulate coagulation in low pressure plasmas. Physical Review E 60:887–898. https://doi.org/10.1103/PhysRevE.60.887

139. Agarwal P, Girshick SL (2014) Numerical modeling of an RF argon-silane plasma with dust particle nucleation and growth. Plasma Chemistry and Plasma Processing 34:489–503. https://doi.org/10.1007/s11090-013-9511-3

140. Epstein PS (1924) On the resistance experienced by spheres in their motion through gases. Phys Rev 23:710

141. Verlet L (1967) Computer "Experiments" on Classical Fluids. I. Thermodynamical Properties of Lennard-Jones Molecules. Physical Review 159:98–103. https://doi.org/10.1103/PhysRev.159.98

142. Agarwal P, Girshick SL (2012) Sectional modeling of nanoparticle size and charge distributions in dusty plasmas. Plasma Sources Science and Technology 21:055023. https://doi.org/10.1088/0963-0252/21/5/055023

143. Mamunuru M, Le Picard R, Sakiyama Y, Girshick SL (2017) The Existence of Non-negatively Charged Dust Particles in Nonthermal Plasmas. Plasma Chemistry and Plasma Processing 37:701–715. https://doi.org/10.1007/s11090-017-9798-6

144. Mehringer C, Kloner C, Butz B, et al (2015) Germanium-silicon alloy and core–shell nanocrystals by gas phase synthesis. Nanoscale 7:5186–5196. https://doi.org/10.1039/C4NR06318J

145. Hunter KI, Held JT, Mkhoyan KAA, Kortshagen UR (2017) Nonthermal Plasma Synthesis of Core/Shell Quantum Dots: Strained Ge/Si Nanocrystals. ACS Applied Materials & Interfaces 9:8263–8270. https://doi.org/10.1021/acsami.6b16170

146. Yasar-Inceoglu O, Zhong LL, Mangolini L (2015) Core/shell silicon/polyaniline particles via in-flight plasma-induced polymerization. Journal of Physics D-Applied Physics 48:. https://doi.org/Artn 31400910.1088/0022-3727/48/31/314009

147. Monette Z, Kasar AK, Daroonparvar M, Menezes PL (2020) Supersonic particle deposition as an additive technology: methods, challenges, and applications. Int J Adv Manuf Technol 106:2079–2099. https://doi.org/10.1007/s00170-019-04682-2

148. Firth P, Holman ZC (2018) Aerosol Impaction-Driven Assembly System for the Production of Uniform Nanoparticle Thin Films with Independently Tunable Thickness and Porosity. ACS Appl Nano Mater 1:4351–4357. https://doi.org/10.1021/acsanm.8b01334

149. Minderhout B van, Peijnenburg T, Blom P, et al (2019) The charge of micro-particles in a low pressure spatial plasma afterglow. J Phys D: Appl Phys 52:32LT03. https://doi.org/10.1088/1361-6463/ab2525

150. Chen X, Seto T, Kortshagen UR, Hogan CJ (2019) Determination of nanoparticle collision cross section distribution functions in low pressure plasma synthesis reactors via ion mobility spectrometry. Nano Futures 3:015002. https://doi.org/10.1088/2399-1984/aaff97

151. Chen X, Ghosh S, Buckley DT, et al (2018) Characterization of the state of nanoparticle aggregation in non-equilibrium plasma synthesis systems. J Phys D: Appl Phys 51:335203. https://doi.org/10.1088/1361-6463/aad26f

152. Chen X, Seto T, Kortshagen UR, Hogan CJ (2020) Size and structural characterization of Si nanocrystal aggregates from a low pressure nonthermal plasma reactor. Powder Technology 373:164–173. https://doi.org/10.1016/j.powtec.2020.06.026

153. Sharma G, Abuyazid N, Dhawan S, et al (2020) Characterization of particle charging in low-temperature, atmospheric-pressure, flow-through plasmas. J Phys D: Appl Phys 53:245204. https://doi.org/10.1088/1361-6463/ab7c97

154. Go DB (2012) Theoretical analysis of ion-enhanced thermionic emission for low-temperature, non-equilibrium gas discharges. J Phys D: Appl Phys 46:035202. https://doi.org/10.1088/0022-3727/46/3/035202

155. Stefanović I, Berndt J, Marić D, et al (2006) Secondary electron emission of carbonaceous dust particles. Phys Rev E 74:026406. https://doi.org/10.1103/PhysRevE.74.026406

156. Kim SH, Woo KS, Liu BYH, Zachariah MR (2005) Method of measuring charge distribution of nanosized aerosols. Journal of Colloid and Interface Science 282:46–57. https://doi.org/10.1016/j.jcis.2004.08.066

157. Smith M, Matsoukas T (1998) Constant-number Monte Carlo simulation of population balances. Chemical Engineering Science 53:1777–1786. https://doi.org/10.1016/S0009-2509(98)00045-1

158. Chen X, Hogan CJ (2021) Nanoparticle dynamics in the spatial afterglows of nonthermal plasma synthesis reactors. Chemical Engineering Journal 411:128383. https://doi.org/10.1016/j.cej.2020.128383

159. Johnson EO, Malter L (1950) A Floating Double Probe Method for Measurements in Gas Discharges. Phys Rev 80:58–68. https://doi.org/10.1103/PhysRev.80.58

160. Knutson EO, Whitby KT (1975) Aerosol classification by electric mobility: apparatus, theory, and applications. Journal of Aerosol Science 6:443–451. https://doi.org/10.1016/0021-8502(75)90060-9

161. Cunningham E, Larmor J (1910) On the velocity of steady fall of spherical particles through fluid medium. Proceedings of the Royal Society of London Series A, Containing Papers of a Mathematical and Physical Character 83:357–365. https://doi.org/10.1098/rspa.1910.0024

162. Davies CN (1945) Definitive equations for the fluid resistance of spheres. Proc Phys Soc 57:259–270. https://doi.org/10.1088/0959-5309/57/4/301

163. Sachtler WMH, Dorgelo GJH, Holscher AA (1966) The work function of gold. Surface Science 5:221–229. https://doi.org/10.1016/0039-6028(66)90083-5

164. He C Work function of α-Fe2O3: a DFT calculation

165. Lindmayer J (1966) Field effect studies of the oxidized silicon surface. Solid-State Electronics 9:225–235. https://doi.org/10.1016/0038-1101(66)90107-9

166. Stolzenburg MR, McMurry PH (2008) Equations Governing Single and Tandem DMA Configurations and a New Lognormal Approximation to the Transfer Function. Aerosol Science and Technology 42:421–432. https://doi.org/10.1080/02786820802157823

167. Chahl HS, Gopalakrishnan R (2019) High potential, near free molecular regime Coulombic collisions in aerosols and dusty plasmas. Aerosol Science and Technology 53:933–957. https://doi.org/10.1080/02786826.2019.1614522

168. Gopalakrishnan R, Hogan CJ (2012) Coulomb-influenced collisions in aerosols and dusty plasmas. Phys Rev E 85:026410. https://doi.org/10.1103/PhysRevE.85.026410

169. Gopalakrishnan R, Jr CJH (2011) Determination of the Transition Regime Collision Kernel from Mean First Passage Times. Aerosol Science and Technology 45:1499–1509. https://doi.org/10.1080/02786826.2011.601775

170. Allen JE (1992) Probe theory - the orbital motion approach. Phys Scr 45:497. https://doi.org/10.1088/0031-8949/45/5/013

171. Mott-Smith HM, Langmuir I (1926) The Theory of Collectors in Gaseous Discharges. Phys Rev 28:727–763. https://doi.org/10.1103/PhysRev.28.727

172. Kortshagen UR, Sankaran RM, Pereira RN, et al (2016) Nonthermal Plasma Synthesis of Nanocrystals: Fundamental Principles, Materials, and Applications. Chem Rev 116:11061–11127. https://doi.org/10.1021/acs.chemrev.6b00039

173. Tamadate T, Higashi H, Seto T, Hogan CJ (2020) Calculation of the ion–ion recombination rate coefficient via a hybrid continuum-molecular dynamics approach. J Chem Phys 152:094306. https://doi.org/10.1063/1.5144772

174. Incropera FP, Lavine AS, Bergman TL, DeWitt DP (2007) Fundamentals of heat and mass transfer. Wiley

175. Ion energy distributions, electron temperatures, and electron densities in Ar, Kr, and Xe pulsed discharges: Journal of Vacuum Science & Technology A: Vol 30, No 3. https://avs.scitation.org/doi/full/10.1116/1.4705515. Accessed 21 Jan 2021

176. Global models of pulse-power-modulated high-density, low-pressure discharges - IOPscience. https://iopscience.iop.org/article/10.1088/0963-0252/5/2/006/meta. Accessed 21 Jan 2021

177. Couëdel L, Samarian AA, Mikikian M, Boufendi L (2008) Influence of the ambipolar-to-free diffusion transition on dust particle charge in a complex plasma afterglow. Physics of Plasmas 15:063705. https://doi.org/10.1063/1.2938387

178. Enroth J, Kangasluoma J, Korhonen F, et al (2018) On the time response determination of condensation particle counters. Aerosol Science and Technology 52:778–787. https://doi.org/10.1080/02786826.2018.1460458

179. Liu BYH, Pui DYH (1974) Equilibrium bipolar charge distribution of aerosols. Journal of Colloid and Interface Science 49:305–312. https://doi.org/10.1016/0021-9797(74)90366-X

180. Prokisch C, Bilgic AM, Voges E, et al (1999) Photographic plasma images and electron number density as well as electron temperature mappings of a plasma sustained with a modified argon microwave plasma torch (MPT) measured by spatially resolved Thomson scattering. Spectrochimica Acta Part B: Atomic Spectroscopy 54:1253–1266. https://doi.org/10.1016/S0584-8547(99)00074-9

181. Yan W, Economou DJ (2017) Gas flow rate dependence of the discharge characteristics of a helium atmospheric pressure plasma jet interacting with a substrate. J Phys D: Appl Phys 50:415205. https://doi.org/10.1088/1361-6463/aa8794

182. Aadim KA, Mazhir SN, Abdalameer NK, Ali AH (2020) Influence of Gas Flow Rate on Plasma Parameters Produced by a Plasma Jet and its Spectroscopic Diagnosis Using the OES Technique. IOP Conf Ser: Mater Sci Eng 987:012020. https://doi.org/10.1088/1757-899X/987/1/012020

183. Eslamisaray MA, Wray PR, Lee Y, et al (2023) A Single-Step Bottom-up Approach for Synthesis of Highly Uniform Mie-Resonant Crystalline Semiconductor Particles at Visible Wavelengths. Nano Lett 23:1930–1937. https://doi.org/10.1021/acs.nanolett.2c05084

184. Lanham SJ, Polito J, Xiong Z, et al (2022) Pulsed power to control growth of silicon nanoparticles in low temperature flowing plasmas. Journal of Applied Physics 132:073301. https://doi.org/10.1063/5.0100380

185. Wray PR, Eslamisaray MA, Nelson GM, et al (2022) Broadband, Angle- and Polarization-Invariant Antireflective and Absorbing Films by a Scalable Synthesis of Monodisperse Silicon Nanoparticles. ACS Appl Mater Interfaces 14:23624–23636. https://doi.org/10.1021/acsami.2c03263

186. Tauber C, Schmoll D, Gruenwald J, et al (2020) Characterization of a non-thermal plasma source for use as a mass specrometric calibration tool and non-radioactive aerosol charger. Atmospheric Measurement Techniques 13:5993–6006. https://doi.org/10.5194/amt-13-5993-2020

187. Zhuang Y, Jin Kim Y, Gyu Lee T, Biswas P (2000) Experimental and theoretical studies of ultra-fine particle behavior in electrostatic precipitators. Journal of Electrostatics 48:245–260. https://doi.org/10.1016/S0304-3886(99)00072-8

188. Chaubey N, Goree J, Lanham SJ, Kushner MJ (2021) Positive charging of grains in an afterglow plasma is enhanced by ions drifting in an electric field. Physics of Plasmas 28:103702. https://doi.org/10.1063/5.0069141

189. Kushner MJ (1992) Simulation of the gas-phase processes in remote-plasma-activated chemical-vapor deposition of silicon dielectrics using rare gas–silane-ammonia mixtures. Journal of Applied Physics 71:4173–4189. https://doi.org/10.1063/1.350821

190. Perrin J, Leroy O, Bordage MC (1996) Cross-Sections, Rate Constants and Transport Coefficients in Silane Plasma Chemistry. Contributions to Plasma Physics 36:3–49. https://doi.org/10.1002/ctpp.2150360102

Appendix A: Supplementary Material for Chapter 2

A.1 Details on the Reactor Geometry

Fig. A.1 shows a schematic of the plasma reactor. The tube wall thicknesses for the 1.0 cm, 1.7 cm, 2.2 cm, and 3.2 cm tubes were 0.10 cm, 0.10 cm, 0.15 cm, and 0.30 cm respectively.

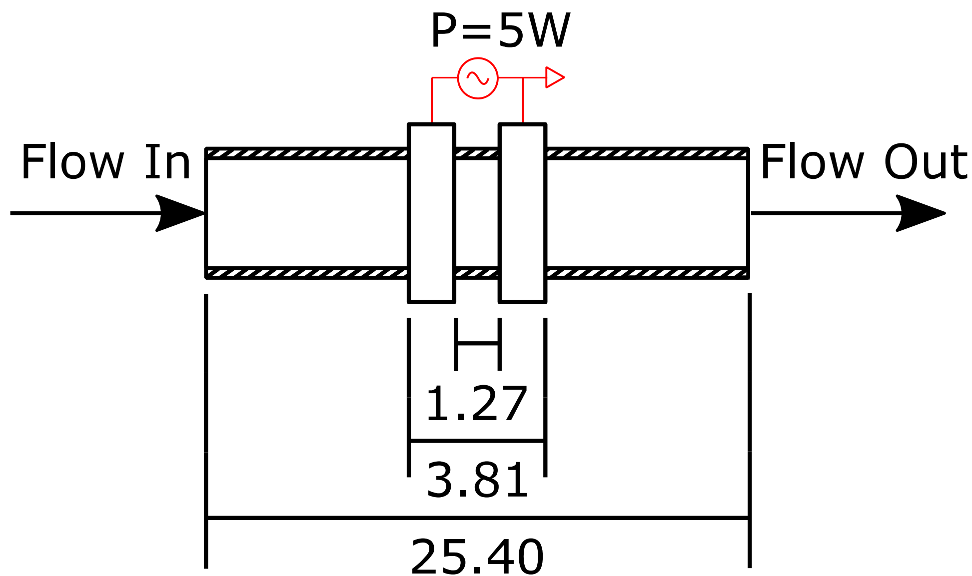

Figure A.1. Illustration of the plasma reactor with the relevant dimensions. Units are given in centimeters.

A.2 Transmission Electron Microscopy (TEM) Images

Particles were synthesized using a reactor tube diameter of 3.2 cm, reactor pressure of 6.5 Torr, and supplied power of 5 W. The feed gas was 51 sccm of argon and 1 sccm of 0.9% silane in helium. Synthesized particles were then impacted onto a lacey carbon TEM grid using the QCM impactor. The TEM grid was lightly adhered to the top of a clean quartz crystal. TEM images were collected using a JEOL JEM-2100F Field Emission scanning transmission electron microscope at an accelerating voltage of 200 kV. Sample images are shown in Fig. A.2. From a sample of 100 particles, the average particle size was about 7 nm, with a geometric standard deviation of 1.21. Synthesized particles appear to be amorphous silicon by inspection.

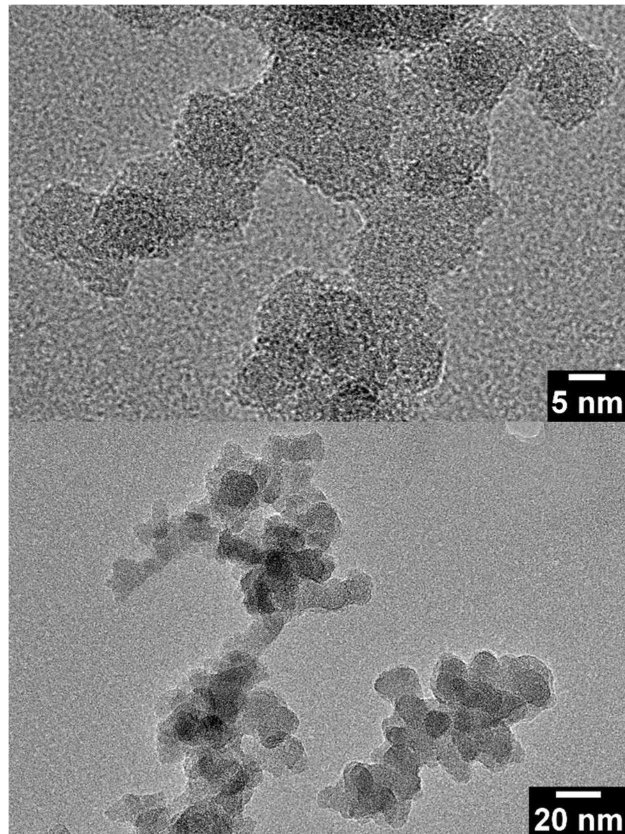

Figure A.2. Sample TEM images of the synthesized particles.

A.3 Fitting the QCM Calibration Data

A derived function for the sensitivity of a planar quartz crystal within the electrode overlap region is provided by Eq. A.3.1 [90]:

$$S = S_{max}\left(J_0(\gamma r)\right)^2 \quad \text{A.3.3}$$

where $J_0(x)$ is the zeroth order Bessel function of the first kind of x, and γ is a constant. Values for S_{max} and γ were determined to be 3.21 Hz·ng^{-1} and 10.6 cm^{-1} respectively via fitting. Fig. A.3 compares the fit of Eq. 10 (from the main text) and Eq. A.3.1 to radially dependent quartz crystal sensitivity. Eq. 10 shows good agreement with the measured data; however, Eq. A.3.1 shows significant divergence from the experimental results at high values of r. This effect is likely due to differences between electrode geometry from our work to the electrode geometry used to derive Eq. A.3.1 [90].

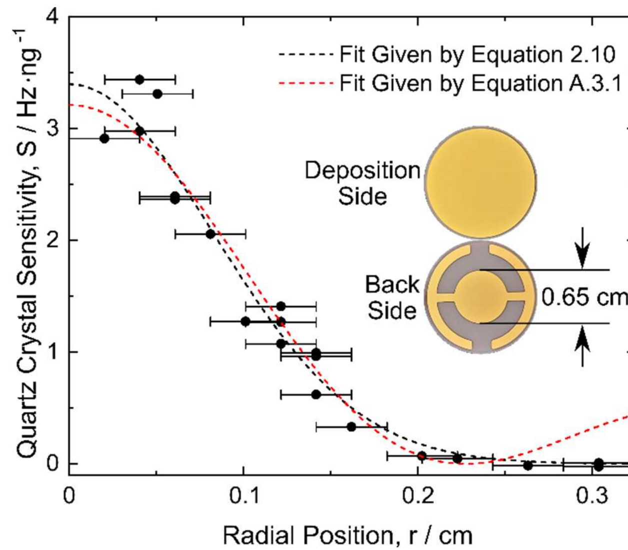

Figure A.3. Quartz crystal sensitivity, S, as a function of radial position, r. Fits from Eq. 2.10 (in main text) and Eq. A.3.1 are provided. The end of the electrode overlap region occurs at r = 0.325 cm.

A.4 Particle Sampling Line Geometry

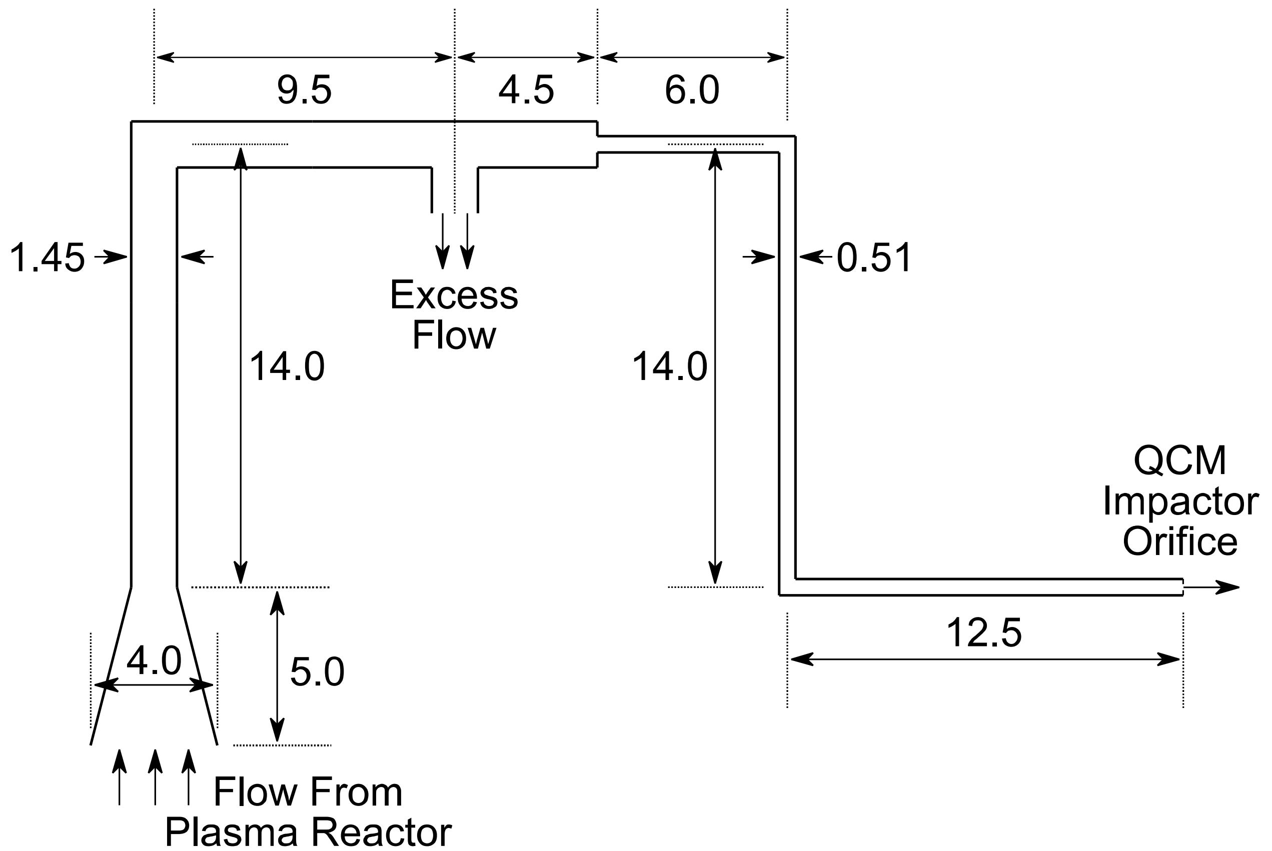

Figure A.4. Geometry of the sampling line running from the plasma reactor to the QCM impactor orifice. The conical reducer (directly downstream of the plasma reactor) was only used for the 2.2 cm and 3.2 cm reactor tubes. Units are given in centimeters.

A.5 Tabulated Parameters and Results

Table A.1 QCM impaction parameters and results

Experiment Number	Reactor Pressure	Tube Diameter	Argon Feed Fraction	Hydrogen Feed Fraction	Silane Feed Fraction	Helium Feed Fraction	Reactor Residence time	Sampling Volumetric Flowrate	Sampling Molar Flowrate	Deposition Rate	Particle Mass Density
-	Torr	cm	%	%	ppm	‰	ms	$cm^3 \cdot s^{-1}$	sccm	$pg \cdot s^{-1}$	$pg \cdot cm^{-3}$
1	4.5	1.7	96.2	0.0	347	38.1	64	2.79	0.99	2.91	1.04
2	4.5	1.7	94.2	0.0	521	57.2	64	2.82	1.00	4.14	1.47
3	4.5	1.7	92.3	0.0	694	76.2	64	2.84	1.01	5.33	1.88
4	4.5	1.7	90.4	0.0	868	95.3	64	2.87	1.02	6.96	2.42
5	4.5	1.7	88.5	0.0	1041	114.3	64	2.90	1.03	9.46	3.26
6	4.5	1.7	86.5	0.0	1215	133.4	64	2.93	1.04	11.62	3.97
7	4.5	1.7	84.6	0.0	1388	152.5	64	2.96	1.05	14.19	4.80
8	6.5	1.7	96.2	0.0	347	38.1	92	2.79	1.43	18.30	6.55
9	6.5	1.7	94.2	0.0	521	57.2	92	2.82	1.45	25.94	9.21
10	6.5	1.7	92.3	0.0	694	76.2	92	2.84	1.46	33.29	11.71
11	6.5	1.7	90.4	0.0	868	95.3	92	2.87	1.47	43.95	15.31
12	6.5	1.7	88.5	0.0	1041	114.3	92	2.90	1.49	55.92	19.30
13	6.5	1.7	86.5	0.0	1215	133.4	92	2.93	1.50	75.52	25.81
14	6.5	1.7	84.6	0.0	1388	152.5	92	2.96	1.52	84.69	28.65
15	8.5	1.7	98.1	0.0	174	19.1	121	2.77	1.86	1.83	0.66
16	8.5	1.7	96.2	0.0	347	38.1	121	2.79	1.87	38.05	13.63
17	8.5	1.7	94.2	0.0	521	57.2	121	2.82	1.89	54.31	19.28
18	8.5	1.7	92.3	0.0	694	76.2	121	2.84	1.91	82.41	28.98
19	8.5	1.7	90.4	0.0	868	95.3	121	2.87	1.93	116.61	40.63
20	8.5	1.7	88.5	0.0	1041	114.3	121	2.90	1.94	183.99	63.49
21	8.5	1.7	86.5	0.0	1215	133.4	121	2.93	1.96	313.90	107.26
22	8.5	1.7	84.6	0.0	1388	152.5	121	2.96	1.98	504.95	170.84
23	4.5	1.7	86.5	9.6	347	38.1	64	2.93	1.04	1.98	0.68
24	4.5	1.7	84.8	9.4	521	57.2	64	2.96	1.05	7.67	2.59
25	4.5	1.7	83.1	9.2	694	76.2	64	2.99	1.06	23.42	7.84
26	4.5	1.7	81.3	9.0	868	95.3	64	3.02	1.07	34.03	11.28
27	4.5	1.7	79.6	8.8	1041	114.3	64	3.04	1.08	37.51	12.32
28	4.5	1.7	77.9	8.7	1215	133.4	64	3.07	1.09	52.24	17.00
29	4.5	1.7	76.2	8.5	1388	152.5	64	3.10	1.10	57.37	18.48
30	6.5	1.7	88.3	9.8	174	19.1	92	2.91	1.49	6.42	2.21
31	6.5	1.7	86.5	9.6	347	38.1	92	2.93	1.51	19.48	6.64
32	6.5	1.7	84.8	9.4	521	57.2	92	2.96	1.52	31.72	10.72
33	6.5	1.7	83.1	9.2	694	76.2	92	2.99	1.53	46.59	15.59
34	6.5	1.7	81.3	9.0	868	95.3	92	3.02	1.55	64.94	21.53
35	6.5	1.7	79.6	8.8	1041	114.3	92	3.04	1.56	85.80	28.18
36	6.5	1.7	77.9	8.7	1215	133.4	92	3.07	1.58	103.80	33.77
37	6.5	1.7	76.2	8.5	1388	152.5	92	3.10	1.59	175.60	56.57
38	8.5	1.7	88.3	9.8	174	19.1	121	2.91	1.95	14.20	4.88
39	8.5	1.7	86.5	9.6	347	38.1	121	2.93	1.97	46.17	15.74
40	8.5	1.7	84.8	9.4	521	57.2	121	2.96	1.99	100.55	33.96
41	8.5	1.7	83.1	9.2	694	76.2	121	2.99	2.00	171.40	57.37
42	8.5	1.7	81.3	9.0	868	95.3	121	3.02	2.02	469.41	155.66
43	8.5	1.7	79.6	8.8	1041	114.3	121	3.04	2.04	897.07	294.68
44	4.5	1.7	0.0	86.5	1215	133.4	64	11.48	4.08	3.85	0.34
45	4.5	1.7	0.0	84.6	1388	152.5	64	11.38	4.04	8.22	0.72
46	6.5	1.7	0.0	88.5	1041	114.3	92	11.57	5.94	2.54	0.22
47	6.5	1.7	0.0	86.5	1215	133.4	92	11.48	5.89	13.02	1.13
48	6.5	1.7	0.0	84.6	1388	152.5	92	11.38	5.84	29.60	2.60
49	8.5	1.7	0.0	88.5	1041	114.3	121	11.57	7.77	7.47	0.65
50	8.5	1.7	0.0	86.5	1215	133.4	121	11.48	7.70	29.96	2.61
51	8.5	1.7	0.0	84.6	1388	152.5	121	11.38	7.64	72.88	6.40

Experiment Number	Reactor Pressure	Tube Diameter	Argon Feed Fraction	Hydrogen Feed Fraction	Silane Feed Fraction	Helium Feed Fraction	Reactor Residence time	Sampling Volumetric Flowrate	Sampling Molar Flowrate	Deposition Rate	Particle Mass Density
-	Torr	cm	%	%	ppm	‰	ms	$cm^3 \cdot s^{-1}$	sccm	$pg \cdot s^{-1}$	$pg \cdot cm^{-3}$
52	6.5	1.0	96.2	0.0	347	38.1	32	2.79	1.43	2.17	0.78
53	6.5	1.0	94.2	0.0	521	57.2	32	2.82	1.45	3.57	1.27
54	6.5	1.0	92.3	0.0	694	76.2	32	2.84	1.46	5.26	1.85
55	6.5	1.0	90.4	0.0	868	95.3	32	2.87	1.47	6.96	2.43
56	6.5	1.0	88.5	0.0	1041	114.3	32	2.90	1.49	8.85	3.05
57	6.5	1.0	86.5	0.0	1215	133.4	32	2.93	1.50	10.59	3.62
58	6.5	1.0	84.6	0.0	1388	152.5	32	2.96	1.52	12.11	4.10
59	6.5	1.7	96.2	0.0	347	38.1	92	2.79	1.43	18.30	6.55
60	6.5	1.7	94.2	0.0	521	57.2	92	2.82	1.45	25.94	9.21
61	6.5	1.7	92.3	0.0	694	76.2	92	2.84	1.46	33.29	11.71
62	6.5	1.7	90.4	0.0	868	95.3	92	2.87	1.47	43.95	15.31
63	6.5	1.7	88.5	0.0	1041	114.3	92	2.90	1.49	55.92	19.30
64	6.5	1.7	86.5	0.0	1215	133.4	92	2.93	1.50	75.52	25.81
65	6.5	1.7	84.6	0.0	1388	152.5	92	2.96	1.52	84.69	28.65
66	6.5	2.2	99.0	0.0	87	9.5	155	2.76	1.41	8.40	3.05
67	6.5	2.2	98.1	0.0	174	19.1	155	2.77	1.42	18.62	6.73
68	6.5	2.2	96.2	0.0	347	38.1	155	2.79	1.43	32.81	11.75
69	6.5	2.2	94.2	0.0	521	57.2	155	2.82	1.45	60.24	21.38
70	6.5	2.2	92.3	0.0	694	76.2	155	2.84	1.46	81.81	28.77
71	6.5	2.2	90.4	0.0	868	95.3	155	2.87	1.47	116.29	40.51
72	6.5	2.2	88.5	0.0	1041	114.3	155	2.90	1.49	138.52	47.80
73	6.5	2.2	86.5	0.0	1215	133.4	155	2.93	1.50	193.91	66.26
74	6.5	2.2	84.6	0.0	1388	152.5	155	2.96	1.52	259.42	87.77
75	6.5	3.2	99.0	0.0	87	9.5	328	2.76	1.41	5.40	1.96
76	6.5	3.2	98.1	0.0	174	19.1	328	2.77	1.42	23.88	8.63
77	6.5	3.2	96.2	0.0	347	38.1	328	2.79	1.43	75.57	27.06
78	6.5	3.2	94.2	0.0	521	57.2	328	2.82	1.45	244.15	86.65
79	6.5	3.2	92.3	0.0	694	76.2	328	2.84	1.46	708.07	249.00
80	6.5	1.0	88.3	9.8	174	19.1	32	2.91	1.49	2.53	0.87
81	6.5	1.0	86.5	9.6	347	38.1	32	2.93	1.51	11.41	3.89
82	6.5	1.0	84.8	9.4	521	57.2	32	2.96	1.52	18.11	6.12
83	6.5	1.0	83.1	9.2	694	76.2	32	2.99	1.53	21.86	7.31
84	6.5	1.0	81.3	9.0	868	95.3	32	3.02	1.55	27.87	9.24
85	6.5	1.0	79.6	8.8	1041	114.3	32	3.04	1.56	31.48	10.34
86	6.5	1.0	77.9	8.7	1215	133.4	32	3.07	1.58	35.09	11.42
87	6.5	1.0	76.2	8.5	1388	152.5	32	3.10	1.59	37.67	12.14
88	6.5	1.7	88.3	9.8	174	19.1	92	2.91	1.49	6.42	2.21
89	6.5	1.7	86.5	9.6	347	38.1	92	2.93	1.51	19.48	6.64
90	6.5	1.7	84.8	9.4	521	57.2	92	2.96	1.52	31.72	10.72
91	6.5	1.7	83.1	9.2	694	76.2	92	2.99	1.53	46.59	15.59
92	6.5	1.7	81.3	9.0	868	95.3	92	3.02	1.55	64.94	21.53
93	6.5	1.7	79.6	8.8	1041	114.3	92	3.04	1.56	85.80	28.18
94	6.5	1.7	77.9	8.7	1215	133.4	92	3.07	1.58	103.80	33.77
95	6.5	1.7	76.2	8.5	1388	152.5	92	3.10	1.59	175.60	56.57
96	6.5	2.2	89.1	9.9	87	9.5	155	2.90	1.49	1.77	0.61
97	6.5	2.2	88.3	9.8	174	19.1	155	2.91	1.49	12.19	4.19
98	6.5	2.2	86.5	9.6	347	38.1	155	2.93	1.51	47.94	16.34
99	6.5	2.2	84.8	9.4	521	57.2	155	2.96	1.52	82.88	27.99
100	6.5	2.2	83.1	9.2	694	76.2	155	2.99	1.53	138.76	46.44
101	6.5	2.2	81.3	9.0	868	95.3	155	3.02	1.55	279.19	92.58
102	6.5	2.2	79.6	8.8	1041	114.3	155	3.04	1.56	430.57	141.44
103	6.5	2.2	77.9	8.7	1215	133.4	155	3.07	1.58	641.27	208.64
104	6.5	2.2	76.2	8.5	1388	152.5	155	3.10	1.59	1011.78	325.97

Experiment Number	Reactor Pressure	Tube Diameter	Argon Feed Fraction	Hydrogen Feed Fraction	Silane Feed Fraction	Helium Feed Fraction	Reactor Residence time	Sampling Volumetric Flowrate	Sampling Molar Flowrate	Deposition Rate	Particle Mass Density
-	Torr	cm	%	%	ppm	‰	ms	$cm^3 \cdot s^{-1}$	sccm	$pg \cdot s^{-1}$	$pg \cdot cm^{-3}$
105	6.5	3.2	89.1	9.9	87	9.5	328	2.90	1.49	3.75	1.29
106	6.5	3.2	88.3	9.8	174	19.1	328	2.91	1.49	30.61	10.52
107	6.5	3.2	86.5	9.6	347	38.1	328	2.93	1.51	125.03	42.61
108	6.5	3.2	84.8	9.4	521	57.2	328	2.96	1.52	249.16	84.16
109	6.5	3.2	83.1	9.2	694	76.2	328	2.99	1.53	561.24	187.85
110	6.5	3.2	81.3	9.0	868	95.3	328	3.02	1.55	996.61	330.49
111	6.5	1.0	0.0	86.5	1215	133.4	32	11.48	5.89	2.10	0.18
112	6.5	1.0	0.0	84.6	1388	152.5	32	11.38	5.84	3.25	0.29
113	6.5	1.7	0.0	88.5	1041	114.3	92	11.57	5.94	2.54	0.22
114	6.5	1.7	0.0	86.5	1215	133.4	92	11.48	5.89	13.02	1.13
115	6.5	1.7	0.0	84.6	1388	152.5	92	11.38	5.84	29.60	2.60
116	6.5	2.2	0.0	84.6	1388	152.5	155	11.38	5.84	2.47	0.22
117	6.5	3.2	0.0	88.5	1041	114.3	328	11.57	5.94	1.60	0.14
118	6.5	3.2	0.0	86.5	1215	133.4	328	11.48	5.89	4.80	0.42
119	6.5	3.2	0.0	84.6	1388	152.5	328	11.38	5.84	11.85	1.04

Table A.2 Mass spectroscopy parameters and results

Experiment Number	Reactor Pressure	Tube Diameter	Argon Feed Fraction	Hydrogen Feed Fraction	Silane Feed Fraction	Helium Feed Fraction	Reactor Residence time	Sampling Volumetric Flowrate	Sampling Molar Flowrate	Silane Conversion
-	Torr	cm	%	%	ppm	‰	ms	$cm^3 \cdot s^{-1}$	sccm	-
120	6.5	1.0	84.6	0.0	1388	152.5	32	2.96	1.52	0.96
121	6.5	1.0	0.00	84.6	1388	152.5	32	11.38	5.84	0.34
122	6.5	3.2	84.62	0.0	1388	152.5	328	2.96	1.52	0.96
123	6.5	3.2	0.00	84.6	1388	152.5	328	11.38	5.84	0.34

A.6 Particle Mass Density as a Function of Silane Concentration

Fig. A.6 shows the same data as Fig. 2.4 in the main text; however, the x-axis was changed from silane fraction to silane concentration. This was performed using the ideal gas law to convert from molar fraction to molar density. Particle mass density is shown to increase with increasing pressure given a constant molar density of silane at the reactor inlet. This can be explained as increasing pressure reduces the diffusion coefficient of reactive species. Given a lower diffusion coefficient, species losses to the reactor walls are expected to be reduced.

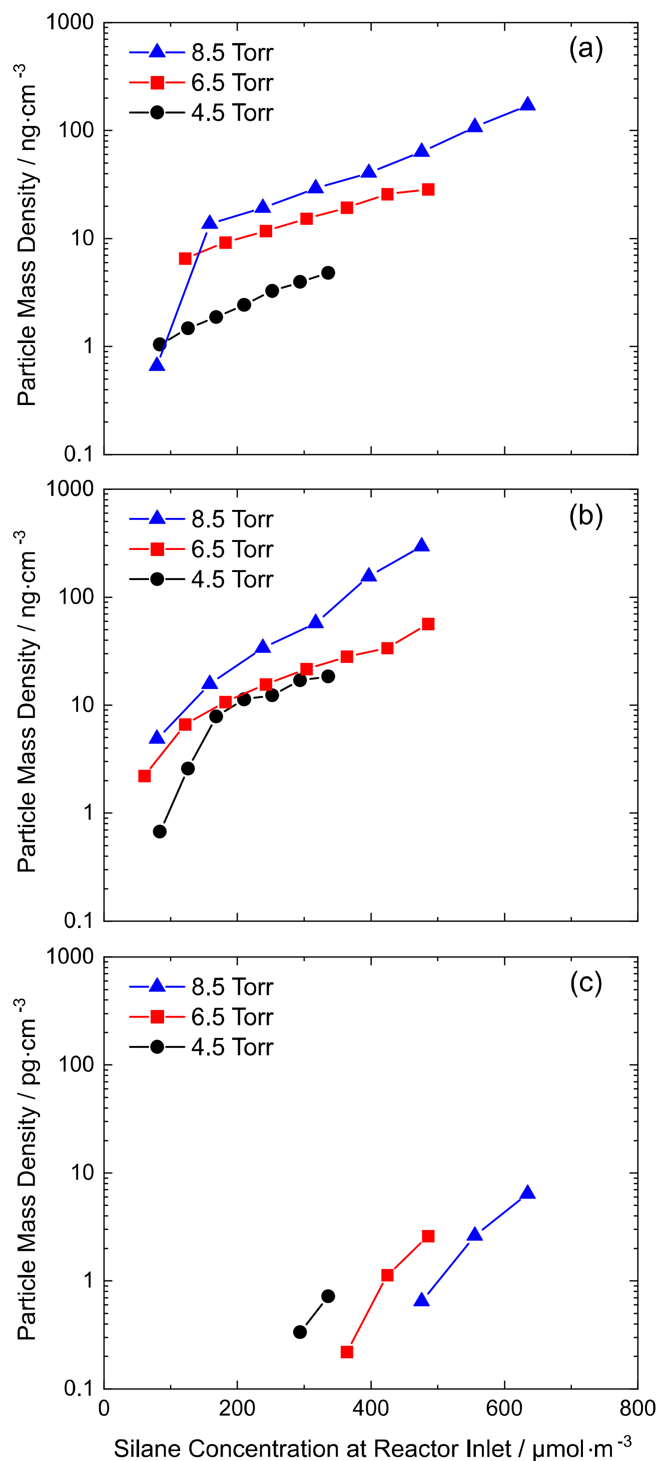

Figure A.6. Mass deposition rate as a function of the silane concentration of the feed gas for various pressures given a balance gas of (a) pure Ar, (b) 10% H_2 in Ar, (c) pure H_2. Tube diameter was held constant at 1.7 cm.

A.7 Reaction Mechanism for Global Model

Table A.3. Gas phase species included in plasma chemistry model

Argon Species

Ar(3*s*), Ar(1s_2), Ar(1s_3), Ar(1s_4), Ar(1s_5), Ar(4*p*), Ar(4*d*), Ar^+

Hydrogen Species[a]

H , H^*, H^+, H^-, H_2 , H_2^+, H_2^* , H_3^+, ArH^+

Silane and Silyl Species[b]

SiH, SiH_2, SiH_3, SiH_4, Si_2H_2, Si_2H_3, Si_2H_4, Si_2H_5, Si_2H_6, Si_nH_{2n+2}, Si_nH_{2n+1}, SiH^-, SiH_2^-, SiH_3^-, $Si_2H_3^-$, $Si_2H_4^-$, $Si_2H_5^-$, SiH_3^+, SiH_2^+

Nanoparticle Species[c]

NP, $NP^\bullet$, NP^+, NP^-

a) * denotes an excited state atom or molecule
b) Si_nH_{2n+2} and Si_nH_{2n+1} species included for $3 \leq n \leq 12$
c) $^\bullet$ denotes a nanoparticle radical. This reactive species is analogous to a Si_nH_{2n+1}.

Table A.4 contains the nanoparticle growth reaction mechanism used in the model. The Ar/SiH_4 gas reaction mechanism is based on previous works [189, 190]. Reaction rates for reactions involving NP have been estimated based on analogous reactions with Si_nH_{2n+2} and Si_nH_{2n+1} and on rates given in Ref. [102].

Table A.4. Nanoparticle growth reaction mechanism

	Reaction	Rate Coefficient[a]
	Nucleation[b]	
1	$Si_{12}H_{26} + SiH \rightarrow NP$	4.0×10^{-11}
2	$Si_{12}H_{26} + SiH_2 \rightarrow NP$	2.0×10^{-11}
3	$Si_{12}H_{26} + SiH_3 \rightarrow NP$	1.0×10^{-11}
4	$Si_{12}H_{26} + SiH_4 \rightarrow NP$	1.0×10^{-30}
5	$Si_{12}H_{26} + Si_2H_2 \rightarrow NP$	6.0×10^{-11}

6	$Si_{12}H_{26} + Si_2H_3 \rightarrow NP$	4.0×10^{-11}
7	$Si_{12}H_{26} + Si_2H_4 \rightarrow NP$	2.0×10^{-11}
8	$Si_{12}H_{26} + Si_2H_5 \rightarrow NP$	1.0×10^{-11}
9	$Si_{12}H_{26} + Si_2H_6 \rightarrow NP$	1.0×10^{-30}
10	$Si_{12}H_{25} + SiH \rightarrow NP$	2.67×10^{-11}
11	$Si_{12}H_{25} + SiH_2 \rightarrow NP$	1.0×10^{-11}
12	$Si_{12}H_{25} + SiH_3 \rightarrow NP$	2.67×10^{-11}
13	$Si_{12}H_{25} + SiH_4 \rightarrow NP$	1.0×10^{-13}
14	$Si_{12}H_{25} + Si_2H_2 \rightarrow NP$	1.0×10^{-11}
15	$Si_{12}H_{25} + Si_2H_3 \rightarrow NP$	2.67×10^{-11}
16	$Si_{12}H_{25} + Si_2H_4 \rightarrow NP$	2.0×10^{-11}
17	$Si_{12}H_{25} + Si_2H_5 \rightarrow NP$	2.67×10^{-11}
18	$Si_{12}H_{25} + Si_2H_6 \rightarrow NP$	1.0×10^{-13}
19	$Si_{11}H_{24} + Si_2H_2 \rightarrow NP$	6.0×10^{-11}
20	$Si_{11}H_{24} + Si_2H_3 \rightarrow NP$	4.0×10^{-11}
21	$Si_{11}H_{24} + Si_2H_4 \rightarrow NP$	2.0×10^{-11}
22	$Si_{11}H_{24} + Si_2H_5 \rightarrow NP$	1.0×10^{-11}
23	$Si_{11}H_{24} + Si_2H_6 \rightarrow NP$	1.0×10^{-30}
24	$Si_{11}H_{23} + Si_2H_2 \rightarrow NP$	6.0×10^{-11}
25	$Si_{11}H_{23} + Si_2H_3 \rightarrow NP$	2.67×10^{-11}
26	$Si_{11}H_{23} + Si_2H_4 \rightarrow NP$	2.0×10^{-11}
27	$Si_{11}H_{23} + Si_2H_5 \rightarrow NP$	2.67×10^{-11}
29	$Si_{11}H_{23} + Si_2H_6 \rightarrow NP$	1.0×10^{-13}
30[c]	$Si_nH_{2n+2} + Si_nH_{2n+1} \rightarrow NP$	1.0×10^{-11}

31[c]	$Si_nH_{2n+2} + Si_nH_{2n+2} \rightarrow NP$	1.0×10^{-30}
32[c]	$Si_nH_{2n+1} + Si_nH_{2n+1} \rightarrow NP$	2.67×10^{-11}
33[d]	$Si_nH_{2n+1} + SiH^- \rightarrow NP^-$	1.0×10^{-9}
34[d]	$Si_nH_{2n+1} + SiH_2^- \rightarrow NP^-$	1.0×10^{-9}
35[d]	$Si_nH_{2n+1} + SiH_3^- \rightarrow NP^-$	1.0×10^{-9}
36[d]	$Si_nH_{2n+1} + Si_2H_3^- \rightarrow NP^-$	1.0×10^{-9}
37[d]	$Si_nH_{2n+1} + Si_2H_4^- \rightarrow NP^-$	1.0×10^{-9}
38[d]	$Si_nH_{2n+1} + Si_2H_5^- \rightarrow NP^-$	1.0×10^{-9}
39[d]	$Si_nH_{2n+2} + SiH^- \rightarrow NP^-$	1.0×10^{-9}
40[d]	$Si_nH_{2n+2} + SiH_2^- \rightarrow NP^-$	1.0×10^{-9}
41[d]	$Si_nH_{2n+2} + SiH_3^- \rightarrow NP^-$	1.0×10^{-9}
42[d]	$Si_nH_{2n+2} + Si_2H_3^- \rightarrow NP^-$	1.0×10^{-9}
43[d]	$Si_nH_{2n+2} + Si_2H_4^- \rightarrow NP^-$	1.0×10^{-9}
44[d]	$Si_nH_{2n+2} + Si_2H_5^- \rightarrow NP^-$	1.0×10^{-9}
45	$Si_{12}H_{25} + SiH_2^+ \rightarrow NP^+$	1.0×10^{-10}
46	$Si_{12}H_{25} + SiH_3^+ \rightarrow NP^+$	1.0×10^{-10}
47	$Si_{12}H_{26} + SiH_2^+ \rightarrow NP^+$	1.0×10^{-10}
48	$Si_{12}H_{26} + SiH_3^+ \rightarrow NP^+$	1.0×10^{-10}
	Charged Particle Reactions	
49	$e + NP \rightarrow NP^-$	1.0×10^{-8}
50	$H^- + NP \rightarrow NP^- + H$	3.0×10^{-10}
51	$Ar^+ + NP \rightarrow NP^+ + Ar$	3.0×10^{-10}
52	$ArH^+ + NP \rightarrow NP^+ + Ar + H$	3.0×10^{-10}

53	$H_2^+ + NP \rightarrow NP^+ + H_2$	3.0×10^{-10}
54	$H_3^+ + NP \rightarrow NP^+ + H_3$	3.0×10^{-10}
55	$H^+ + NP \rightarrow NP^+ + H$	3.0×10^{-10}
56	$Ar^+ + NP^- \rightarrow NP + Ar$	1.0×10^{-8}
57	$ArH^+ + NP^- \rightarrow NP + Ar + H$	1.0×10^{-8}
58	$H_2^+ + NP^- \rightarrow NP + H_2$	1.0×10^{-8}
59	$H_3^+ + NP^- \rightarrow NP + H_3$	1.0×10^{-8}
60	$H^+ + NP^- \rightarrow NP + H$	1.0×10^{-8}
61	$e + NP^+ \rightarrow NP$	1.0×10^{-7}
62	$H^- + NP^+ \rightarrow NP + H$	1.0×10^{-8}
	Growth by Surface Deposition[e]	
63	$SiH^- + NP \rightarrow NP^-$	3.0×10^{-10}
64	$SiH_2^- + NP \rightarrow NP^-$	3.0×10^{-10}
65	$SiH_2^- + NP \rightarrow NP^-$	3.0×10^{-10}
66	$Si_2H_3^- + NP \rightarrow NP^-$	3.0×10^{-10}
67	$Si_2H_4^- + NP \rightarrow NP^-$	3.0×10^{-10}
68	$Si_2H_5^- + NP \rightarrow NP^-$	3.0×10^{-10}
69	$SiH_2^+ + NP \rightarrow NP^+$	3.0×10^{-10}
70	$SiH3^+ + NP \rightarrow NP^+$	3.0×10^{-10}
71	$SiH_2^+ + NP^- \rightarrow NP$	2.89×10^{-8}
72	$SiH3^+ + NP^- \rightarrow NP$	2.89×10^{-8}
73	$SiH^- + NP^+ \rightarrow NP$	1.0×10^{-8}
74	$SiH_2^- + NP^+ \rightarrow NP$	1.0×10^{-8}

75	$SiH_2^- + NP^+ \rightarrow NP$	1.0×10^{-8}
76	$Si_2H_3^- + NP^+ \rightarrow NP$	1.0×10^{-8}
77	$Si_2H_4^- + NP^+ \rightarrow NP$	1.0×10^{-8}
78	$Si_2H_5^- + NP^+ \rightarrow NP$	1.0×10^{-8}
79	$SiH + NP \rightarrow NP$	1.89×10^{-9}
80	$SiH_2 + NP \rightarrow NP$	1.32×10^{-9}
81	$SiH_3 + NP \rightarrow NP$	2.5×10^{-8}
82	$SiH_4 + NP \rightarrow NP$	1.0×10^{-30}
83	$Si_2H_2 + NP \rightarrow NP$	1.32×10^{-9}
84	$Si_2H_3 + NP \rightarrow NP$	6.0×10^{-10}
85	$Si_2H_4 + NP \rightarrow NP$	4.0×10^{-10}
86	$Si_2H_5 + NP \rightarrow NP$	4.0×10^{-10}
87	$Si_2H_6 + NP \rightarrow NP$	1.0×10^{-30}
88[f]	$Si_nH_{2n+1} + NP \rightarrow NP$	4.0×10^{-10}
89[f]	$Si_nH_{2n+2} + NP \rightarrow NP$	1.0×10^{-30}
90	$SiH + NP^- \rightarrow NP^-$	3.78×10^{-9}
91	$SiH_2 + NP^- \rightarrow NP^-$	2.64×10^{-9}
92	$SiH_3 + NP^- \rightarrow NP^-$	5.0×10^{-10}
93	$SiH_4 + NP^- \rightarrow NP^-$	1.0×10^{-30}
94	$Si_2H_2 + NP^- \rightarrow NP^-$	2.64×10^{-9}
95	$Si_2H_3 + NP^- \rightarrow NP^-$	1.2×10^{-9}
96	$Si_2H_4 + NP^- \rightarrow NP^-$	8.0×10^{-10}
97	$Si_2H_5 + NP^- \rightarrow NP^-$	8.0×10^{-10}
98	$Si_2H_6 + NP^- \rightarrow NP^-$	1.0×10^{-30}

99[f]	$Si_nH_{2n+1} + NP^- \rightarrow NP^-$	8.0×10^{-10}
100[f]	$Si_nH_{2n+2} + NP^- \rightarrow NP^-$	1.0×10^{-30}
101	$SiH + NP^+ \rightarrow NP^+$	3.78×10^{-9}
102	$SiH_2 + NP^+ \rightarrow NP^+$	2.64×10^{-9}
103	$SiH_3 + NP^+ \rightarrow NP^+$	5.0×10^{-10}
104	$SiH_4 + NP^+ \rightarrow NP^+$	1.0×10^{-30}
105	$Si_2H_2 + NP^+ \rightarrow NP^+$	2.64×10^{-9}
106	$Si_2H_3 + NP^+ \rightarrow NP^+$	1.2×10^{-9}
107	$Si_2H_4 + NP^+ \rightarrow NP^+$	8.0×10^{-10}
108	$Si_2H_5 + NP^+ \rightarrow NP^+$	8.0×10^{-10}
109	$Si_2H_6 + NP^+ \rightarrow NP^+$	1.0×10^{-30}
110[f]	$Si_nH_{2n+1} + NP^+ \rightarrow NP^+$	8.0×10^{-10}
111[f]	$Si_nH_{2n+2} + NP^+ \rightarrow NP^+$	1.0×10^{-30}
	Agglomeration	
112	$NP + NP^+ \rightarrow NP^+$	1.0×10^{-9}
113	$NP + NP^- \rightarrow NP^-$	1.0×10^{-9}
114	$NP^- + NP^+ \rightarrow NP$	5.0×10^{-8}
115	$NP + NP \rightarrow NP$	1.0×10^{-9}
116	$NP^\bullet + NP^+ \rightarrow NP^+$	5.0×10^{-9}
117	$NP^\bullet + NP^- \rightarrow NP^-$	5.0×10^{-9}
118	$NP^\bullet + NP^\bullet \rightarrow NP$	1.0×10^{-8}
119	$NP^\bullet + NP \rightarrow NP$	5.0×10^{-9}

a) Reaction rates have units of $cm^3 \cdot s^{-1}$. A rate coefficient of 1×10^{-30} $cm^3 \cdot s^{-1}$ is intended to indicate

no appreciable reaction.

b) Nucleation reactions resulting in $NP^{\bullet}$ are not shown. Nucleation of $NP^{\bullet}$ occurs by reactions 1-32 at half the given rate.

c) $7 \leq n \leq 12$

d) $11 \leq n \leq 12$

e) Growth reactions of $NP^{\bullet}$ are not shown. Growth of $NP^{\bullet}$ occurs by reactions 79-89 at half the given rate.

f) $3 \leq n \leq 12$

Appendix B: Supplementary Material for Chapter 3

B.1 The Monte Carlo Code for Particle Trapping Simulation

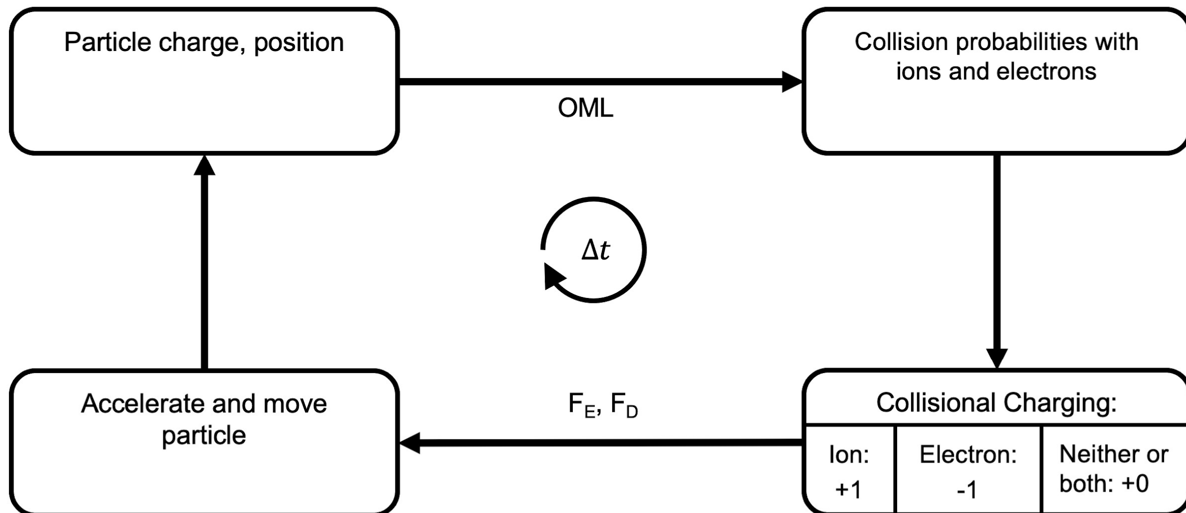

Figure B.1. Schematic of the Monte Carlo code for the parametric simulation of particle trapping. F_E denotes the electrical force, F_D the drag force. OML refers to the orbital motion limited theory of particle charging in plasmas.

B.2: Comsol Simulation Results of a Particle Synthesis

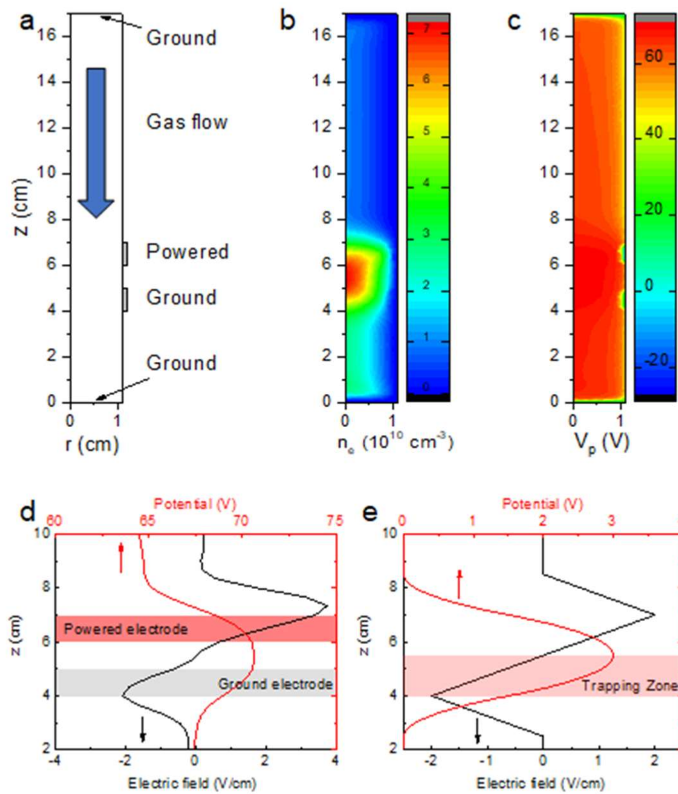

Figure B.2. Comsol simulation results of a particle synthesis reactor to determine the electric field profile to be used in the Monte Carlo simulation. The simulation was performed assuming pure argon with a power of 1 W, a pressure of 1 Torr, and no particles being present. a Schematic of the geometrical set-up of the simulation; b Plasma electron density; c Radio frequency period-averaged electrical potential. d Axial profile of the time-average electrical potential and electric field and e approximate electric field and potential used in the Monte Carlo simulation.

Appendix C: Supplementary Material for Chapter 4

C.1 Design of the Flow-Through Plasma

The capacitively coupled plasma utilized in this study is a dielectric barrier discharge (DBD) plasma reactor, as shown in Fig. C.1. The plasma tube is in a coaxial configuration where the outer electrode is supplied radiofrequency voltage and the inner electrode is grounded. Additionally, the inner electrode is hollow which allows for the insertion of a thermocouple for temperature measurements. Langmuir probe measurements were taken downstream of the outer electrode, but still within the plasma glow region. Dimensions of the system can also be found in Fig. C.1.

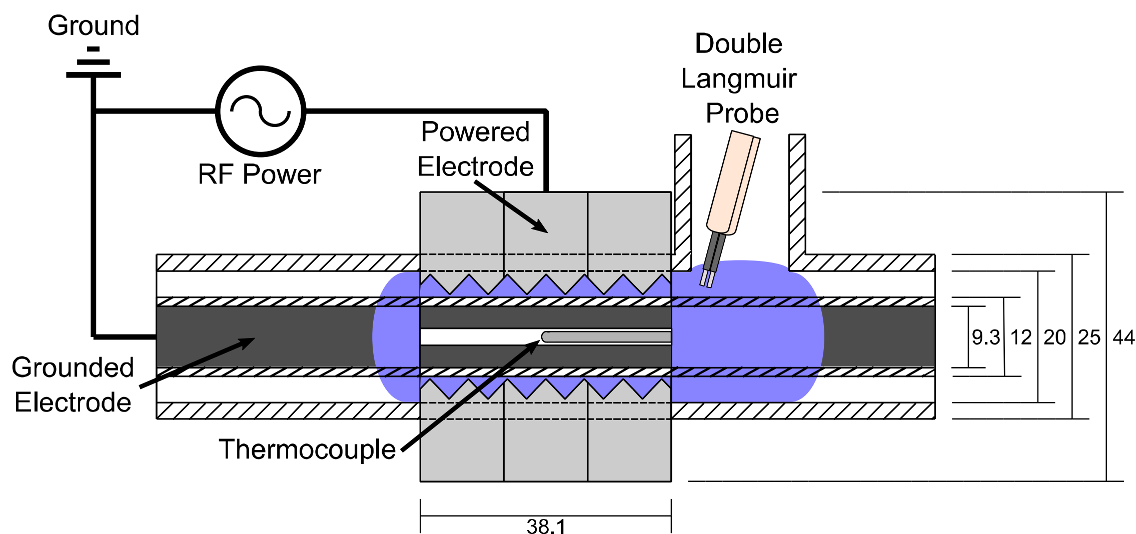

Figure C.1. The flow-through plasma with the Langmuir probe port. Reactor dimensions are given in millimeters.

C.2 DMA Operation and DMA Transfer Function

The DMA was supplied power from a Bertan 225 Series high voltage power supply. By sweeping the DMA voltage, a full mobility spectrum can be measured from the CPC. The DMA voltage sweep for each polarity is described by Eq. C.2.1:

$$V(t) = V_o \left(\frac{V_f}{V_o}\right)^{\frac{t}{\tau}} \quad \text{(C.2.1)}$$

where $V(t)$ is the voltage at time t in kV, V_o is the initial voltage (±0.1 kV), V_f is the final voltage (±10 kV), and τ is the scan time (300s). The voltage is swept in this way in order to simplify the DMA transfer function as described by Wang and Flagan [74].

Traditionally, DMA transfer function accounts for small variances in the streamlines particles must follow to be selected. For instance, the physical width of the inlet and outlet slot of the DMA characterization zone can cause particles of a narrow range of mobilities to be filtered through the DMA. Moreover, the diffusional effect of nanoparticles can also change the DMA transfer function. However, for particles in the size range (~100 nm) of this study, the diffusional effect can be ignored. To confirm this, both a non-diffusing transfer function and a diffusion transfer function were used to invert the CPC data and the same results were obtained. Therefore, for computational ease, the non-diffusive transfer function Ω presented by Stolzenburg and McMurry [166] was utilized in the data inversion procedure:

$$\Omega = \frac{1}{2\beta(1-\delta)}\left(\left|\tilde{Z}_p - (1+\beta)\right| + \left|\tilde{Z}_p - (1-\beta)\right| - \left|\tilde{Z}_p - (1+\beta\delta)\right| - \left|\tilde{Z}_p - (1-\beta\delta)\right|\right) \quad \text{(S2)}$$

where $\tilde{Z}_p = \frac{Z_p}{Z_p^*}$, with Z_p^* being the selected mobility, $\beta = \frac{Q_b+Q_a}{Q_m+Q_s}$, with Q_b being the selected aerosol (outlet) flowrate, Q_a being the aerosol inlet flowrate, Q_m being the excess outlet flowrate, and Q_s being the inlet sheath flowrate, and $\delta = \frac{Q_s-Q_a}{Q_s+Q_a}$.

C.3 The Constant Number Monte Carlo Simulation

The constant number Monte Carlo (CNMC) model utilized in this study is a simplified version of the CNMC model developed by Chen et al [158]. $N = 1000$ monodisperse nanoparticles, initially neutral, are generated in the simulation box. First, inter-event time Δt_k is calculated dynamically at each time step, for the in-plasma simulation:

$$\Delta t_k = \frac{50}{R_T} \tag{C.3.1}$$

$$R_T = C_e \sum_{p=1}^{N} \beta_{e,p} + C_i \sum_{p=1}^{N} \beta_{i,p} \tag{C.3.2}$$

For post plasma simulation Δt_k is additionally determined by the ion and electron loss rates:

$$\Delta t_k = \min\left(\frac{50}{R_T}, \frac{1\%}{R_L}\right) \tag{C.3.3}$$

$$R_L = \max_{a=i,e}\left(\left|\frac{14.64\mathcal{D}_{eff,a}}{D_{tube}^2} + \frac{C_i C_e \beta_{e,i}}{C_a} + \frac{C_p}{N}\sum_{p=1}^{N}\beta_{a,p}\right|\right) \tag{C.3.4}$$

where R_T is the total number of ion-particle and electron-particle collision events per unit time. C_e, C_i and C_p are electron, ion density and particle concentration respectively, and $\beta_{e,p}$, $\beta_{i,p}$ and $\beta_{e,i}$ are collision kernels of electron-particle collision, ion-particle collision and ion-electron collision, respectively. The models used for the collision kernels are described in the next section. R_L is maximum percent change in ion or electron density per unit time, D_{tube} is the diameter of the plasma tube reactor, $\mathcal{D}_{eff,a}$ is the effective diffusion coefficient of ions or electrons. In ambipolar diffusion $\mathcal{D}_{eff,a} = \mathcal{D}_i\left(1 + \frac{T_e}{T_i}\right)$, where $\mathcal{D}_i$ is ion diffusion coefficient, T_i and T_e are ion and electron temperature; in free diffusion $\mathcal{D}_{eff,a}$ equals the diffusion coefficient of ions or electrons, repectively.

In both cases, a maximum of $\alpha = 50$ events are allowed to occur in a time step, which means 5% of nanoparticles can collide with an ion/electron in a time step. Additionally, in post

plasma simulation, if $\frac{50}{R_T} > \Delta t_k$, α is randomly generated from a Poisson distribution with expectation $R_T \Delta t_k$. Smith and Matsoukas [157] demonstrate that the error in constant number Monte Carlo simulation (CNMC) calculation is inversely proportional to the square root of the total number of particles in the simulation box. To test the precision of the current settings, we ran the same simulation stated in this section at $N = 10000$ and same result was obtained with a significant increase in the computation time compared to $N = 1000$ cases. To save computational resources, we elect to use $N = 1000$ and a maximum of 50 events per timestep in our simulation.

After the inter-event time Δt_k and the total number of events α in the timestep are determined, a random number $rand1$ of uniform distribution among (0,1) is then generated. If $rand1 \leq \frac{C_e \sum_{p=1}^{N} \beta_{e,p}}{R_T}$, electron-particle collision will be sampled; if not, ion-particle collision will be simulated. To find the particle experiencing the selected collision event, a new random number $rand2$ from (0,1) is generated and a particle is iteratively randomly selected from the simulation box until $rand2 < \frac{\beta_{a,p}}{\max \beta_{a,p}}$. The charge of the satisfied particle will be altered by +1 for ion-particle collision and -1 for electron-particle collision. This selection process is iteratively simulated until all α events are sampled.

After the particle collision events are sampled, the ion and electron density as well as electron temperature are updated. Ion temperature is always in thermal equilibrium with the carrier gas. In plasma, electron temperature and ion density are constant, while electron density is updated based on quasi-neutral condition:

$$C_e = C_i + \bar{q} C_p \quad \text{(C.3.5)}$$

where is $\bar{q}$ particle average charge in the simulation box. Post plasma, we assume no regeneration term of electrons or ions and their densities decreases due to diffusion loss to the wall (assuming a classical mass transfer model in a laminar, fully developed internal flow [174]), ion-electron recombination, and collisional losses to the particles. The ion or electron density C_a is updated at the end of each timestep:

$$C_a|^{k+1} = C_a|^k - \Delta t_k \left(\frac{14.64\mathcal{D}_{eff,a}}{D_{tube}^2} C_a|^k + \frac{C_i C_e \beta_{e,i}}{C_a} + C_p\Big|^k \frac{\alpha_{a,p}}{N\Delta t_k} \right), \ a = i, e \qquad \text{(C.3.6)}$$

where $\alpha_{a,p}$ is the actual number of ion-particle or electron-particle collision events in the current time step. The electron temperature T_e decays post plasma with a model adapted from temporal afterglow [175, 176]:

$$T_e|^{k+1} = \frac{T_e|^0}{(1+2\mathcal{v}_0 t_{k+1})^2} \qquad \text{(C.3.7)}$$

where $\mathcal{v}_0 = \frac{\sqrt{eT_e|^0/m_i}}{L_{eff}}$, $T_e|^0$ is the initial electron temperature, m_i is the ion mass and L_{eff} is plasma characteristic length.

Then the new residence time $t_{k+1} = t_k + \Delta t_k$ is updated, and a new time step starts. The simulation ends when the residence time t_{k+1} reaches a predefined time.

C.4 Collision Kernel Models

The orbital motion limited model of electron-particle collisions is used to define the electron-particle collision kernel $\beta_{e,p}$ [170]. The collision kernels for ion-particle collision and ion-electron collision follow the work by Hogan and Gopalakrishnan [167–169], who expressed the collision kernel β_{ij} between species i and j in terms of the non-dimensional collision kernel H and diffusive Knudsen number Kn_D:

$$H = \frac{\beta_{ij} m_{ij} \eta_C}{f_{ij} r_{ij}^3 \eta_{FM}^2} \tag{C.4.1}$$

$$Kn_D = \frac{\sqrt{m_{ij} kT}\, \eta_C}{f_{ij} r_{ij} \eta_{FM}} \tag{C.4.2}$$

where m_{ij} and f_{ij} are reduced mass and friction coefficients, r_{ij} is the colliding radius and is the sum of the radius of the two collisional species, k is the Boltzmann constant and T is temperature. η_C and η_{FM} are enhancement factor in Coulombic collision in continuum regime and free molecular regime as defined in the referred literature and is functions of potential energy ratio Ψ_E and non-dimensional screening length S_D

$$\Psi_E = -\frac{q_i q_j e^2}{4\pi\varepsilon_0 r_{ij} kT} \tag{C.4.3}$$

$$S_D = \frac{\lambda_D}{r_p} \tag{C.4.4}$$

where q_i and q_j are integer charges of the two collisional species, e is elementary charge, ε_0 is vacuum permittivity, λ_D is Debye length and r_p is particle radius.

The collision kernel model H is determined by Kn_D and Ψ_E. When $\Psi_E < 0.5$ [168, 169]:

$$H = \frac{4\pi Kn_D^2 + 25.836 Kn_D^3 + \sqrt{8\pi} Kn_D \left(11.211 Kn_D^3\right)}{1 + 3.502 Kn_D + 7.211 Kn_D^2 + 1\ \ .211 Kn_D^3} \tag{C.4.5}$$

Else defined $Kn_\Psi = \frac{3Kn_D}{2\Psi_E}$, when $\min(Kn_\Psi, Kn_D) < 2.5$

$$\frac{H}{4\pi Kn_D^2} = \frac{1}{1 + 1.598(\min[Kn_D, Kn_\Psi])^{1.1709}} \tag{C.4.6}$$

For the atmospheric pressure plasma in the experiment, Eq. C.4.1-C.4.6 are utilized to define the ion-particle collision kernel $\beta_{i,p}$.

For ion-electron collision, screening effect is ignored, so $S_D = \infty$. The Kn_D changes from 243 to 2541 and Ψ_E spans from 784 to 5 when the electron temperature decays from in plasma condition to gas temperature out of plasma as shown in Fig. C.2. Therefore, Eq. C.4.5-C.4.6

alone is not enough to describe $\beta_{e,i}$. Additional high potential collision model for near free molecular regime is applied [167]:

$$H = e^{\mu} \frac{4\pi Kn_D^2 + 25.836 Kn_D^3 + \sqrt{8\pi} Kn_D (11.211 Kn_D^3)}{1 + 3.502 Kn_D + 7.211 Kn_D^2 + 11.211 Kn_D^3} \tag{C.4.7}$$

Where μ is a function of Kn_D and Ψ_E in the referred literature. Eq. C.4.7 is developed for $Kn_D < 2000$ and $\Psi_E < 60$ as illustrated in Fig. C.2. The wide collisionality range of ion-electron collision traditionally makes it difficult to develop a comprehensive collision model [173]. Although combining Eq. C.4.6 and Eq. C.4.7 cannot cover the whole range of ion-electron collisionality, we extend both models and apply Eq. S16 when $\Psi_E < 135$ and Eq. C.4.6 when $\Psi_E \geq 135$ to create a continuum ion-electron collision model.

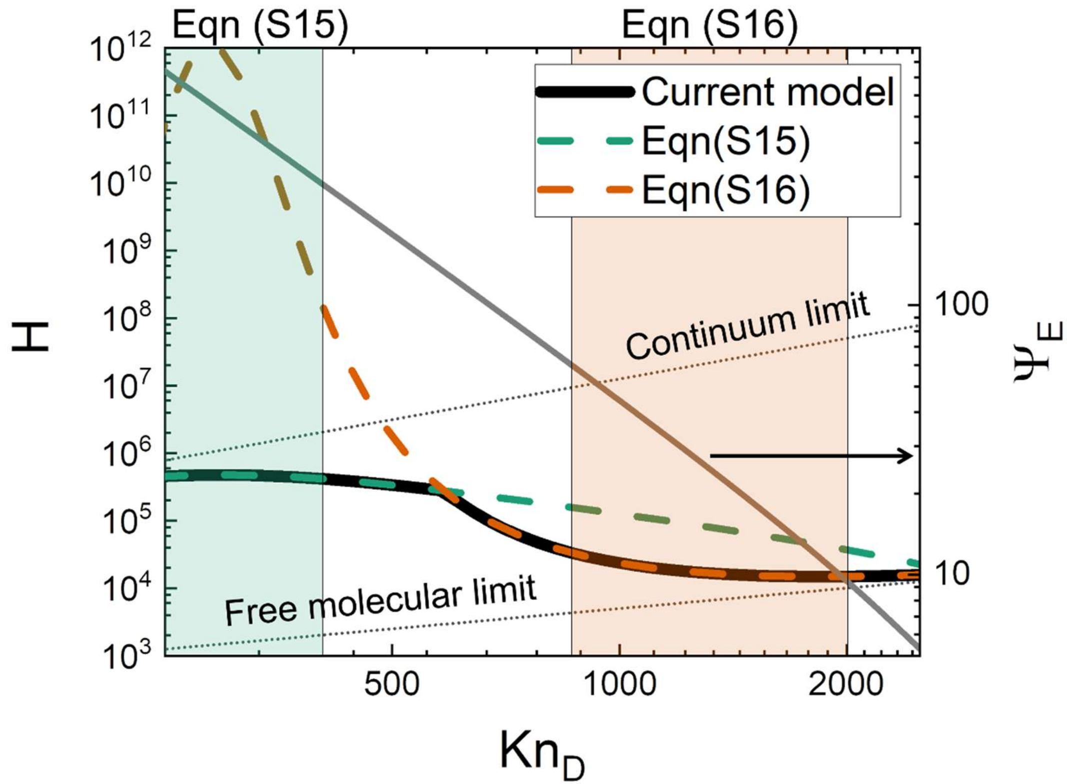

Figure C.2. Ion-electron collision model. Non-dimensional collision kernel H as a function of diffusive Knudsen number Kn_D for Gopalakrishnan & Hogan (2012) model [168] (Eq. S15), Chahl & Gopalakrishnan (2019) [4] (Eq. C.4.7) and the combined model used in this paper in the collisionality range of ion-electron collision. The shaded area is the collisionality range that Eq. C.4.6 and Eq. C.4.7 is originally developed for respectively. Also shown are continuum limit $H = 4\pi Kn_D^2$ and free molecular limit $H = \sqrt{8\pi} Kn_D$ as reference lines and potential energy ratio Ψ_E as a function of Kn_D for ion-electron collision.

C.5 Sample Particle Charge Distribution with the Measured Neutral Fraction

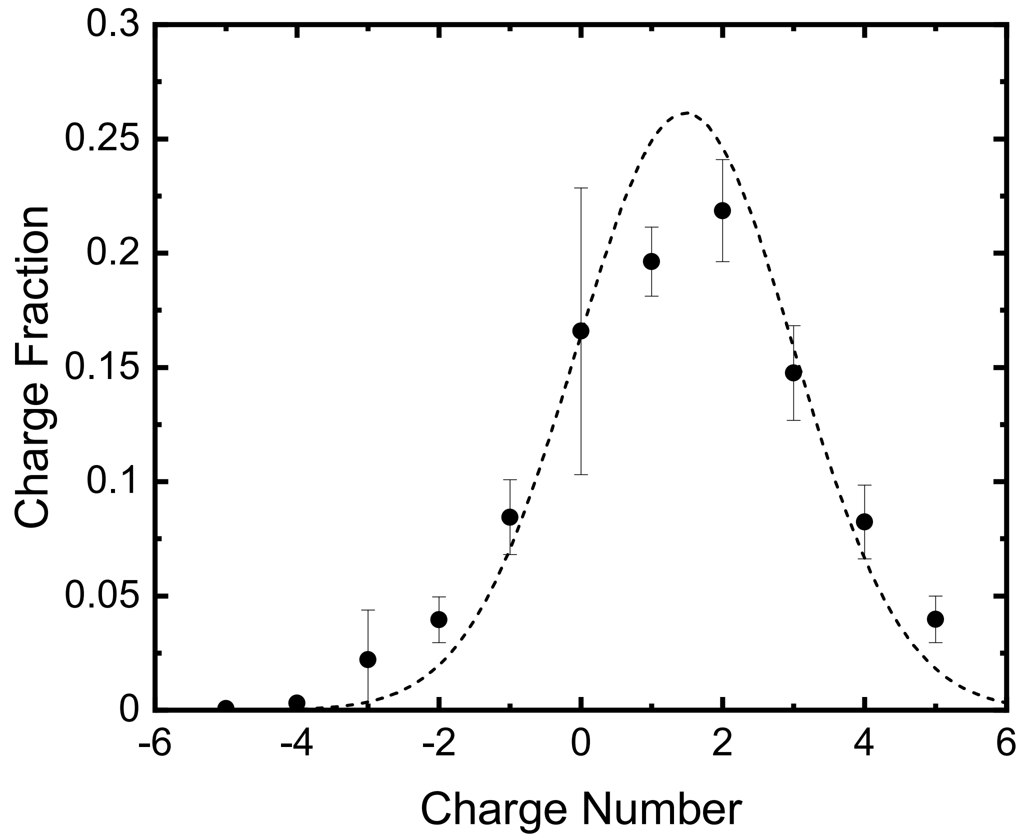

Figure C.3. Charge fraction (markers) post plasma compared to a shifted Boltzmann charge distribution (dotted line). The neutral charge fraction is measured using an electrostatic precipitator, which removes all charged particles, and a CPC. The error bars represent two standard deviations of uncertainty.

C.6 Simulation Results at a Conventional Plasma Condition

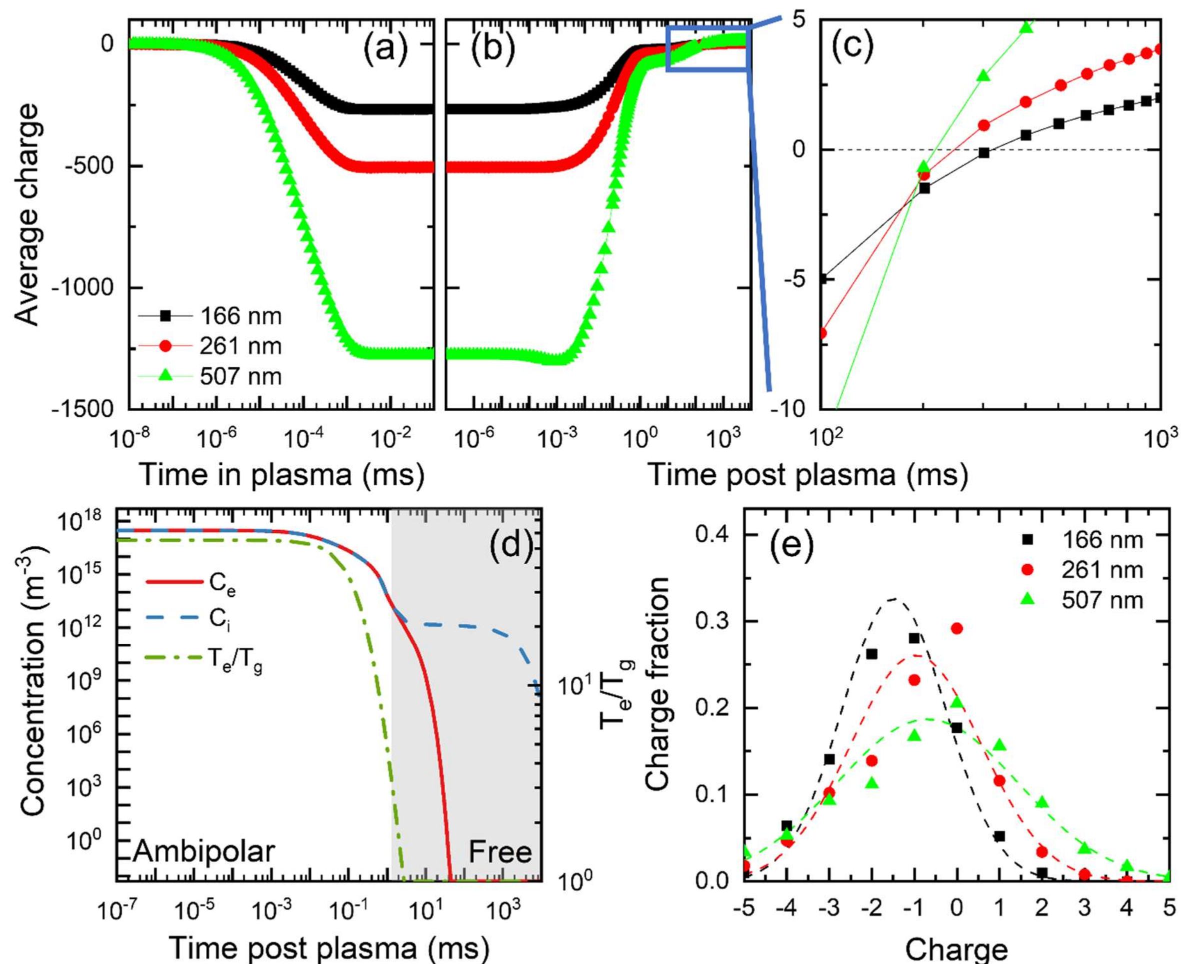

Figure C.4. Simulation results at $T_e = 1.43$ eV and $C_i = 3 \times 10^{11}$ cm^{-3}. (a-c) Average particle charge for various particle diameters as a function of (a) particle residence time in plasma (b-c) particle residence time post plasma. (d) Electron density, ion density and ratio of electron temperature to gas temperature as a function of residence time post plasma for 166 nm SiO_2 nanoparticles. The shaded area is when free diffusion starts. (e) Charge distribution of 166 nm, 261 nm, and 507 nm SiO_2 nanoparticles at a selected residence time of 202 ms (markers) with comparison to charge distributions from Eq. 7 in main text (lines).